Department of Physics and Astronomy
University of Heidelberg

Master thesis
in Physics
submitted by

B.Sc. Lukas Berger
born in Gronau
2023

Characterization of a simple supersonic expansion source for small molecular ions by resonant photodissociation of the nitrous oxide cation

This Master thesis has been carried out by Lukas Berger
at the
Max Planck Institute for Nuclear Physics
under the supervision of

PD Dr. Holger Kreckel

and

Prof. Dr. Xavier Urbain
Université catholique de Louvain

Charakterisierung einer einfachen Überschall-Expansionsquelle für kleine Molekül-Ionen durch resonante Photodissoziation des Distickstoffmonoxid-Kations

Der kryogene Speicherring (CSR) am Max-Planck-Institut für Kernphysik ermöglicht die Speicherung von Molekül-Ionen nahezu beliebiger Masse im extremen Vakuum (Restgasdichten in der Größenordnung von 1000 cm^{-3}) und bei einer niedrigen Temperatur $T < 10$ K (siehe [Hah+16]). In dieser Umgebung kühlen kleine infrarotaktive molekulare Ionen innerhalb von Minuten auf ihre niedrigsten Rotationszustände herunter (siehe [OCo+16]) und astrophysikalisch relevante Reaktionen können unter interstellaren Bedingungen durchgeführt werden. Allerdings fehlt einigen astrophysikalisch relevanten Molekül-Ionen jedoch ein permanentes Dipolmoment (z. B.: H_2^+, H_3^+ und H_3O^+). Sie müssen vor der Injektion in den Speicherring kalt erzeugt werden, da sie nicht in experimentell zugänglichen Zeitskalen herunterkühlen. In dieser Arbeit wird eine einfache Überschallexpansionsquelle auf der Basis eines kommerziellen gepulsten Piezo Ventils und einer Ionisierung durch elektrische Entladung vorgestellt. Sie ermöglicht die Erzeugung intensiver Pulse kleiner molekularer Ionen. Hochauflösende Photodissoziationsspektroskopie von N_2O^+ wird am STARGATE-Experiment genutzt (siehe [Bej+21]) um die interne Anregung der molekularen Ionen zu charakterisieren und ihre Rotationstemperatur zu bestimmen.

Characterization of a simple supersonic expansion source for small molecular ions by resonant photodissociation of the nitrous oxide cation

The Cryogenic Storage Ring (CSR) at the Max Planck Institute for Nuclear Physics allows for the storage of molecular ions of almost arbitrary mass at extreme vacuum (residual gas densities on the order of 1000 cm^{-3}) and at low temperature $T < 10$ K (see [Hah+16]). In this environment, small infrared-active molecular ions will cool to their lowest rotational states within minutes, and studies of astrophysically relevant reactions can be performed under interstellar-like conditions. However, some astrophysically relevant molecular ions lack a permanent dipole moment (e.g.: H_2^+, H_3^+ and H_3O^+) and have to be produced in cold ion sources prior to injection, as they do not cool on experimentally accessible time scales. Here the design of a simple supersonic expansion source based on a commercial pulsed valve and an electric discharge will be presented. It allows for the production of intense pulses of small molecular ions. We use high resolution photodissociation spectroscopy of N_2O^+, employing the STARGATE setup (see [Bej+21]), to characterize the internal excitation of the molecular ions and extract their rotational temperature.

Contents

List of Figures

List of Tables

Acronyms

CSR Cryogenic Storage Ring

CW continuous wave

DR dissociative recombination

FWHM full width at half maximum

IR infrared laser

MCP microchannel plates

MPIK Max Planck Institute for Nuclear Physics

RMS root mean square

Vis visible laser

Constants

Used constants		
symbol	name	value
e	elementary charge	$1.602 * 10^{-19}$ C
ϵ_0	vacuum permittivity	$8.854 * 10^{-12}$ $\mathrm{Fm^{-1}}$
π	pi	3.142
k_B	Boltzmann constant	$1.380 * 10^{-23}$ $\mathrm{JK^{-1}}$
h	Planck constant	$6.626 * 10^{-34}$ $\mathrm{m^2kgs^{-1}}$
$\hbar = \frac{h}{2\pi}$	reduced Planck constant	$1.055 * 10^{-34}$ $\mathrm{m^2Js}$
$\overline{R}$	universal gas constant	8.314 $\mathrm{JK^{-1}mol^{-1}}$

Chapter 1

Motivation

The Cryogenic Storage Ring (CSR) is an electrostatic storage facility with a circumference of 35 m that can be cooled to cryogenic temperatures ($T_{CSR} < 10$ K) by a closed cycle liquid helium unit. The experimental chambers maintain an ultra high vacuum with residual gas densities on the order of 10^3 cm^{-3}. The black body radiation field is strongly reduced compared to room temperature experiments. The ion optical lattice allows for storage of ions with kinetic energies between 30 keV to 300 keV per unit charge. A dedicated neutral beam line is connected to a straight section of the storage ring, allowing the stored ions to be merged with a fast beam of neutral atoms (see [Hah+16] and [Gru+22]). The neutrals are produced by photodetachment of negative ions, resulting in a ground term atomic beam. The relative collision energy can be tuned by changing the kinetic energy of the anion beam in an independent drift tube before they pass the photodetachment laser, enabling energy resolved measurements. The next straight section of the CSR is equipped with an electron cooler. It uses an unconventional design for smaller energy uncertainty, that is necessary because of the small ion velocities in the CSR compared to magnetic storage rings. The electron cooler can also be used for high resolution recombination experiments. In this section of the CSR, various laser can be used for photospectroscopy. A low temperature reaction microscope (REMI) was recently installed in the CSR and will be tested in the near future. The setup of the CSR allows us to study reactions of neutrals, ions, electrons and photons at cryogenic temperatures and low gas densities, comparable to conditions in the cold interstellar medium.

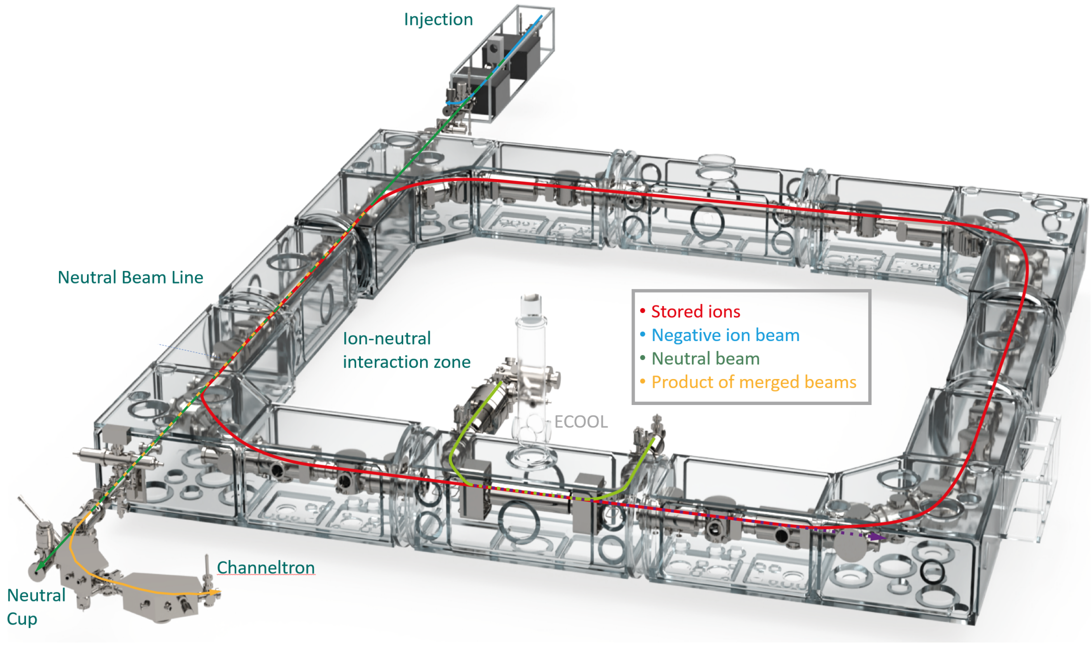

Figure 1.1: The Cryogenic Storage Ring (CSR) at the Max Planck Institute for Nuclear Physics in Heidelberg [Gru23].

It has been shown in previous studies that small infrared active molecular ions like CH^+ and OH^-, when stored inside the CSR, will cool radiatively to their lowest vibrational and rotational states. Vibrations cool relatively fast and for most infrared active ions the lowest vibrational states are reached after the first few seconds [Gru+22]. The lowest rotational states are reached for most infrared active ions after a few minutes (see [OCo+16] and [Mey+17]). There are three possible processes that can change a state of a molecule: absorption of a photon inducing a transition to an excited state, spontaneous emission of a photon and stimulated emission. Einstein coefficients are used to quantify these processes. A_{21} is the Einstein coefficient for spontaneous emission, B_{12} is the Einstein coefficient for absorption and B_{21} is the Einstein coefficient for stimulated emission. They are related by the condition

$$B_{21} = \frac{g_1}{g_2} B_{12} = \frac{c^3}{8\pi\nu_{12}^3 h} A_{21}. \tag{1.1}$$

g_i is the multiplicity of the state i, c is the speed of light, h is the Planck constant and ν is the wavenumber of the transition [Ber16]. For the CSR, the stimulated emission can be neglected and the time dependent evolution of rotational states can be described with the following coupled differential equations.

$$\frac{dP_i(t)}{dt} = -P_i(t)\left(\sum_k A_{ik} + \sum_j B_{ij}\rho(\nu_{ij})\right) + \sum_j A_{ji}P_j + \sum_k B_{ki}\rho(\nu_{ki})P_k(t) \tag{1.2}$$

for $j > i > k$. P_k, P_i or P_j describe the population of the respective states. $\rho(\nu_{ij})$ describes the thermal radiation field for the transition ν and can be estimated with Planck's law

$$\rho = \frac{8\pi h\nu^3}{c^3} * \frac{1}{e^{-h\nu/k_B T} - 1}. \tag{1.3}$$

k_B is the Boltzmann constant.
For diatomic molecules like HD$^+$ the Einstein coefficients for spontaneous emission can be estimated with

$$A_{21} = \frac{2\omega_{21}^3}{3\epsilon_0 hc^3}\mu_{21}^2. \tag{1.4}$$

ω is the angular frequency, μ is the dipole moment and ϵ_0 is the vacuum permittivity. A more detailed description can be found in [Hil82]. The specific transitions can be calculated with the rotational constant

$$\hbar\omega = 2B(J+1). \tag{1.5}$$

$\hbar$ is the reduced Planck constant, J is the rotational quantum number and B is the rotational constant.
The dipole moment for HD$^+$ is $\mu_{\mathrm{HD}^+} = 0.86$ D (see [Sah74] and [Bun74]) and the rotational constant is $B_{\mathrm{HD}^+} = 21.9\ \mathrm{cm}^{-1}$ (see [CLT11]). Assuming an initial Boltzmann distribution of HD$^+$ at $T_0 = 300$ K and a temperature in the CSR of $T_{CSR} = 10$ K, one can calculate the evolution for the population of the states for the storage time in the CSR using equation 1.2. For $J = 0$ to $J = 9$ this can be seen in fig. 1.2.

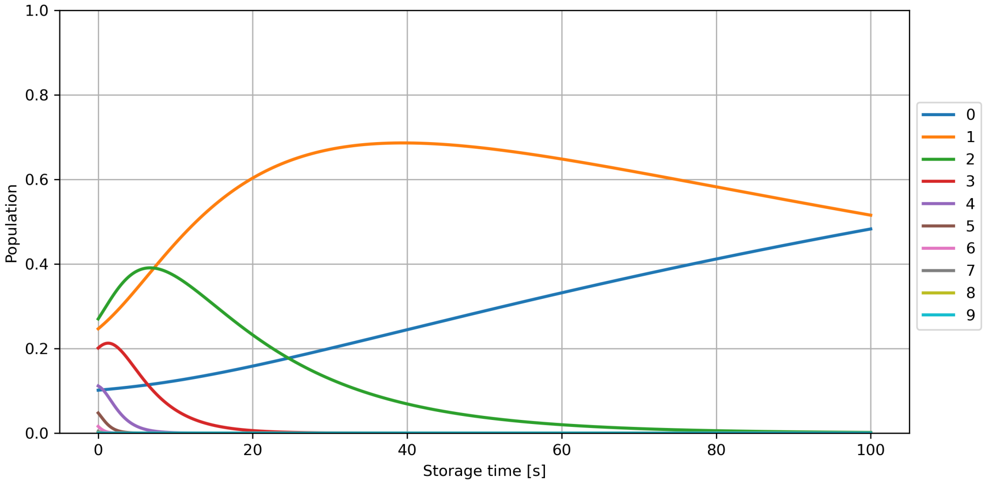

Figure 1.2: Population of rotational states of HD$^+$ after eq. 1.2 for $T_0 = 300$ K and $T_{CSR} = 10$ K.

The cooling is dependent on the dipole moment of the molecule. However, there are molecules with great relevance to astrophysics that lack a dipole moment and do not cool down in accessible timescales (e.g.: H_2^+, H_3^+ and H_3O^+). A focus of interest is on H_3^+ as it has a high reactivity and was first spectroscopically detected in dense molecular clouds by Geballe and Oka in 1996 [GO96]. H_3^+ is important for interstellar chemistry (see fig. 1.3), as it acts as "universal protonator" [McC+04].

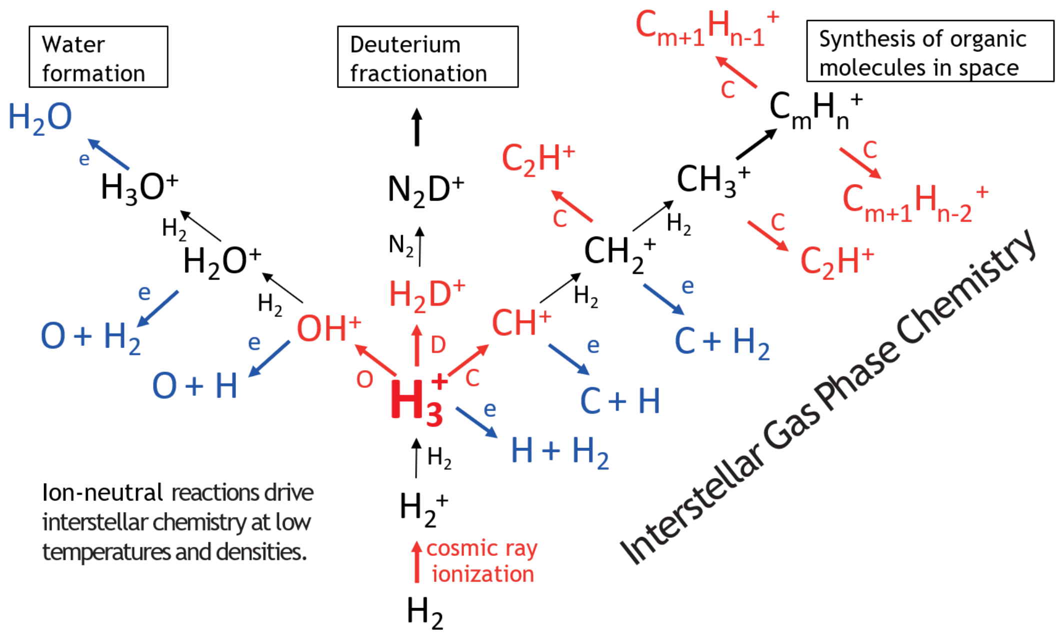

Figure 1.3: The interstellar gas phase chemistry starting with H_3^+ ([Kre23] and cf. [McC01]).

However, the density of H_3^+ in diffuse interstellar clouds ($n \sim 10^{-3}$ to 10^{-5} cm^{-3}) [McC+98] did not match the observed large column densities using infrared absorption spectroscopy in diffuse interstellar clouds [McC+02]. This led to discussions if the adopted laboratory DR rate ($\sim 2 * 10^{-7} \frac{\mathrm{cm}^3}{\mathrm{s}}$) [McC+04] was applicable in interstellar conditions. Overall, laboratory determinations of the DR rate of H_3^+ varied over several orders of magnitude (10^{-6} to $10^{-11} \frac{\mathrm{cm}^3}{\mathrm{s}}$ (see [McC+04])). Stationary afterglow measurements report that the DR rate is pressure dependent [Glo+00]. Other measurements suggest that the DR cross section changes with rotational excitations (see [Wol+04], [Lam+03] and [Lar+03]). To study the DR process of H_3^+ in the interstellar medium the molecule has to be stored at low pressure and be vibrationally and rotationally cold.

While vibrational excitations of H_3^+ cool in a few seconds, rotations cool much slower (see [Kre+04] and [Kre+02]). In fact, H_3^+ does not cool to the lowest rotational states in accessible storage times in cryogenic storage rings. To study those molecules at low temperatures they have to be produced cold before they get injected into the storage ring.

A simple supersonic expansion ion source was built at the Max Planck Institute for Nuclear Physics with the goal to produce cold ions. The idea to use supersonic expansion to produce cold ions is not new (see [McC+04],[Kre+10], [Zha+07] and [PT89]). However, many designs of supersonic expansion ion sources are complicated and often unstable ([PT89] and [McC+04]). When, for a example, a laser is used for photoionisation of the gas (see [Pot+97]) one wants to have a high density ion beam that overlaps perfectly with a high intensity laser beam to ionize as much molecules as possible. For high densities of ions often a pulsed source is used. Pulsed lasers compress the energy into short time domains. This results in high peak power and intensity over the duration of the pulse. For this reason pulsed lasers are often used with pulsed sources. The pulsed source must then be synchronized with the pulsed laser resulting in a complex experimental setup. For example in [Pot+97] a supersonic expansion through a pulsed nozzle of 150 μm is used with a mode-locked Ti:sapphire femtosecond laser (Spectra Physics, Tsunami 3955) pumped by 10 W Ar^+ laser (Spectra Physics, Beam Lock 2060) and a regenerative amplifier pumped by a 10 Hz Nd:YAG laser (Spectra Physics, GCR 150.10) followed by a frequency doubling. Other designs use a pulsed electron gun for electron impact ionization [CRE06] or a pulsed discharge [Kre+10] which require complex power supplies. The pulsed valves must pulse quickly against high pressure differences to produce short pulses with very high gas density in order to not overload the pumps. A source based on a solenoid valve (General Valve, Series 9) could be operated at 50 Hz with a short pulse limit of 300 μs [McC+04]. The design of [PT89] is based on a piezo valve and was operated with pulses as narrow as 50 μs at up to 150 Hz.

A new design was developed at the Max Planck Institute for Nuclear Physics that relies on the commercial available Amsterdam Piezo Valve and a discharge between two electrodes for ionization. One electrode is grounded while a constant high voltage is applied to the other electrode. The discharge can be produced with conventional available power supplies (see section 3.2). The valve has opening times in the order of 20 μs to continuum and was tested up to 5 bar (see section 3.1). A nozzle of 2.5 mm was used. The source produces pulses of up to 5 μA. The manufacturer claims a repetition rate up to 5 kHz (see [Mas]). Due to the large nozzle, our repetition rate was limited by the pumping power and not by the repetition rate of the amsterdam piezo valve.
Thanks to a collaboration with the Université Catholique de Louvain in Belgium the ion source was transported to the lab of Prof. Dr. Xavier Urbain. Here, the supersonic expansion ion source was tested with N_2O and the internal rotational temperature of N_2O^+ ions exiting the source was measured with resonant photodissociation.

Chapter 2

Ideal supersonic expansion

In this thesis, a simple supersonic expansion ion source is used to produce subthermal molecular ions. This chapter aims to give an introduction into the ideal supersonic expansions using the ideal continuum model. First the process of supersonic expansion will be explained. After that some basics and useful relations will be outlined. Then the isentropic flow equations will be derived and the choked flow through a nozzle will be discussed.

2.1 Ideal continuum model

Supersonic expansion is a process where a jet of a compressible fluid flows from a high-pressure regime a) through a nozzle with diameter D in a low-pressure regime b). The fluid is at rest in regime a), flows with sonic velocity through the nozzle and undergoes a lot of collisions. After this the fluid expands into the low-pressure regime and reaches velocities above the speed of sound.

The idea behind the supersonic expansion is that the unordered internal energy of the fluid at rest in regime a) gets translated into kinetic energy by collisions of the particles inside the nozzle. At high pressures in regime a) effects of gas viscosity and heat transfer can be neglected [Mor96]. In an adiabatic isentropic expansion and when the nozzle diameter D is much smaller than the mean free path of the molecules λ_0, the sum of enthalpy H and kinetic energy $E_{kin} = \frac{1}{2}mv(x)^2$ is assumed to be constant [Mor96].

$$H(x) + \frac{1}{2}m(v(x))^2 = constant \tag{2.1}$$

m is the mass, and $v(x)$ is the velocity in direction x.

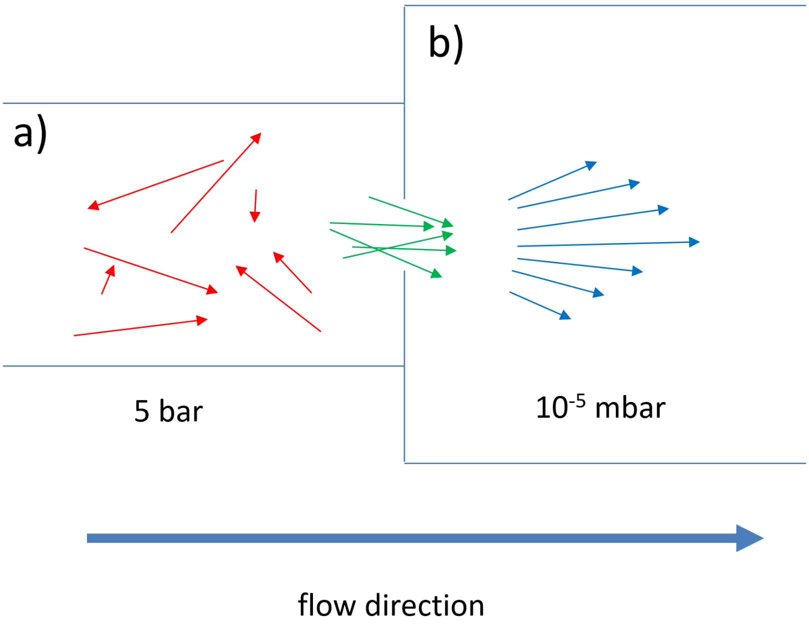

Figure 2.1: Supersonic expansion from high pressure regime a) through a nozzle into a low pressure regime b). Unordered internal energy gets translated into directed energy by collisions inside of the nozzle. (cf. [Bej21])

Random motion is converted into directed mass flow.

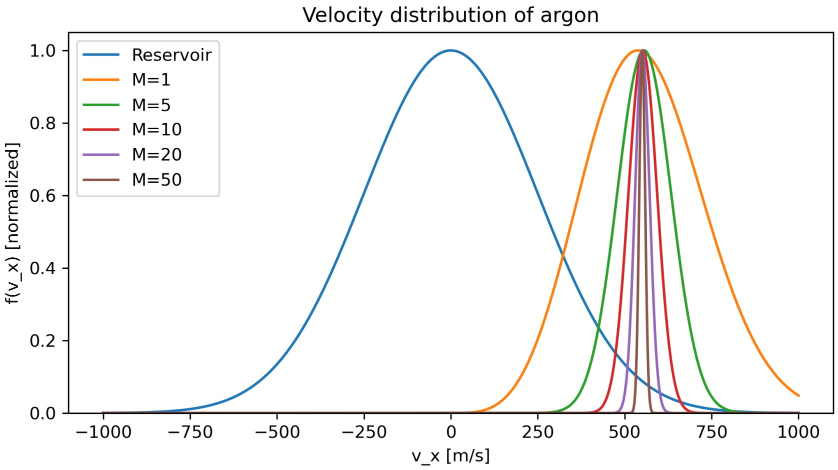

Figure 2.2: Maxwell-Boltzmann velocity distribution of argon compared to the distribution of the jet for different Mach numbers (see eq. 2.5). The full width at half maximum (FWHM) represents the translational temperature. (cf. [Bej21] and [IMV03])

The velocity distribution of the jet for different Mach numbers (see fig.: 2.2) can be described by the equation:

$$
\begin{aligned}
f_v(v_x) = &\left(\frac{m_{mol}}{RT_0}\right)^{3/2} \left(1 + \frac{\gamma - 1}{2} M^2\right)^{3/2} v_x^3 \, * \\
&exp\left(-\left(\left(\frac{m_{mol}}{RT_0}\right)^{1/2} (1 + \frac{\gamma - 1}{2} M^2)^{1/2} v_x - \left(\frac{\gamma}{2}^{1/2}\right) M\right)^2\right)
\end{aligned}
\tag{2.2}
$$

M is the Mach number (see eq. 2.5), m_{mol} is the molar mass of the gas, R is the gas constant (see eq. 2.4), γ is the adiabatic index (see eq. 2.9), T_0 is the inital temperature and v_x is the velocity in x direction.
The translation temperature is the full width at half maximum (FWHM). It shows, that for higher Mach numbers the gas is cooler but has a higher kinetic energy (see [Bej21] and [IMV03]).

2.2 Fluids

A fluid is defined as a substance that deforms continuously when acted upon by a shear stress. By this definition liquids and gases are fluid. A liquid is a nearly incompressible fluid that retains a nearly constant volume independent of pressure, while a gas is compressible. Supersonic expansion is based on the compressibility of the fluid. However, for subsonic flows the compressibility of a gas can be neglected and a steady flow through a narrowing nozzle leads to an increase in gas velocity. When the velocity of the gas is near to the sound velocity of that gas, effects of compressibility become more important (cf. [Gir22] pages 27 to 30 and [PMA19] pages 27 to 30).

2.3 Speed of sound and Mach number

As subsonic, sonic and supersonic have already been mentioned, the speed of sound is introduced next. The speed of sound v_s describes the propagation velocity of pressure waves (small disturbances) in the fluid and is highly dependent on the properties of the medium. In a calorically perfect ideal gas the sound velocity v_s can be calculated by

$$
v_s = \sqrt{\gamma \frac{p}{\rho}} = \sqrt{\gamma R T}. \tag{2.3}
$$

In this equation γ is the adiabatic index, p is the pressure, ρ is the density, T is the absolute temperature and R is the specific gas constant (see [Gir22]). The specific gas constant is given by

$$R = \frac{\overline{R}}{m_{mol}}. \tag{2.4}$$

$\overline{R}$ is the universal gas constant and m_{mol} is the molar mass of the gas.

The Mach number

$$M = \frac{u}{v_s} \tag{2.5}$$

is a dimensionless quantity that represents the speed of an object u relative to the speed of sound in the surrounding medium v_s.

2.4 Mean free path

To reach cold temperatures in a supersonic expansion the molecules of the fluid have to undergo a lot of collisions in the nozzle and translate unordered internal energy into kinetic energy (see fig.: 2.1). The mean free path is the distance a particle can travel before colliding with another particle. It is defined by

$$\lambda_0 = \frac{k_B T_0}{\sqrt{2} p \sigma}. \tag{2.6}$$

T_0 is the temperature, p is the pressure, k_B is the Boltzmann constant and σ is the collisional cross section. For a one component gas one can approximate the effective cross section from spherical particles with radius r.

$$\sigma = 2\pi(2r)^2 \tag{2.7}$$

Using the van der Waals radius for argon as $r = 1.88 * 10^{-10}$m (see [Bon64]), $k_B = 1.38 * 10^{-23}$ J/K, $T = 300$ K and a pressure of $p = 5$ bar results in a mean free path of $\lambda = 1.32 * 10^{-8}$ m.

A useful parameter to look at the number of collisions in the nozzle is the Knudsen number. Its given by the mean free path λ_0 divided by the diameter of the nozzle D

$$Kn = \frac{\lambda_0}{D}. \tag{2.8}$$

With a nozzle diameter of $D = 2.5$ mm and the mean free path from before, this results in $Kn = 5.27 * 10^{-6}$. If $Kn \leq 1$ the molecules undergo a large number of collisions and exchange energy. For different Knudsen numbers different equations have to be used [Bej21]:

Regime	Knudsen number	Equations
Continuous regime	$Kn < 10^{-2}$	Euler
Creeping flow	$10^{-2} < Kn < 10^{-1}$	Navier-Stokes
Transient regime	$10^{-1} < Kn < 10$	Boltzmann
Free molecular regime	$Kn > 10$	Boltzmann

Table 2.1: Different regimes in dependence of the Knudsen number.

2.5 Isentropic flow equation derivation

To derive some useful dependencies for supersonic expansions, we will start with some assumptions. We assume that we have a perfect gas and an adiabatic process. Effects of gravity and viscosity are neglected. Assuming the compression and the following expansion of the gas is reversible, it follows from the second law of thermodynamics that this is a isentropic gas flow. The following derivation is based on [NASb]. Different approaches to derive the same equations can be found in [Bej21] and [PMA19].

First, the adiabatic index is introduced:

$$\gamma = \frac{c_p}{c_v} \tag{2.9}$$

c_p is the specific heat coefficient at constant pressure and c_v is the specific heat coefficient at constant volume. Using the relation $c_p - c_v = R$ (Mayer's relation) it follows

$$\frac{c_p}{R} = \frac{\gamma}{\gamma - 1}. \tag{2.10}$$

The equation of state is

$$p = \rho R T \tag{2.11}$$

and the differential change in entropy dS is given by

$$dS = c_p \frac{dT}{T} - R\frac{dp}{p}. \tag{2.12}$$

dT is the differential change in temperature and dp is the differential change in pressure. For an isentropic process $dS = 0$. It follows:

$$c_p \frac{dT}{T} = R\frac{dp}{p} \tag{2.13}$$

Now using the equation of state 2.11 as $R = \frac{p}{\rho T}$ in 2.13 it follows:

$$c_p dT = \frac{dp}{\rho} \tag{2.14}$$

or

$$\frac{c_p}{R} * d\left(\frac{p}{\rho}\right) = \frac{dp}{\rho} \tag{2.15}$$

Now equation 2.15 has to be differentiated resulting in:

$$\frac{c_p}{R} * \left(\frac{dp}{\rho} - p * \frac{d\rho}{\rho^2}\right) = \frac{dp}{\rho} \tag{2.16}$$

and

$$\left(\frac{c_p}{R} - 1\right) * \frac{dp}{p} = \frac{c_p}{R} * \frac{d\rho}{\rho}, \tag{2.17}$$

now using equation 2.10 in equation 2.17 to

$$\frac{1}{\gamma - 1} * \frac{dp}{p} = \frac{\gamma}{\gamma - 1} * \frac{d\rho}{\rho}, \tag{2.18}$$

which simplifies to

$$\frac{dp}{p} = \gamma * \frac{d\rho}{\rho}. \tag{2.19}$$

This gives us after integration:

$$(p/\rho)^\gamma = constant \tag{2.20}$$

We can determine the value of the *constant* by defining the total conditions as pressure p_t and density ρ_t when the flow is isentropically brought to rest.

$$(p/\rho)^\gamma = constant = (p_t/\rho_t)^\gamma \tag{2.21}$$

$$\frac{p}{p_t} = (\rho/\rho_t)^\gamma \tag{2.22}$$

Using now again the equation of state 2.11, we can define the total temperature:

$$\frac{\rho T}{\rho_t T_t} = (\rho/\rho_t)^\gamma \tag{2.23}$$

$$\frac{T}{T_t} = (\rho/\rho_t)^{\gamma-1}. \tag{2.24}$$

Now combining eq. 2.22 and eq. 2.24 to

$$\frac{p}{p_t} = (T/T_t)^{\gamma/(\gamma-1)}. \tag{2.25}$$

The enthalpy h of a gas is given by

$$h = cp * T \tag{2.26}$$

and the conservation of energy equation expressed as:

$$h_t = h + \frac{v^2}{2} \tag{2.27}$$

If we now use the Mach number that has already been introduced (eq. 2.5) and the speed of sound

$$v_s = \sqrt{\gamma \frac{p}{\rho}} = \sqrt{\gamma R T}, \tag{2.28}$$

and now substitute eq. 2.5 and eq. 2.26 into eq. 2.27

$$cp * T_t = cp * T + \frac{M^2 v_s^2}{2}. \tag{2.29}$$

Now substituting eq. 2.28

$$cp * T_t = cp * T + \frac{M^2 \gamma R T}{2} \tag{2.30}$$

and finally using $c_p - c_v = R$ (Mayer's relation), gives us the equation of isentropic temperature:

$$\frac{T_t}{T} = 1 + \frac{\gamma - 1}{2} M^2 \tag{2.31}$$

Using the relations 2.24 and 2.25 to obtain the equation of isentropic pressure and isentropic density.

$$\frac{p_t}{p} = \left(1 + \frac{\gamma - 1}{2} M^2\right)^{\gamma/(\gamma-1)} \tag{2.32}$$

$$\frac{\rho_t}{\rho} = \left(1 + \frac{\gamma - 1}{2} M^2\right)^{1/(\gamma-1)} \tag{2.33}$$

2.6 Choked flow

This section about the choked flow is based on [NASc]. The conservation of mass requires that the rate, at which mass enters a nozzle, must also be the rate at which it leaves. This leads to the continuity equation:

$$\dot{m} = \rho v A, \tag{2.34}$$

where $\dot{m}$ is the mass flow rate, ρ is the density, v is the velocity and A is the area through which the gas flows. If one now remembers the Mach number (eq. 2.5) and the speed of sound (eq. 2.3) we can derive

$$v = Mv_s = M\sqrt{\gamma RT}. \tag{2.35}$$

if we now substitute this into eq. 2.34, we get

$$\dot{m} = \rho AM\sqrt{\gamma RT}. \tag{2.36}$$

Now substituting the equation of states in the form of $\rho = \frac{p}{RT}$ gives us

$$\dot{m} = A\sqrt{\frac{\gamma}{R}}M\frac{p}{\sqrt{T}}. \tag{2.37}$$

Substituting the isentropic flow equation for pressure 2.32 that has been derived before into eq. 2.37 gives us

$$\dot{m} = \frac{Ap_t}{\sqrt{T_t}}\sqrt{\frac{\gamma}{R}}M\frac{T}{T_T}^{\frac{\gamma+1}{2(\gamma-1)}}. \tag{2.38}$$

Now using the isentropic flow equation for temperature 2.31 that also has been derived before and substitute this into eq. 2.38 we finally get (see [NASc])

$$\dot{m} = \frac{Ap_t}{\sqrt{T_t}}\sqrt{\frac{\gamma}{R}}M\left(1+\frac{\gamma-1}{2}M^2\right)^{-\frac{\gamma+1}{2(\gamma-1)}}. \tag{2.39}$$

This equation describes the flow rate of mass through an area dependend on the Mach number. While this looks a little bit complicated, it gets a lot more clearer if we look at a plot of this (see fig.: 2.3).

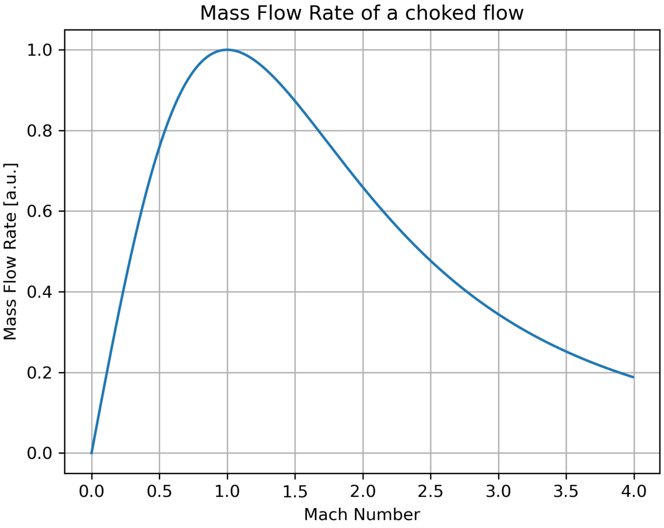

Figure 2.3: Mass flow rate for a choked flow. Plot of equation 2.39. The maximum is at M=1.

In figure 2.3 one can see, that equation 2.39 has a maximum at $M = 1$. At $M = 1$ the mass flow rate can be estimated by

$$\dot{m} = \frac{Ap_t}{\sqrt{T_t}} \sqrt{\frac{\gamma}{R}} \left(\frac{\gamma + 1}{2}\right)^{-\frac{\gamma+1}{2(\gamma-1)}} . \tag{2.40}$$

This means that a choked flow through a nozzle reaches a maximum velocity of the sound velocity. We have a subsonic flow before the nozzle. When the nozzle is small enough, the gas is compressed and reaches sonic speeds and undergoes a lot of collisions inside of the nozzle. After the nozzle, the gas expands adiabatically and reaches supersonic speed.

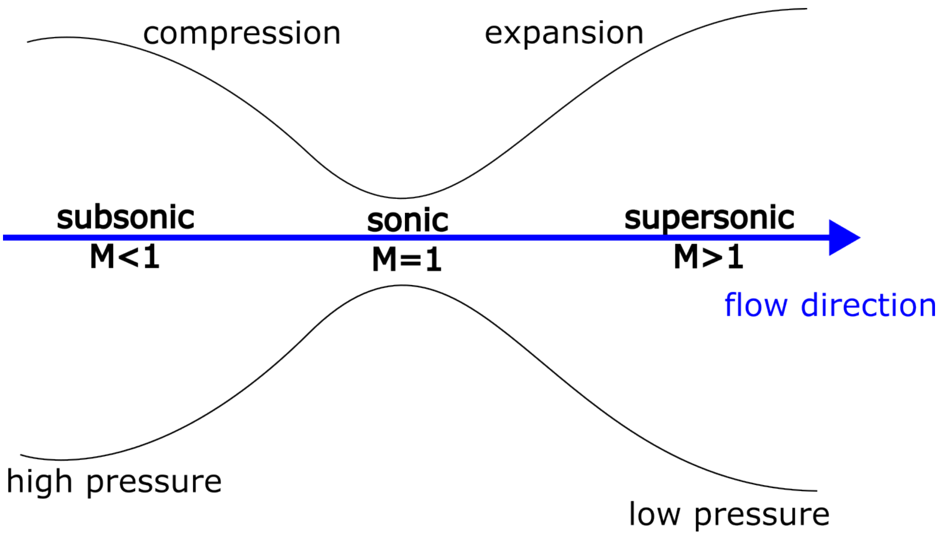

Figure 2.4: Choked flow. The flow is subsonic before the nozzle. The gas is then compressed and reaches sonic speed inside of the nozzle. After that, the gas expands adiabatically and supersonically.

Chapter 3

The ion source

Supersonic expansion is a proven way to produce cold molecules. However, we want to produce molecular ions and store them in a storage ring. Therefore we need an ion source to produce charged particles that can be manipulated with electric or magnetic fields. This chapter will give an introduction into the supersonic expansion ion source that was build and tested at the Max Planck Institute for Nuclear Physics (MPIK) in Heidelberg. The title of this thesis states a simple supersonic expansion source. The goal was to build a source that is relatively easy to rebuild.

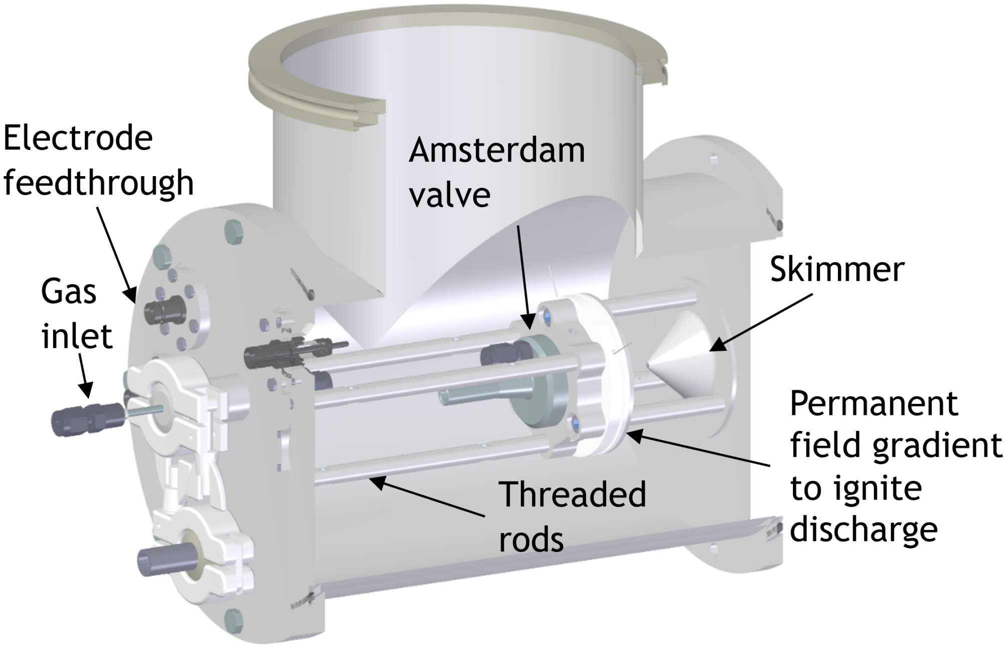

Figure 3.1: Simple supersonic expansion source based on the commercial available Amsterdam Piezo Valve ([Gru23]).

3.1 Pulsed valve

We need a relatively high density of ions in the storage ring to make a measurement. The flow through a nozzle can only be as fast as the speed of sound (see fig. 2.3). As we see in equation 2.40 the mass flow rate through a nozzle is mainly dependent on the nozzle diameter. Therefore we want to use a relatively large nozzle diameter in the ion source. Supersonic expansion relies on the large pressure difference between two regimes and the compression of the gas as it flows through a nozzle. For a large nozzle it is very hard to maintain this pressure difference because pumping reaches its limit. We used a pulsed valve and a nozzle with a diameter of 2.5 mm to produce high density pulses of ions, while still maintaining a pressure difference of 5 bar to 10^{-5} mbar.

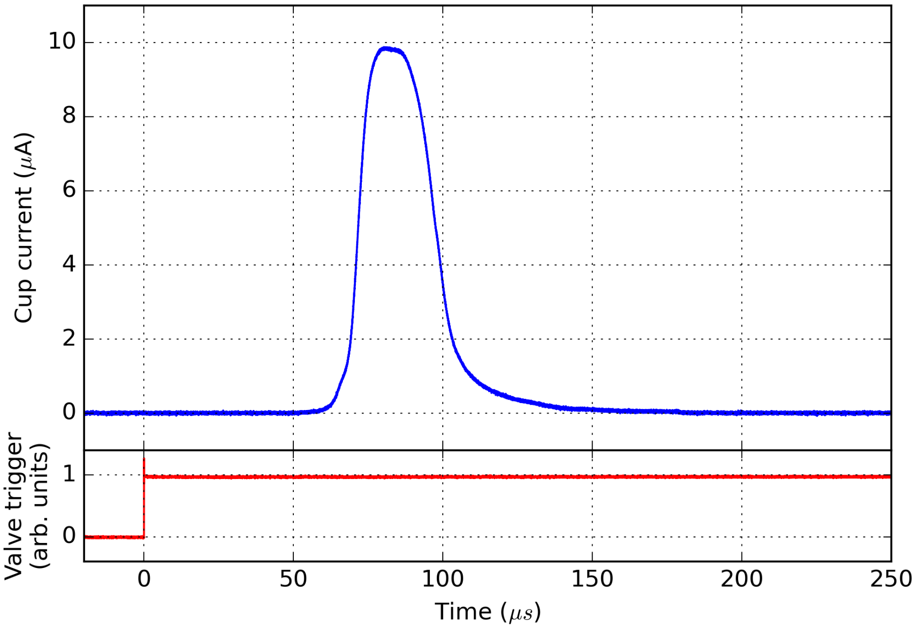

Figure 3.2: Shown is a pulse of 10 μA produced by the Amsterdam Piezo Valve. Discharge voltage 1910V, opening time 25 μs and pressure 1 bar ([Nue23]).

We used the commercial available Amsterdam Piezo Valve that is based on a flexing rod of a piezo material. It has opening times from 20 μs to continuum and was tested with a pressure of up to 5 bar. We were able to produce pulses of H_3^+ with up to 10 μA [Nue23].

3.2 Ionization

For ionization we used two electrodes that are inside of the nozzle. One of the electrodes is grounded and the other electrode is on a constant voltage at about 1 kV. When the Amsterdam Piezo Valve opens, the changing density triggers a discharge between the electrodes and ionizes the gas.

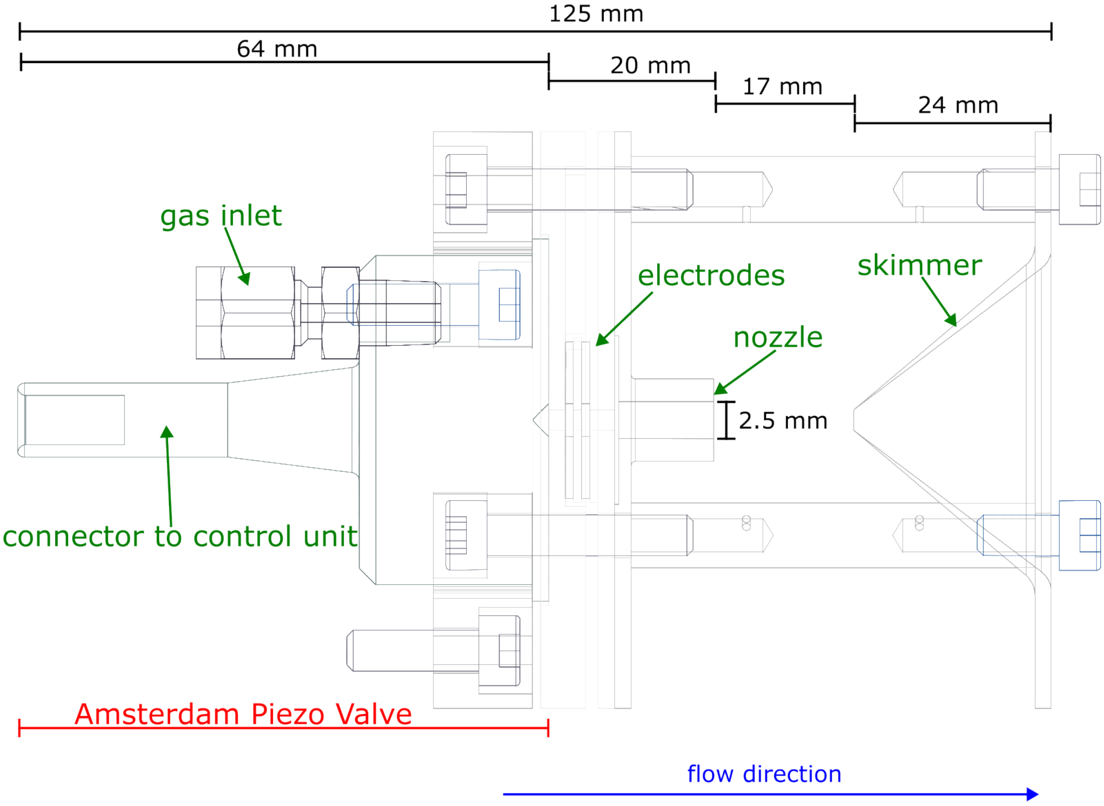

Figure 3.3: A drawing of the supersonic expansion ion source. Visible are the electrodes that ionize the gas. One is on ground potential and the other is on a static high voltage ([Gru23]).

The electrodes are on a constant voltage and the discharge is triggered by the gas pulse. When the discharge burns, high currents flow for a short period of time. To cushion the current peaks we used a capacitor of 1 μF. However, when we measured the voltage of the discharge operating the ion source with pulses every 100 ms and at a voltage of 300 V, one can see that the voltage breaks down below 50 V (see fig.: 3.4). After this, the capacitor is recharged. This takes so much time that 100 ms after the first pulse the voltage is too low for a discharge in the second pulse (see fig.: 3.4).

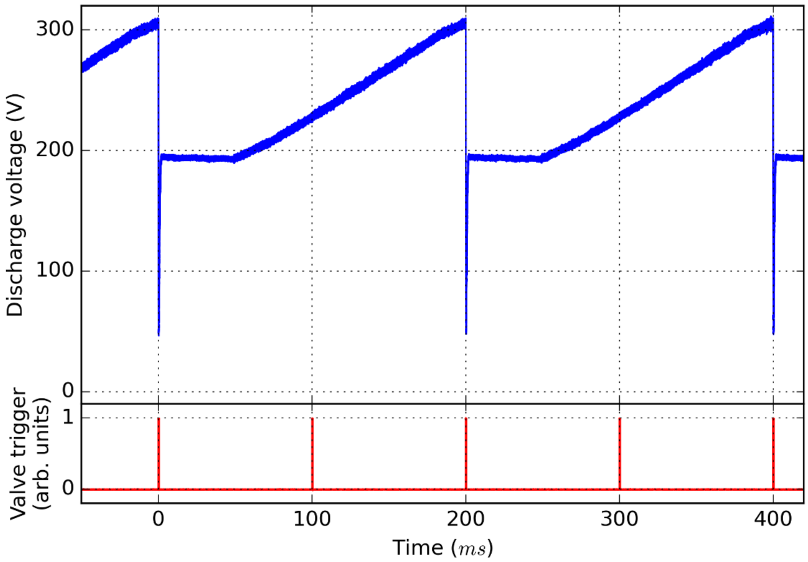

Figure 3.4: The Amsterdam Piezo Valve is operated with a pulse every 100 ms and a discharge voltage of 300 V is used. [Nue23]

Looking into the breakdown of the voltage, we were able to approximate the current. He estimated that at a Voltage of 350 V a current of 24 ± 7 A flows. We need currents of about $I_{discharge} = 1$ A, but we want to have the discharge burning as long as gas flows through the nozzle. A small circuit with a limiting resistor was developed to limit the current to $I_{discharge} = 1$ A and the decrease of the discharge voltage to approx. 10 %.

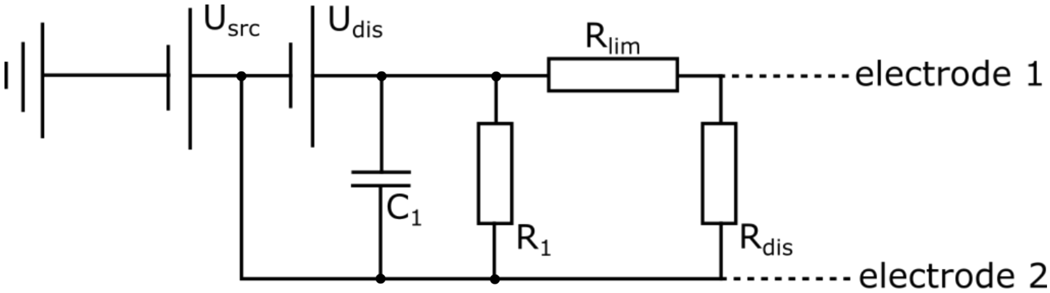

Figure 3.5: Circuit to limit the current in the discharge. The capacitor cushions the peaks in the currents. R_{lim} limits the current and R_1 is used to discharge the capacitor when the device is powered off. U_{dis} is the discharge voltage and U_{src} is the acceleration voltage. Parameters: $U_{dis} = 0.4$ kV to 1.2 kV, $R_{lim} = 1.25$ kΩ, $C_1 = 1$ μF and $R_1 = 1$ MΩ ([Nue23]).

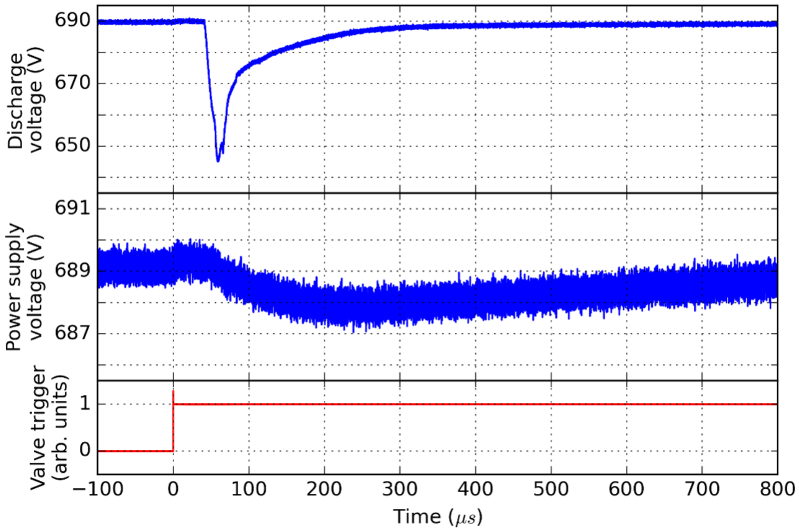

Figure 3.6: Shown is the discharge voltage and power supply voltage when the valve is triggered. Using the circuit we were able to stabilize the discharge voltage ([Nue23]). The supersonic expansion ion source can be operated with commercially available power supplies. Note that the y-axis for the discharge and the power supply voltage does not start at zero.

3.3 Conclusion

The supersonic expansion source is a pulsed ion source that is based on a commercial Piezo Valve and uses a constant voltage and electrodes to produce a discharge that ionizes the gas. The discharge is triggered by the valve and with the introduced circuit, commercially available power supplies can be used. Therefore this source is relatively easy to rebuild.

Chapter 4

Limitations

The ideal supersonic expansion and the ion source have already been introduced. However, some assumptions that were used in the ideal supersonic expansion do not hold for the used ion source. This chapter will give an insight into the limitations and broken assumptions.

If we look again at equations 2.31, 2.32 and 2.33

$$\frac{T_t}{T} = 1 + \frac{\gamma - 1}{2} M^2 \tag{4.1}$$

$$\frac{p_t}{p} = \left(1 + \frac{\gamma - 1}{2} M^2\right)^{\gamma/(\gamma-1)} \tag{4.2}$$

$$\frac{\rho_t}{\rho} = \left(1 + \frac{\gamma - 1}{2} M^2\right)^{1/(\gamma-1)} , \tag{4.3}$$

we can estimate the temperature an ideal supersonic expansion should yield. The supersonic expansion ion source has been tested with a pressure up to $p_t = 5$ bar and the gas expands in a regime with a pressure of approx. $p = 10^{-5}$ mbar. If we put those numbers into eq. 2.32 and use the adiabatic index of argon ($\gamma \approx 1.7$ (see Nist Database [Nata])), we can calculate a Mach number of $M \approx 104$. If we now put in this Mach number into equation 2.31 and assume we start with $T_t = 300$ K, we can calculate a temperature of $T \approx 0.08$ K. While we were never able to reach temperatures this low with our ion source, there are papers like [Luo+93], [CRE06] and [Wan+88] that report that they have reached temperatures in the mK range with supersonic expansions. Let's therefore take a closer look at the limitations that affect our supersonic ion source.

It is assumed that collisions occur with sufficient frequency for equilibrium to be maintained between the internal degrees of freedom throughout the expansion process. But as the gas expands, the density decreases and less and less collisions take place leading to an imbalance in the internal degrees of freedom (see [Mor96] and [Bej21]). The efficiency of the cooling is determined by the efficiency of energy transfer in the degrees of freedom and is given in the order of translational > rotational > vibrational [IMV03]. Therefore, the molecules are not necessarily populated in a Maxwell-Boltzmann distribution, and high vibrational levels can still be populated. Luckily vibrations cool relatively fast radiatively in the storage ring (see [OCo+16] and [AZF94]).

4.1 Terminal Mach number

The conversion of thermal energy into directed kinetic energy requires collisions among the molecules. With increasing distance from the nozzle exit the density of the gas decreases. With density of the gas also the amount of collision drops, limiting the reachable Mach number independently of the pressure in the low pressure regime.

$$M_t = G\left(\frac{1}{\epsilon}Kn\right)^{-(\gamma-1)/\gamma} \tag{4.4}$$

with G as a constant and ϵ as collisional effectiveness (see [Mor96]). For argon it could be shown that $G = 2.05$ and $\epsilon = 0.25$ ([AF65]). With the Knudsen number that has already been calculated (see eq. 2.6) and $\gamma_{argon} = 1.7$ ([Nata]), the terminal Mach number can be calculated to $M_t = 173$.

4.2 Pulsed sources

A pulsed source is a good compromise to get a high density of ions while still maintaining the pressure difference between the reservoirs. However, for the derivation of the equations 2.31, 2.32 and 2.33 it was assumed that a continuous gas flow was given. To still assume a continuous flow, the opening time of the valve has to be long enough for a supersonic expansion to fully develop. A good rule of thumb given in [Mor96] is

$$\Delta t \geq 4\frac{D}{v_s} \tag{4.5}$$

where D is the nozzle diameter and v_s is the speed of sound of the used gas in the reservoir.

The supersonic expansion ion source has a nozzle diameter of $D = 2.5$ mm. For argon the sound velocity can be calculated with equation 2.3 using an adiabatic index of argon of $\gamma \approx 1.7$ ([Nata]) and a molecular mass of $m_{mol} \approx 40$ g/mol. It results $v_s \approx 326$ m/s.

Using this in equation 4.5 results in an opening time of $\Delta t \approx 30\ \mu$s. This is in the same order of magnitude as the minimal opening time of the supersonic expansion valve ($\Delta t = 20\ \mu$s).

4.3 Prandtl-Meyer equation

An isentropic centered expansion process can be called Prandtl-Meyer expansion. This section is based on [NASa].

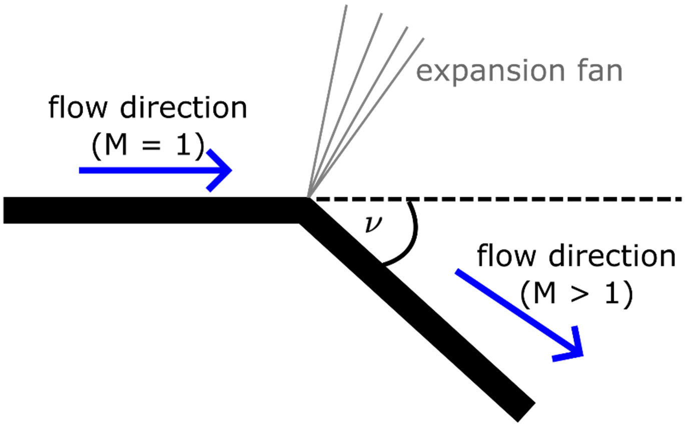

Figure 4.1: A sonic flow of a compressible fluid is flowing over a surface. When the flow turns around a convex corner, the fluid expands and a Prandtl-Meyer expansion fan is produced (cf. [NASa]).

When a sonic flow of a compressible fluid is turned around a convex corner, an expansion fan is formed. The Mach number of the gas increases while temperature, static pressure and density decrease. The expansion fan consists of an infinite number of weak pressure waves and it is an isentropic process. The Prandtl-Meyer equation gives a relation of the Mach number to the angle ν by which the flow is turned:

$$\nu = \sqrt{\frac{\gamma+1}{\gamma-1}} \arctan \sqrt{\frac{\gamma-1}{\gamma+1}(M^2-1)} - \arctan \sqrt{(M^2-1)} \tag{4.6}$$

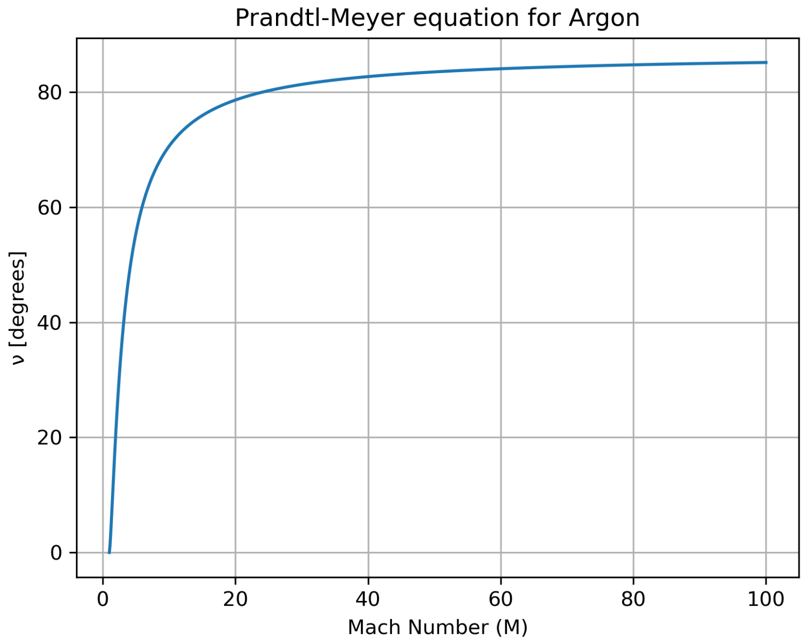

Figure 4.2: Plot of equation 4.6 for argon ($\gamma = 1.7$)

The Mach number is a function of the speed of sound (eq. 2.5: $M = \frac{u}{v_s}$). The speed of sound is dependent on the properties of the fluid (eq. 2.3: $v_s = \sqrt{\gamma RT}$). If the temperature of the fluid goes to zero, the speed of sound also goes to zero. Thereby even for finite velocities of the fluid, the Mach number can go from 0 to ∞.

One can calculate a maximum angle ν by which the flow can be turned when the Mach number goes to infinity

$$\nu_{max} = \frac{\pi}{2}\left(\sqrt{\frac{\gamma+1}{\gamma-1}} - 1\right). \tag{4.7}$$

Using the γ of argon as before, the maximum angle for argon can be calculated
$\nu_{max} \approx 87°$.
For large ν the flow turns not enough to be parallel to the wall. In this case a shear layer is observed. A rectangular nozzle is used in the supersonic expansion ion source and the jet undergoes a free jet expansion.

4.4 Shock waves

A shock wave is a thin propagating disturbance that moves faster than the local speed of sound. Properties of a gas change by a large amount and static pressure, temperature and density increase almost instantaneously. Shock waves should not be mistaken as expansion fans. Shock waves are irreversible (not isentropic) and the Mach number decreases, while expansion fans are reversible (isentropic) and the Mach number increases (see [NASd]).

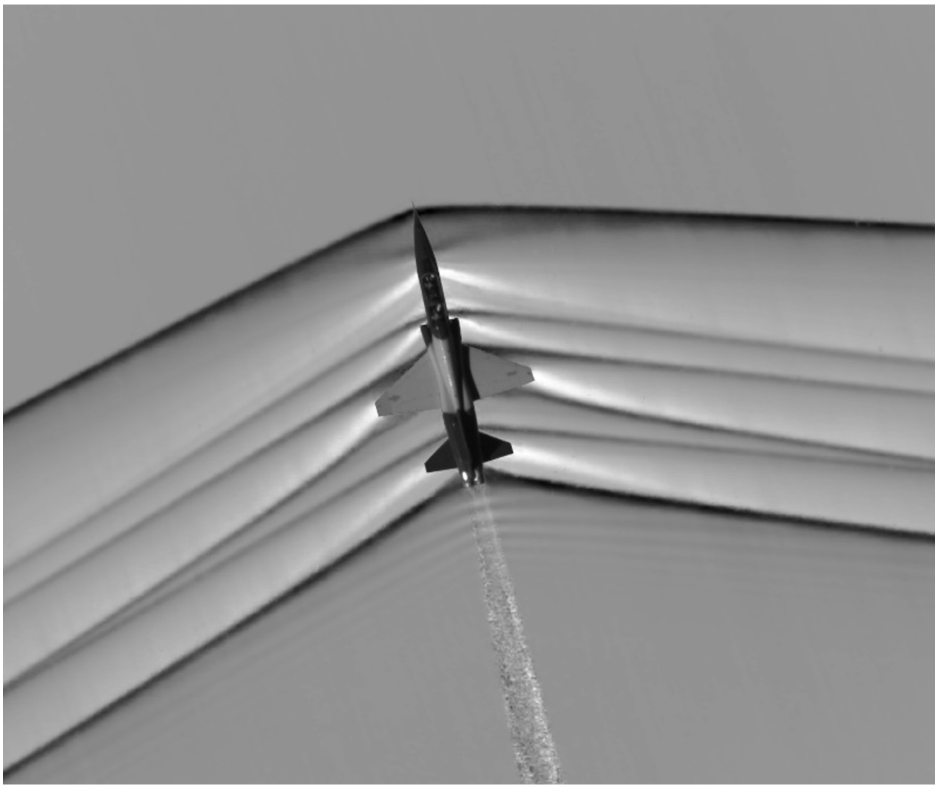

Figure 4.3: Shock waves generated by an aicraft moving faster than the local speed of sound. The shock waves are visible thanks to Schlieren photography (from [NASf]).

4.5 Mach disks

In the supersonic expansion the gas is compressed when it flows through the nozzle. Exiting the nozzle, we have an underexpanded jet that expands into a regime of low pressure. This results in an expansion fan on the lip of the nozzle. Those expansion waves are then reflected on the free jet boundary and turn back inward as compression waves and a compression fan. The flow is then recompressed by those compression waves. If the compression waves are strong enough, they can add up to an oblique shock wave (the barrel shock due to cylindrical form of the nozzle). For high pressure ratios, the flow attains a very low pressure during expansion that can not be balanced with just an oblique shock and a Mach disk appears. A Mach disk is a nearly flat normal shock wave perpendicular to the flow direction (see [Bej21] and [WM08]). Dependent on the upstream pressure this can be repeated multiple times.

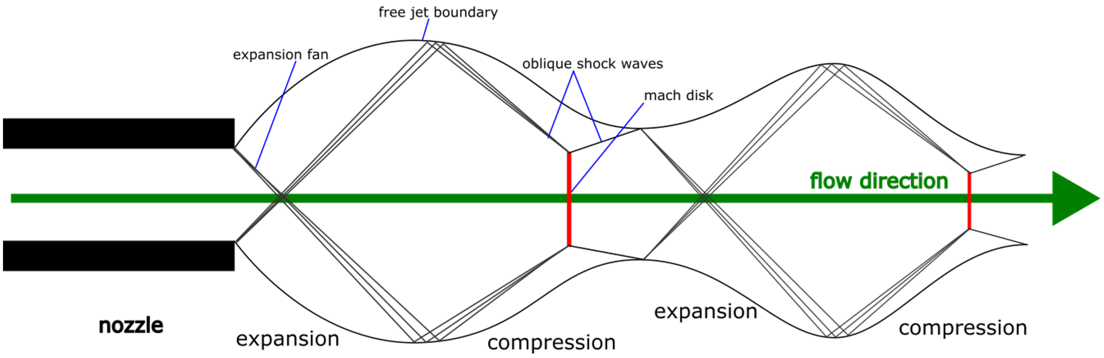

Figure 4.4: Mach disks (cf. [WM08]).

Some aircrafts, like the Lockheed SR-71 are build to fly at high altitudes. The jet engines are therefore adapted to the pressure conditions at high altitudes and produce an over-expanded jet at sea level. This is a similar process to the under-expanded jet that starts with an oblique shock wave instead of an expansion fan. The oblique shock is generated because the pressure of the ambient atmosphere is higher than the pressure in the jet. As before, a mach disk is formed before the flow expands again with an expansion fan. The mach disk however is a regime with high pressure and density and can reignite excess fuel making it visible (see fig.: 4.5).

Figure 4.5: The Lockheed SR-71 with visible Mach disks due to an overexpanded jet (from [NASe].

For a moderately underexpanded jet (pressure ratio: $2 < p_t/p < 4$) no mach disk is formed. Oblique shocks and expansion waves can repeat themselves multiple times. For a highly underexpanded jet (pressure ratio: $4 < p_t/p < 7$) a mach disk is formed and the process can also repeat itself multiple times. For an extremely underexpanded jet (pressure ratio: $p_t/p > 7$) only one single shock cell is formed (see fig.: 4.6).

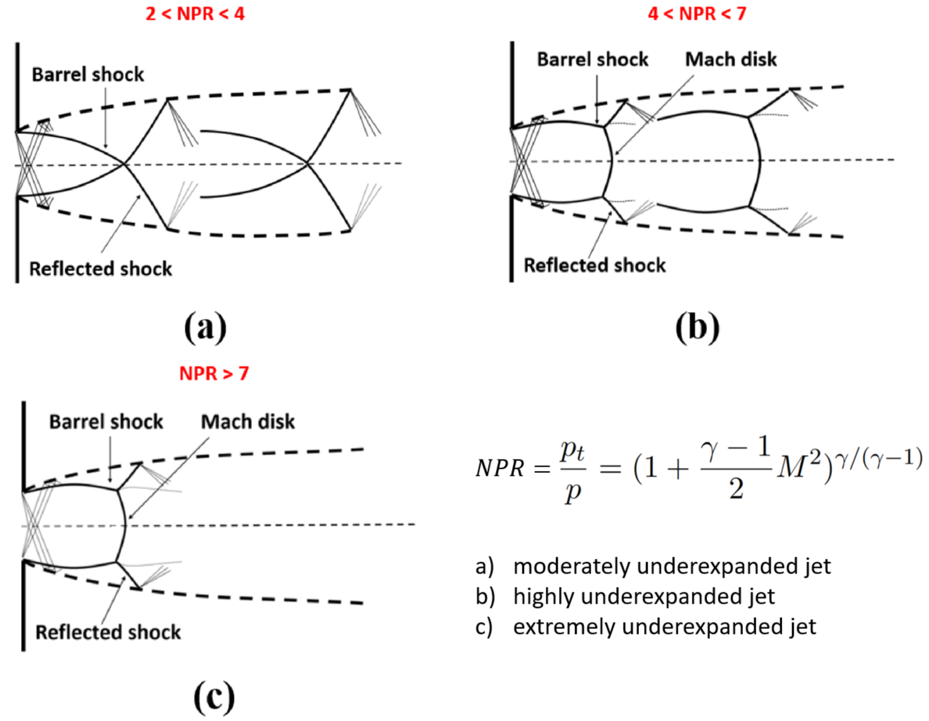

Figure 4.6: Underexpanded jets for different pressure ratios $\frac{p_t}{p}$. With permission to use from [Ana+22].

In our case we have a pressure ratio of $p_t/p \approx 10^8$ and an extremely underexpanded jet. Therefore we want to look closer into the single shock cell that is formed.

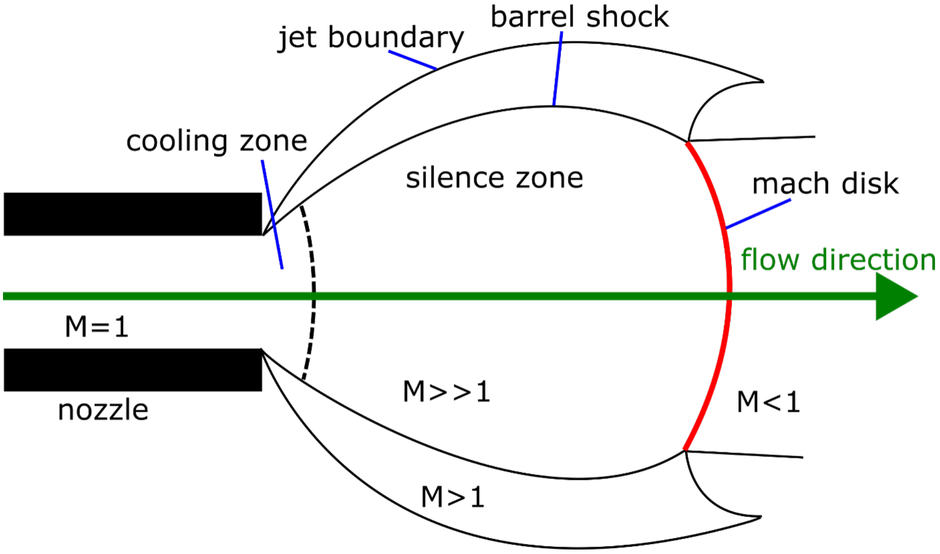

Figure 4.7: A single shock cell formed by the expansion of an extremely underexpanded jet. (cf. [Bej21]).

The shock cell consists of a barrel shock terminated by a Mach disk. Inside of the shock cell there are different regions. Directly in front of the nozzle is the cooling zone. In the cooling zone the collisions take place, monochromatize the velocities and cool down the gas. The second region in flow direction is the so-called zone of silence. The speed of sound is nearly zero and the flow is supersonic ($M >> 1$). In this area fewer collisions take place and molecules can be treated as isolated ones (free molecular flow regime).

For equations 2.31, 2.32and 2.33 we assumed an isentropic process. For an extremely underexpanded jet and a free expansion, a barrel shock and a mach disk are produced. Shock waves are irreversible so the assumption of an isentropic gas flow seems to be broken. However, one can assume that for particles in the silence zone the isentropic assumption still holds ([Bej21] and [Mor96]). To select only particles out of this region, a skimmer is used (see fig. 3.1).

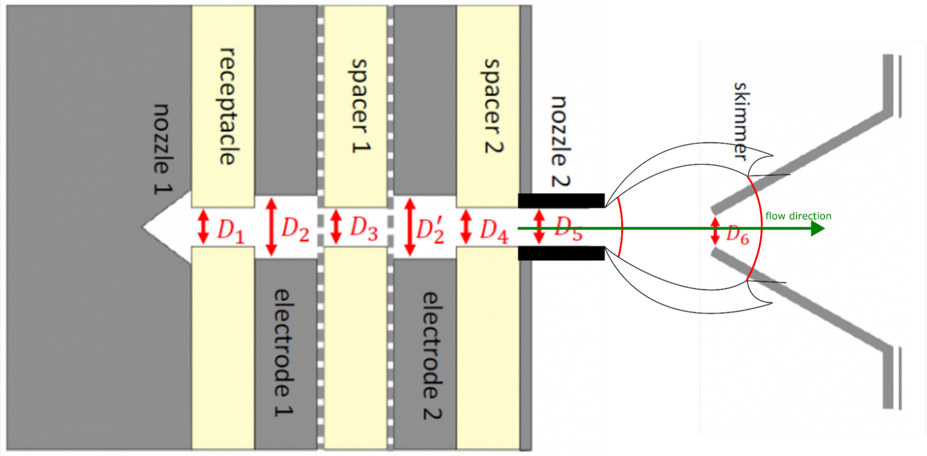

Figure 4.8: The supersonic expansion source with electrodes. A barrel shock is shown on the nozzle exit. The skimmer is used to select particles out of the silence zone ([Nue23]).

D_1	D_2	D_3	D_2'	D_4	D_5
2.5 mm	4 mm	2.5 mm	4 mm	2.5 mm	2.5 mm

Table 4.1: Dimensions shown in fig. 4.8.

4.6 Turbulence

The Reynolds number is a good indicator to estimate if turbulence is abundant. *Re* is a dimensionless quantity that represents the ratio of inertial and viscous forces, given by

$$Re = \frac{\rho v D}{\mu}, \tag{4.8}$$

where ρ is the density, v is the flow speed, D is the nozzle diameter and μ is the viscosity. For a $Re < 2000$ the flow is laminar, for $2000 < Re < 3000$ the flow is inertial and if $Re > 3000$ the flow is turbulent (see [Bej21]).

As shown in figure 2.3 the speed of the jet flowing through the nozzle is equal to the speed of sound. For argon this has already been calculated to be $v_s = 326 \ \ \mathrm{m/s}$ at $T = 300$ K. Assuming a temperature of 300 K and a pressure of 5 bar at the nozzle entry, one finds a density for argon of $\rho = 8.0319 \ \mathrm{kg/m^3}$ and a viscosity of $2.2810 * 10^{-5}$ Pa*s in the Nist database ([Nata]). With a nozzle diameter of $D = 2.5$ mm, the Reynolds number can be calculated to be $Re_{nozzle} \approx 2.9 * 10^5$. This is a rough estimate at the entry of the nozzle. However, it shows that in our supersonic expansion ion source $Re >> 3000$ and turbulence is abundant. The design of the nozzle itself could also pronounce turbulence, since the nozzle is not smooth due to the recessed electrodes (see fig. 4.8).

For the derivation of equations 2.31, 2.32 and 2.33 we neglected effects of viscosity. For our supersonic expansion ion source this assumption is not given.

4.7 Ionization by discharge

To store the particles in the ring, they have to be ionized. In the supersonic expansion ion source the ionization is done with a discharge between two electrodes inside of the nozzle (see fig. 4.8). In Chapter 2 we assumed an adiabatic process which is not the case for a discharge in the nozzle. Looking at equation 2.31 the initial temperature T_t might be a lot higher than room temperature because of the discharge, resulting in a higher temperature after the expansion.

The ion source produces a mix of ions and neutral particles. This allows for ion-neutral chemistry. The ion can induce a dipole moment in the neutral particle resulting in an attractive force between the ion and the neutral particle [SB08]. Often there is no energetic barrier to ion-neutral reactions [Tsi+22].

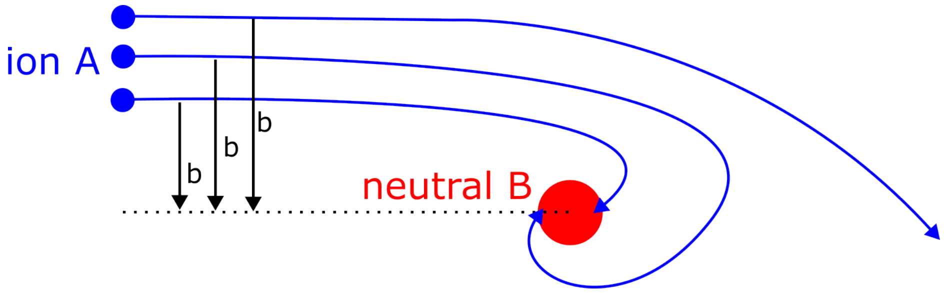

Figure 4.9: The path of an ion A in the the attractive potential due to the induced dipole moment in the neutral B. b is the impact parameter.

The potential V_{eff} can be described with the following equation:

$$V_{eff} = \frac{-1}{8\pi\epsilon_0}\frac{e^2\alpha}{r^4} + E_{kin}\left(\frac{b}{r}\right)^2 \tag{4.9}$$

α is the polarizability of the neutral particle, r is the distance between the particles, b is the impact parameter (see fig. 4.9) and E_{kin} is the kinetic energy of the Ion. The first part of equation 4.9 describes the charge induced dipole potential and the second part describes a centrifugal potential (see [Tsi+22]). A critical impact parameter b_{crit} can be calculated for reactions to happen (see [SGM14]).

$$b_{crit} = \sqrt[4]{\frac{e^2\alpha}{2\pi\epsilon_0 E}} \tag{4.10}$$

A Langevin rate coefficient can be calculated (see [Tsi+22]).

$$k_L = e\sqrt{\frac{\pi\alpha}{\epsilon_0\mu}}, \tag{4.11}$$

where μ is the reduced mass. Note that this rate coefficient is independent of energy E and temperature T.

A drawback of the theory is, that it does not account for interactions that happen when the collision partners are close to one another [Tsi+22]. Also the shown theory does not take into account that the rates of ion-neutral reactions are often enhanced at low temperatures [Tsi+22]. Quantum mechanical effects are neglected.

4.8 Cluster

Supersonic expansions are known to produce clusters from earliest investigations (see [Mor96]). It requires three-body collisions to form clusters because the third body has to carry off energy. The total number of binary collisions during a supersonic expansion is proportional to $p_0 D$ where p_0 describes the pressure in the high pressure regime and D describes the nozzle diameter [Mor96]. The total number of three-body collisions is proportional to $p_0^2 D$. Thus forming clusters is maximised for small nozzle diameters and high pressures of p_0. Nitrous oxide is known to react with itself and form clusters (see [Gau88] and [Pot+97]). Forming clusters in our experiment results in less ions in the laser interaction zone because everything but N_2O^+ is filtered out. Formation of cluster could also affect the cooling because the third body in the three body interaction carries energy from the collision.

4.9 Charged particles

Supersonic expansion relies on collisions of particles that translate unordered internal energy into kinetic energy. For ions, however, there are electrical forces and a repulsion of particles. This could affect the final temperature after expansion.

4.10 Interaction with background gases

The idealized continuum model will also break down when the expanding gas reaches a density in the order of the background gas. Collisions with the background gas will randomize the velocity distribution and the expansion will become an irreversible process (not isentropic).

Chapter 5

Measuring temperature

As shown in the previous chapter, there are a lot of limitations to the idealized continuum model and the estimates from equations 2.31, 2.32 and 2.33 probably do not hold. Therefore, we need to measure the internal temperature of the molecular ions produced, in our supersonic expansion ion source.

5.1 Resonant photodissociation

Molecules have electronic, vibrational and rotational states, giving rise to an rovibronic spectrum. The vibration as well as the rotation are quantized and the states can be described by the vibrational quantum number v and the rotational quantum number J. Changes of rotational energy levels are typically much smaller than changes in vibrational energy and give a fine structure to the vibrational spectrum. Electronic transitions are even larger in energy than vibrational transitions. Transitions are categorized in branches. For excitations with only one photon (dipole transitions) only $\Delta J = 0, \pm 1$ are possible. A vibrational transition with the same rotational quantum number ($\Delta J = 0$) is visible in the spectrum as Q-branch. For some molecules Q-branches are supressed. When $\Delta J = +1$ it is visible as R-branch. The R-branch is on the higher wavenumber side of the Q-branch. The P-branch is on the lower wavenumber side and describes a transition where $\Delta J = -1$.

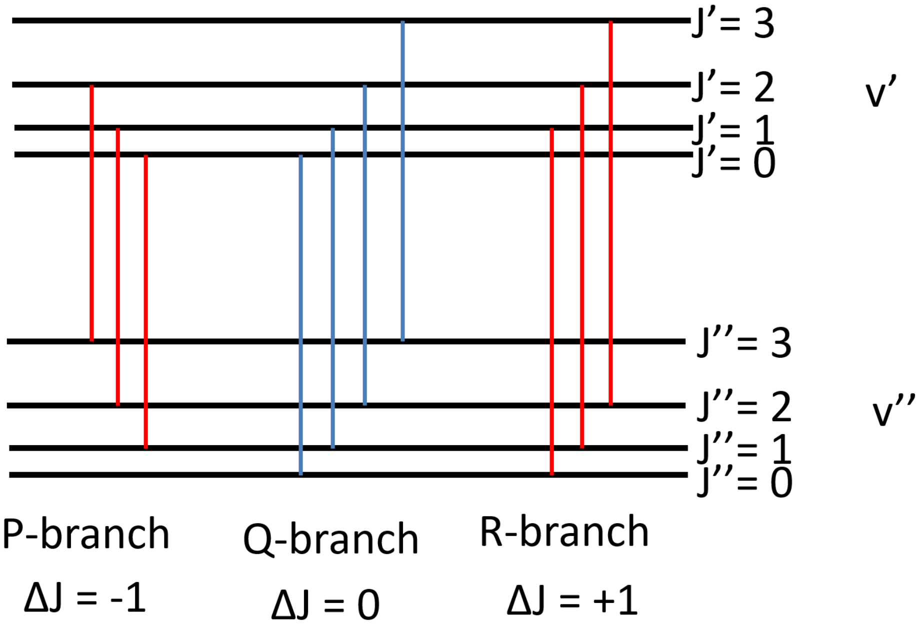

Figure 5.1: The transitions in dependency of v and J that are represented in the spectrum as P-, Q- and R-branch.

In the resonant photodissociation a photon is absorbed by a molecule. The molecule is then excited by this photon into a state above the dissociation limit. After that the molecule dissociates into fragments. The excitation into the state above the dissociation barrier is a resonance condition and the energy of the photon has to match the transition energy. Therefore, absorption of photons with energy $E = hf$ is related to the number of molecules in the right vibrational quantum number v and rotational quantum number J. This is dependent on the internal temperature of the molecule. Measuring the amount of molecules that dissociate in dependency of the energy of the photon gives a temperature dependent spectrum with characteristic shapes of the P- and R-branches.

5.2 Notation

$$\tilde{\Theta}^{2S+1}\Lambda^{(+/-)}_{(u/g)}(000)$$

Explanation	
Θ	X labels the electronic ground state. A, B, C label states with the same multiplicity as the ground state. a, b, c label states with different spin multiplicity compared to the ground state.
S	The spin quantum number.
Λ	The projection of orbital angular momentum along the internuclear axis.
(u/g)	The parity. (inversion operation)
$(+/-)$	The reflection symmetry.
$\tilde{\Theta}$	In polyatomic molecules (not diatomic) a tilde is added.
(000)	The vibrational quantum numbers of the state. In this thesis for N_2O the convention by Herzberg is used. v_1 corresponds to the higher frequency $N-N$ σ^+ stretch, v_2 corresponds to the π bend and v_3 to the lower frequency $N-O$ stretch (see section 5.3) [Bej+21].

Table 5.1: Shown is the notation that characterizes the state of the molecule.

5.3 The nitrous oxide cation

N_2O^+ is a linear triatomic molecular ion with a central N atom. Due to its linear structure it has two rotational degrees of freedom. There are three vibrational degrees of freedom ($NN-O$ stretching, $N-NO$ stretching and bending). The N_2O^+ ion has been extensively investigated in the literature (see [Bej+21] for details).
The rovibronic band $\tilde{A}^2\Sigma^+(002) \leftarrow \tilde{X}^2\Pi_{3/2}$ is one of the most intense in the spectral range (30500 cm^{-1} to 32500 cm^{-1}) of the frequency doubled pulsed dye laser used for the present work (see [Bej+21]) and has already been recorded at high resolution (see e.g. [Hir+20] and [Bej+21]). In Detail, we want to look at the photodissociation process

$$N_2O^+(\tilde{X}^2\Pi(000)) \xrightarrow{\text{exc.}} N_2O^+(\tilde{A}^2\Sigma^+(002)) \xrightarrow{\text{diss.}} NO^+(\tilde{X}^1\Sigma^+) + N(^4S) \tag{5.1}$$

that has been characterized to be in the 30885 cm^{-1} to 30940 cm^{-1} range (see [Wan+10]).

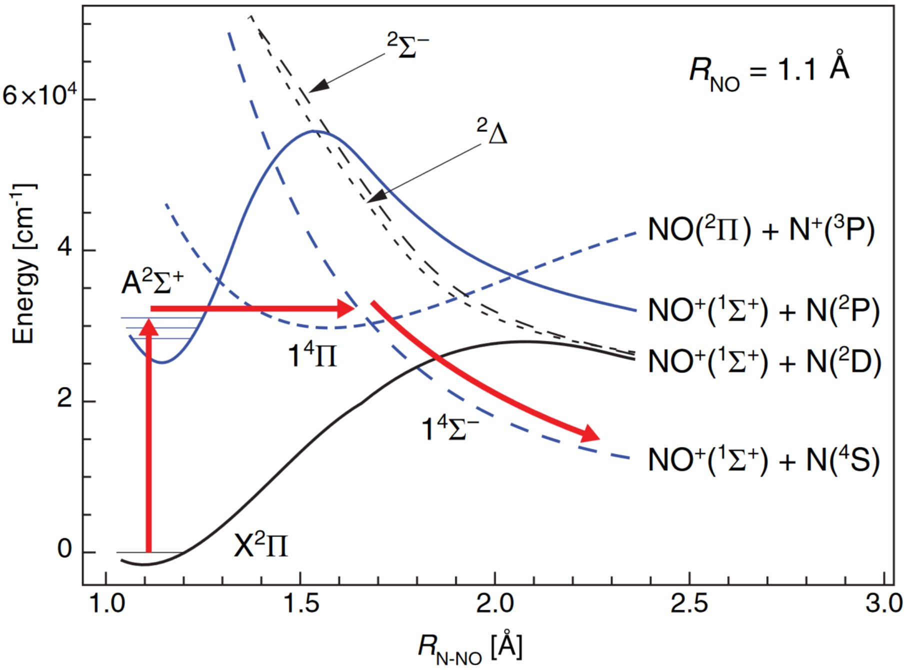

Figure 5.2: Photodissociation process N_2O^+ described by equation 5.1. N_2O^+ is excited above the dissociation limit by a UV photon. The molecule dissociates into NO^+ and N. With permission to use from [Hir+20].

5.4 Temperature dependent simulated spectrum

The simulation of the photodissociation spectrum (see eq. 5.1) was done by Joffrey Fréreux using the PGOPHER software and spectroscopic parameters from [Fel13] (ground state) and [FKS82] for the $\tilde{A}^2\Sigma^+(002)$ state.
The simulated spectra for $T = 20$ K, $T = 35$ K, $T = 70$ K and $T = 500$ K are shown in fig. 5.3. The peak at 30908 cm^{-1} is the Q-branch. The R-branch is on the higher wavenumber side and the P-branch is on the lower wavenumber side. The peak at approx. 30890 cm^{-1} is only visible for high temperatures. The valley at approx. 30910 cm^{-1} is only visible for low temperatures. The R-branch shows different structures for different temperatures. From fitting this simulated spectrum on a measured spectrum, one can deduct the internal rotational temperature.

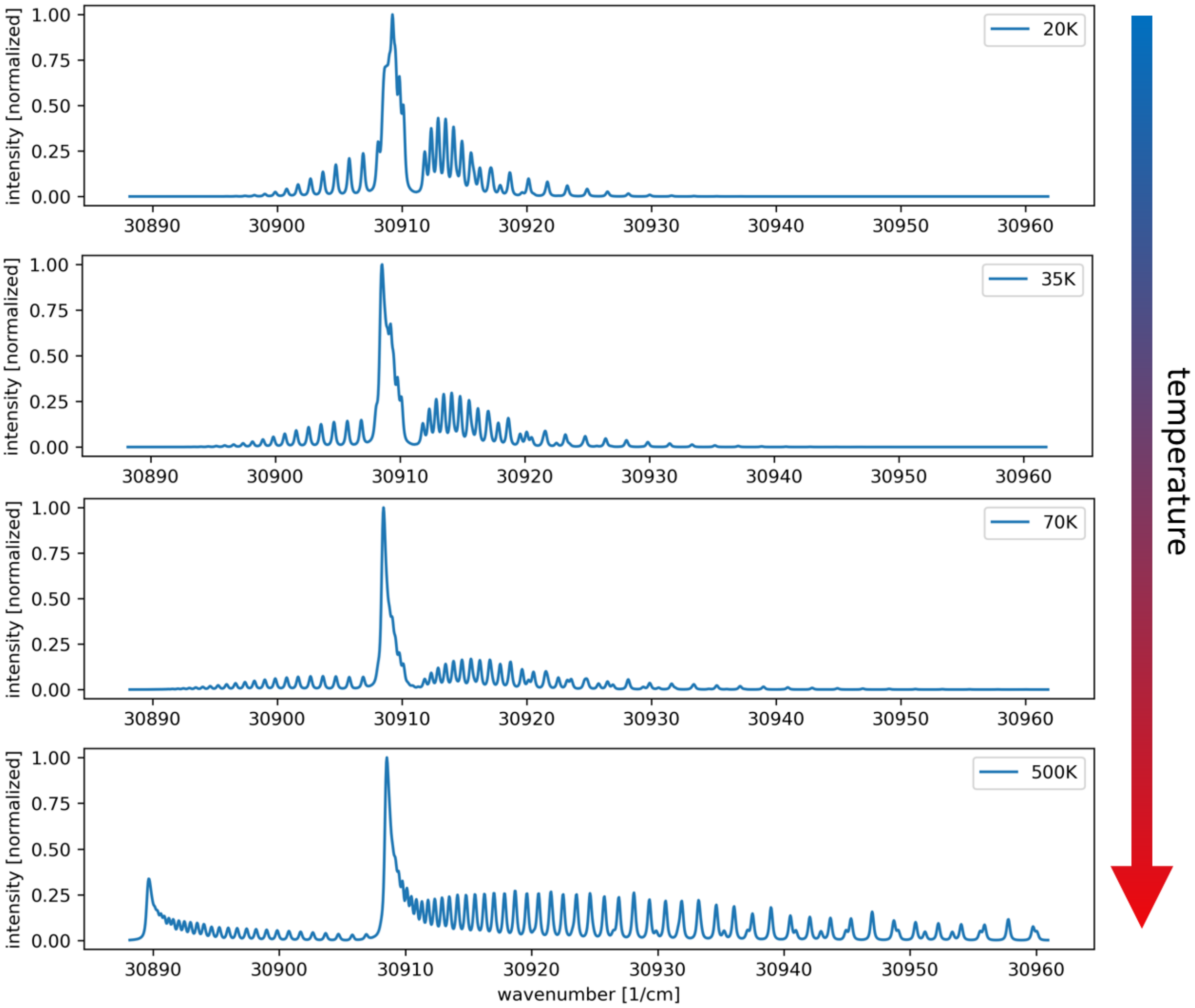

Figure 5.3: Simulated photodissociation spectra

Chapter 6

STARGATE

Since we now have a simulated temperature dependent spectrum of the photodissociation process to compare measured data to, the setup that was used to measure that data will be introduced in the following. STARGATE stands for **S**pectroscopy of **T**ransient **A**nions and **R**adicals by **G**ated and **A**ccelerated **T**ime-of-flight **E**xperiment and is a spectrometer at the Université Catholique de Louvain in Belgium that can measure high-resolution photodissociation spectra of mass-selected ions. This chapter is based on [Bej+21] and [Bej21].

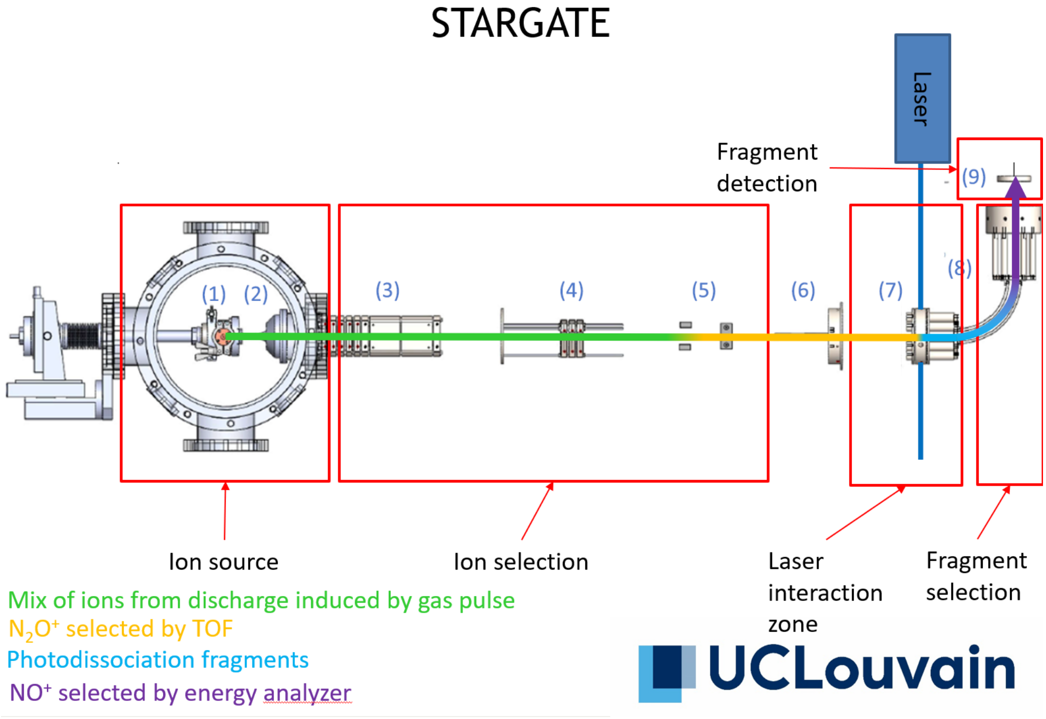

Figure 6.1: Setup of STARGATE. (c.f. [Bej+21]).

6.1 Ion production and ion selection

The supersonic expansion ion source (see chapter 3) was shipped to Belgium and installed in the setup of STARGATE. The ions that are produced in this source are accelerated to a kinetic energy of $E_{kin} = 1$ keV. A conical electrode placed after the grounded skimmer is used to accelerate and focus the ion beam. Six aluminum ring electrodes that are connected via 100 kΩ are used to provide a smooth acceleration potential and also forming an electrostatic lens (see fig. 6.2).

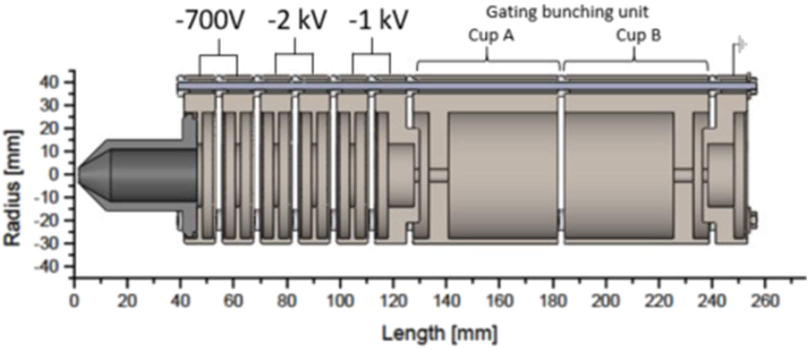

Figure 6.2: Acceleration scheme used at STARGATE ([Bej+21]).

The selection of the ions that are let into the laser interaction zone is done with a time-of-flight measurement. To improve the mass resolving power (MRP) $R = m/\Delta m$ the ions are bunched and gated to provide a $t = 0$ and reduce the dispersion Δt for the same m/z. This is done by two cup-like electrodes A and B (see fig. 6.2). Initially both cups are at the acceleration voltage. A last grounded electrode stops and reflects the ions and acts as a gate. Then Cup A is switched to +400 V and acts as a closed gate to the ring electrodes while also accelerating the ions that are lagging behind in the cup. Cup B is switched to 0 V and the ions can enter the drift tube. Fast HV push-pull switches with rise times of 20 ns are used and a tunable delay in the order of 40 ns is used between Cup A and B (see fig. 6.3 where this process is shown). Three electrodes, the one in the middle biased on 650 V and the outer two electrodes on ground potential, are used to refocus the ion beam (see (4) in fig.: 6.1).

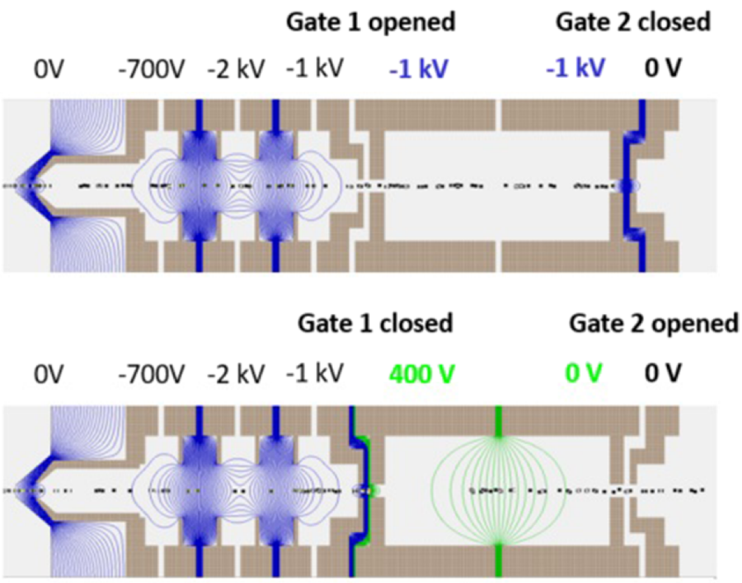

Figure 6.3: Gating process used at STARGATE. Simulated with SIMION (taken from [Bej+21]).

The ions then travel a distance of 1.5 m before a time-of-flight measurement is done. A mass resolving power of up to $R = 140$ ([Bej+21]) could be reached and it was shown that the change in mass of $^{14}N^{15}N^{16}O^+$ to $^{14}N_2\,^{16}O^+$ could be resolved (see [Bej+21]). After the drift tube a pulsed 2D deflector is used to select the ions that are led into the laser interaction zone (see (5) in fig. 6.1). The 2D deflector consists of two parallel steering plates to which a voltage is applied (typically $\simeq 1\ \mu$s with 70 V, horizontally). A fast HV push-pull switch with a rise time of 20 ns is used. A second pair of plates is used for vertical alignment. While selected ions will be guided into the laser interaction zone, not selected ions will collide with the chamber walls.

For best resolution in ion selection, the ions can be bunched at the end of the time-of-flight section. For the measurement in this thesis, however, the ions were bunched to maximise the overlap with the pulsed laser. Everything but N_2O^+ was filtered.

6.2 Laser

For photodissociation of N_2O^+ a pulsed dye laser (Continuum ND 6000, range: 614 nm to 654 nm) was used with a frequency of 30 Hz, an energy of 0.6 mJ/pulse and a pulse duration of 5 ns. This laser was pumped by a Nd:YAG laser (Continuum Powerlite Precision II) and led through a frequency doubling BBO crystal. A prism was used to separate the frequency doubled laser (range: 307 nm to 327 nm) and use it in the photodissociation (see fig. 6.4). After the UV-laser passed the laser interaction zone, it is detected on a pyroelectric detector (model PE10BB, OPHIR).

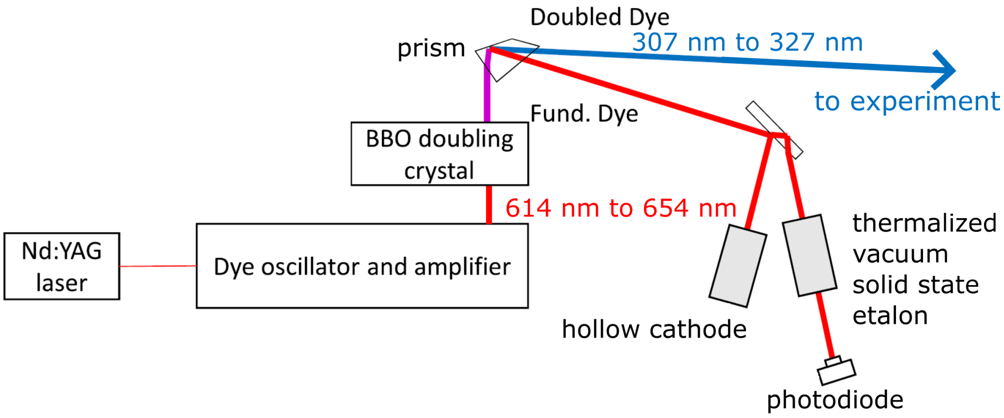

Figure 6.4: Laser setup used at STARGATE (taken from [Bej+21]).

6.3 Fragment selection and detection

While the deflector filters everything but N_2O^+, different fragments are produced due to photodissociation in the laser interaction zone. We want to detect only NO^+ to compare the detected to the simulated spectrum (see fig. 5.3). A 90° electrostatic deflector (see (8) in fig.: 6.1) is used to filter the fragments and not photodissociated ions depending on their kinetic energy. A bias cell in the laser interaction zone is used to increase the kinetic energy spread between different fragments. The selected fragment hits an MCP afterwards and is detected.

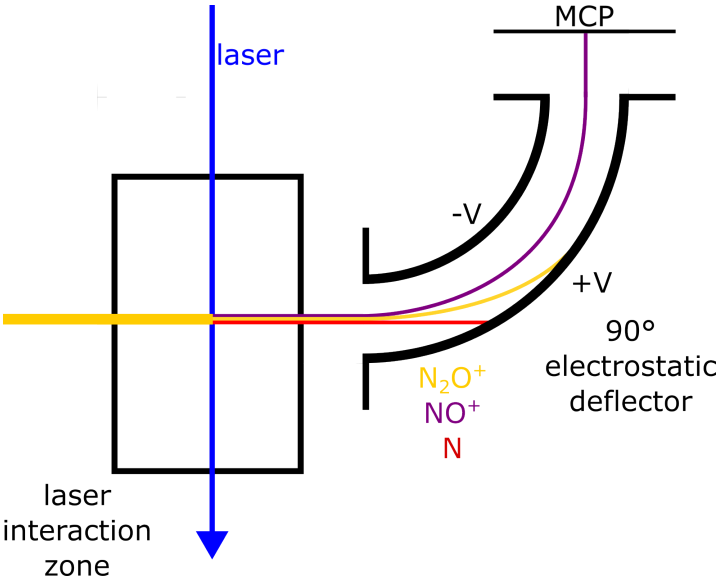

Figure 6.5: 90° electrostatic deflector used at STARGATE for fragment selection (cf. [Bej+21]).

6.4 Overlap of ion beam with pulsed laser beam

To get a maximized signal, the overlap between the ion beam and the laser beam has to be as big as possible. Bunching is used for a higher density of ions to interact with the laser pulse. The laser pulse is synchronized with a time delay to the gas injection. In [Bej+21] it is estimated that an ion bunch of 6.9 mm length interacts in an approx. 6 mm interaction region.

6.5 Vacuum

The vacuum quality is ensured by three turbo pumps (Pfeiffer ATH 2300M, Balzer 4306 and Pfeiffer Hipace 700 Plus ([Bej+21])). The ion source can be operated with up to 5 bar to 10^{-5} mbar respectively. With differential pumping between the skimmer and a pumping tube before the laser interaction zone ((2) and (6) on fig. 6.1), a pressure of 10^{-7} mbar was reached in the interaction zone of the laser, in the fragment selection and at the detector ((7), (8) and (9) on fig. 6.1). Collisions with residual gas that could heat up the molecules are suppressed and losses due to recombination are minimized.

6.6 Seeded expansion

Atoms do not have rotational and vibrational degrees of freedom to store energy in. This results in a different adiabatic index for monoatomic gases ($\gamma = 5/3 \approx 1.67$) and diatomic gases ($\gamma = 7/5 = 1.4$). Therefore, monoatomic gases cool better than diatomic gases as one can see in equation 2.31. To reach a lower temperature of N_2O^+ we used a mix of N_2O ($\gamma_{\mathrm{N_2O}} = 1.3$ [Natb]) and Ar ($\gamma_{\mathrm{Ar}} = 1.7$ [Nata]). The idealized continuum model of gas flow works well for this and for the molecular weight and heat capacity one can take the weighted average of the corresponding properties of the gases in the mix (see [Mor96]). Using a high concentration (≥ 90 %) of the carrier gas (in this case argon) the final Mach number and temperature are mostly determined by the carrier gas. The carrier gas acts as a cold bath for the molecules and due to collisions the measured ions cool down to lower temperatures. For efficient cooling, the carrier gas must have a mass similar to that of the molecule under investigation (see [Bej21]). High concentration of the carrier gas can also suppress the formation of clusters (see [Gau88]).

Chapter 7

Measured data and analysis

7.1 Mix 93 % argon and 7% N_2O

The source was shipped to Belgium and installed into the setup of STARGATE. A mix of 93 % argon and 7 % N_2O at 2 bar expanded into a vacuum at $1.25 * 10^{-5}$ mbar. The valve was operated with an opening time of 28 μs and a discharge voltage of -1000 V. The pulsed dye laser was operated at 30 Hz and with 0.6 $\frac{\text{mJ}}{\text{pulse}}$ and a pulse duration of 5 ns. The laser intensity was measured as a function of wavelength and can be seen in fig. 7.1.

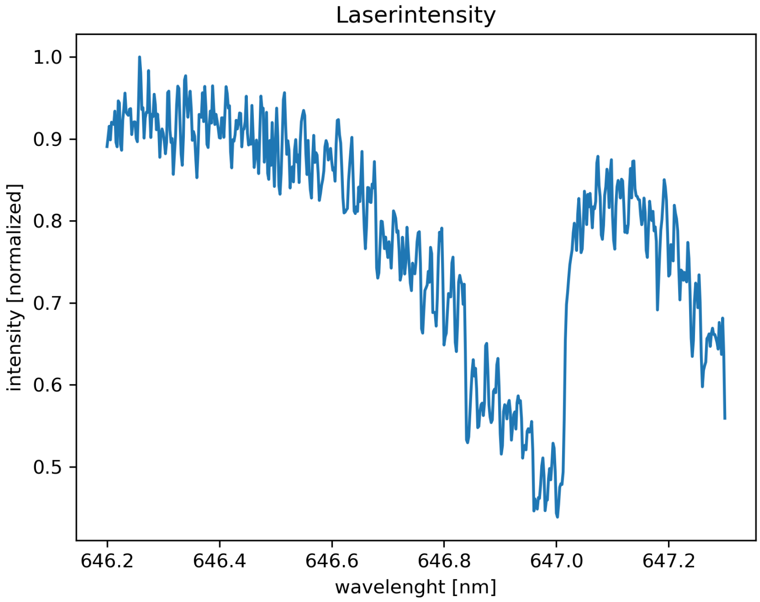

Figure 7.1: The laser intensity of the pulsed dye laser for the measurement with 93 % argon and 7 % N_2O.

The laser intensity varies over the duration of the measurement. Therefore, the recorded spectrum of NO^+ is corrected by the laser intensity.

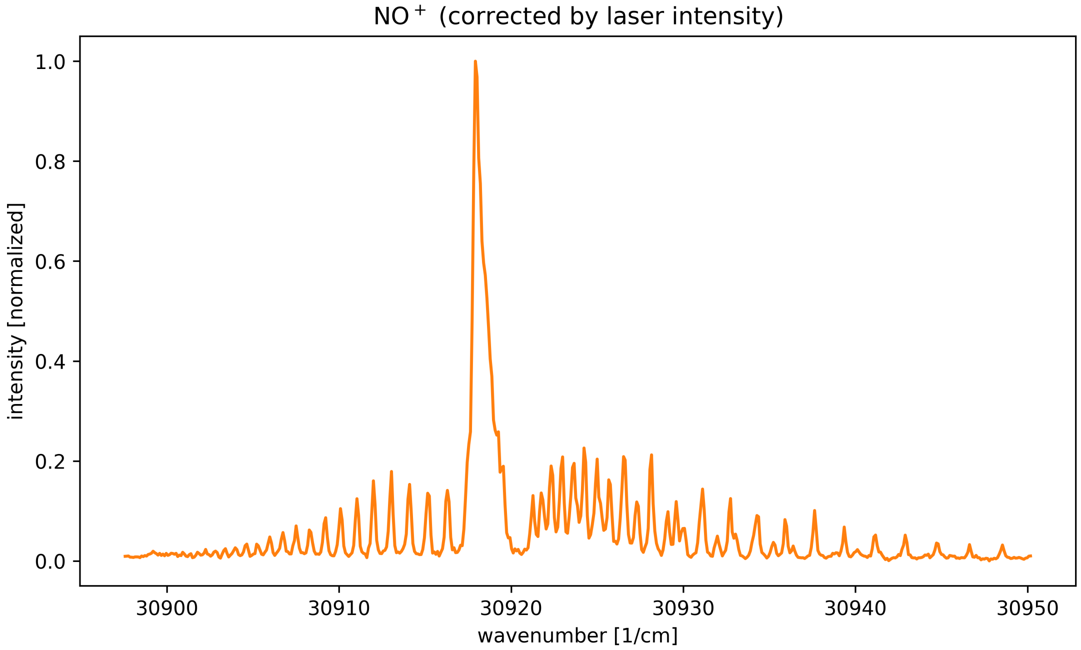

Figure 7.2: The detected NO^+ signal corrected by the laser intensity.

The wavelength scale was calibrated to the Q-branch and the experimental data is shifted by 9.35 cm^{-1} to the simulated spectra. This could be due to inaccuracy in the readout of the wavenumber. The wavenumber shown in fig. 7.2 is calculated from the measured wavelength of the dye laser before frequency doubling.

Fitting one simulated spectrum for different temperatures on the measured data does not give good results. The reason for this can be seen when one compares the measured data to the simulated spectra (see fig. 7.3). The measured spectra shows visible markers for hot and cold ions. For example, the valley at approx. 30912 cm^{-1} is only visible for cold molecules and also visible in the measured spectra. At approx. 30890 cm^{-1} there is a small peak visible in the measured spectra, that is very dominant in the simulated spectrum for warm ions and not visible for cold ions. Overall, the structure of the branches looks like there are more cold ions than hot ions.
The population of states for a given temperature can be calculated with the Maxwell-Boltzmann distribution. The Maxwell-Boltzmann distribution assumes a thermodynamic equilibrium. In the supersonic expansion the gas cools by collisions. At high densities there are enough collisions to maintain thermal equilibrium. But because molecules have a finite size and the gas is not an ideal continuum, the number of collisions decreases when the density decreases in the expansion. The efficiency of the cooling is determined by the efficiency of energy transfer in the degrees of freedom

and is given in the order of translational > rotational > vibrational [IMV03] (see also chapter 4). This could be one reason why the recorded spectrum does not match the simulated spectrum for one temperature. Secondly, the ions are gated, focused and accelerated before photodissociation. This could lead to a heating of some ions.

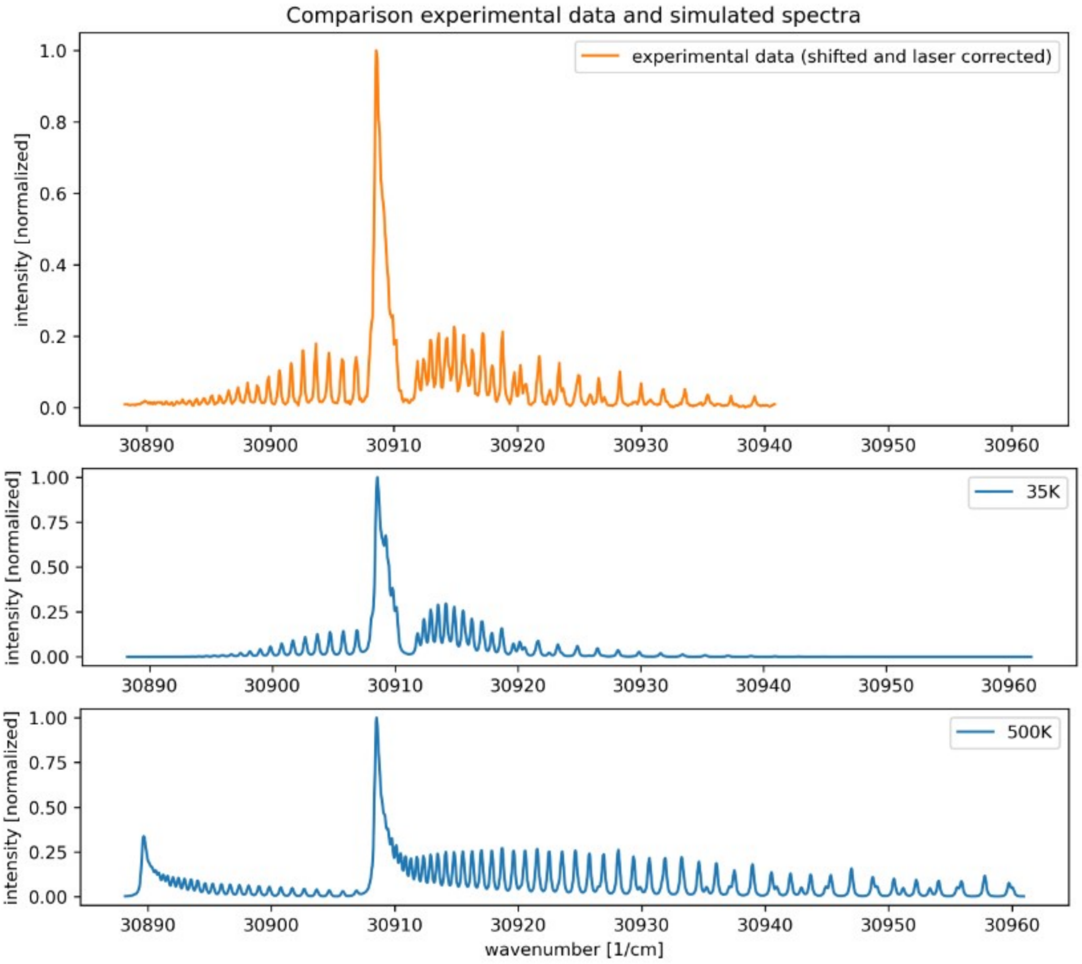

Figure 7.3: Measured data shifted and corrected with laser intensity in comparison to simulated spectra.

A simple model was used to derive temperature of the ions from the data. The weighted sum of two simulated spectra was fitted on the measured data.

$$f_{fit}(c) = c * S(T_1) + (1 - c) * S(T_2), \tag{7.1}$$

where $S(T_1)$ is a simulated spectrum for the temperature T_1 and $S(T_2)$ is a simulated spectrum for the temperature T_2. c is the only fit parameter and can have values between 0 and 1 and describes the weight of spectrum $S(T_1)$ to spectrum $S(T_2)$. The following combinations of spectra were fitted to the data. All fits are shown in the appendix A.1.

Combination of fitted spectra				
$S(T_1)/S(T_2)$	$S(70\text{ K})$	$S(100\text{ K})$	$S(200\text{ K})$	$S(500\text{ K})$
$S(10\text{ K})$	A.1	A.2	A.3	A.4
$S(20\text{ K})$	A.5	A.6	A.7	A.8
$S(25\text{ K})$	A.9	A.10	A.11	A.12
$S(30\text{ K})$	A.13	A.14	A.15	A.16
$S(35\text{ K})$	A.17	A.18	A.19	A.20
$S(40\text{ K})$	A.21	A.22	A.23	A.24
$S(70\text{ K})$	A.25	A.26	A.27	A.28

Table 7.1: The combinations of $S(T_1)$ and $S(T_2)$ fitted with eq. 7.1. The table consists of references to the plots that are shown in the appendix A.1.

The fit of $S(40\text{ K})$ and $S(200\text{ K})$ matches the measured data best.

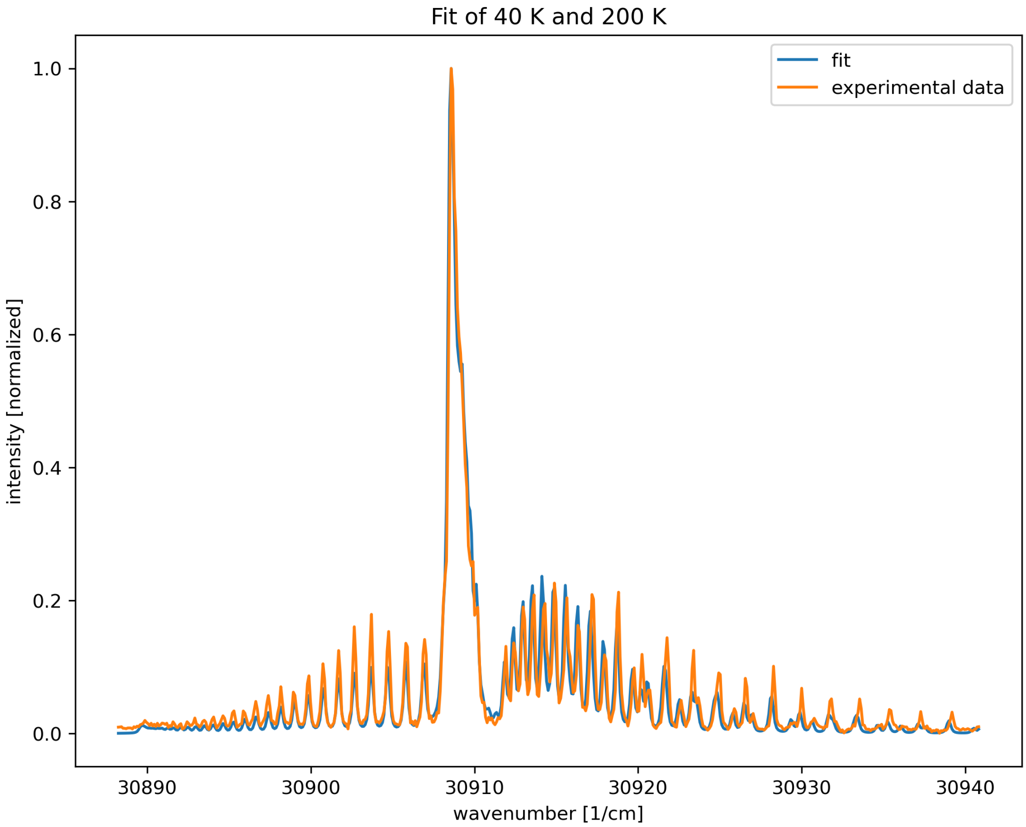

Figure 7.4: Fit of spectra for 40 K and 200 K. The fit parameter results $c = 0.800 \pm 0.027$.

The fit parameter c results in $c = 0.800 \pm 0.027$. In the used fit model this means that approx. 80 % of the ions are at 40 K and approx. 20 % are at 200 K.

The model of two weighted simulated spectra fitted on the data reproduces the measured data well. Although indicators for warm ions are visible, they are not dominant. For example, the peak at 30890 cm^{-1} is very dominant in the simulated spectrum for warm ions (see fig. 7.3) and small in the measured data. Indicators for cold ions are dominant (e.g. the valley at approx. 30912 cm^{-1} is only visible for low temperatures). The fit parameter $c = 0.800 \pm 0.027$ shows, that the temperature of most of the ions is closer to 40 K than to 200 K.

7.2 Effect of carrier gas

Argon is used as a carrier gas to cool N_2O to lower temperatures. Argon has a different adiabatic index than N_2O ($\gamma_{Ar} = 5/3 \approx 1.67$ and $\gamma_{N_2O} = 7/5 = 1.4$ (see section 6.6)) and also suppresses the formation of clusters (see section 4.8). To measure this effect a spectrum with pure N_2O was recorded. The valve was operated with an opening time of 34 μs and a discharge voltage of -973 V. Pure N_2O at 5 bar expanded into a vacuum at $1.00 * 10^{-5}$ mbar. The recorded spectrum (see fig. 7.5) was shifted by 10.19 cm^{-1} and corrected by the measured laser intensity (see fig. A.29).

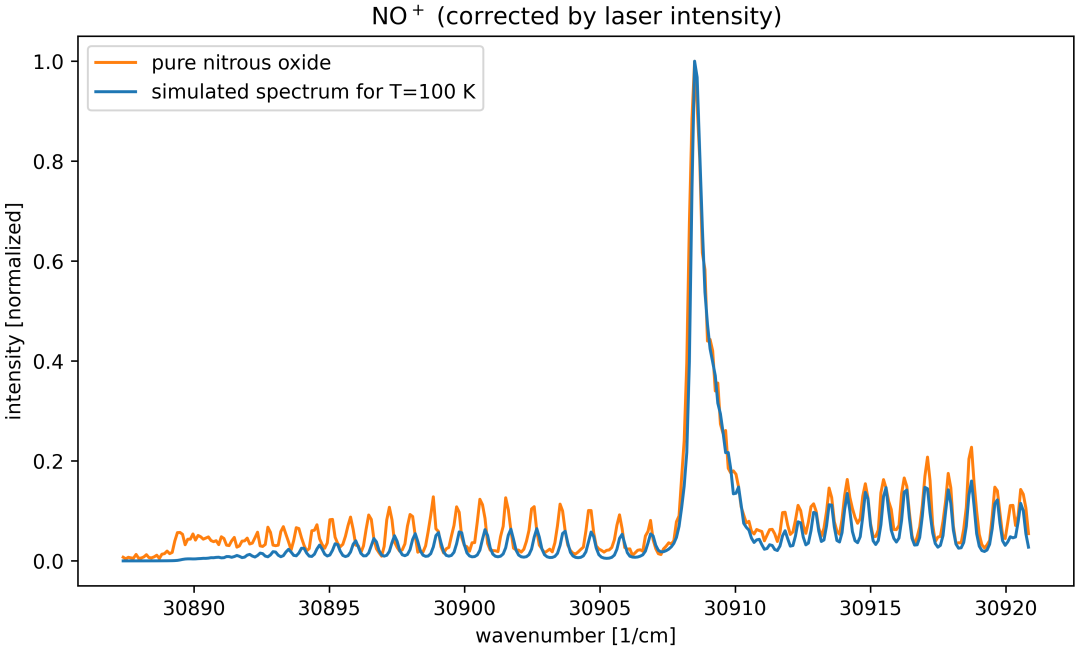

Figure 7.5: Comparison between the simulated spectrum at $T = 100$ K and the measured data shifted by 10.19 cm^{-1}.

However, one can see that the position of the peaks in the recorded data and the simulated spectrum match in the R-branch, but not in the P-branch. This was not visible in the spectrum for 93 % argon to 7 % N_2O. To fit the simulated spectrum, the recorded data of pure N_2O was scaled so the position of the peaks match. The two recorded spectra for 93 % argon to 7 % N_2O and pure N_2O can be seen in fig. 7.6.

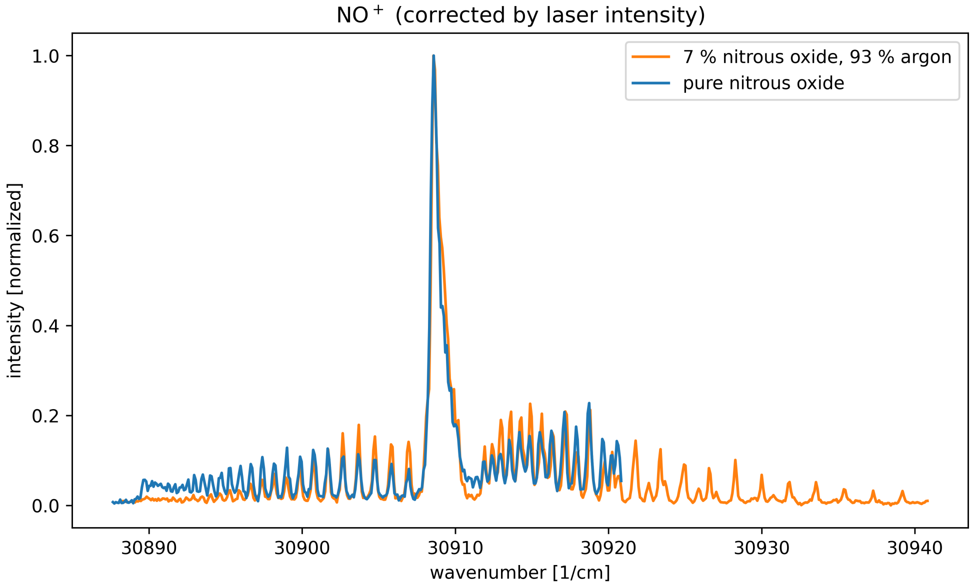

Figure 7.6: Comparison between the measured spectrum for 93 % argon to 7 % N_2O and pure N_2O.

In the spectrum for pure N_2O a pressure of 5 bar was used, resulting in a higher pressure ratio $\frac{p_t}{p}$ which should lead to higher Mach numbers and therefore lower temperatures (see eq. 2.32 and eq. 2.31). However, the indicators for warm ions are more dominant in the spectrum of pure N_2O. The simulated spectra were fitted on the measured spectrum for pure N_2O the same way it was done with the spectrum for 93 % argon to 7 % N_2O. All fits are shown in the appendix A.2.

The fit for $S(70\text{ K})$ and $S(200\text{ K})$ matches the measured data best (see fig. 7.7). The fit parameter $c = 0.201 \pm 0.058$ shows, that the temperature of most of the ions is closer to 200 K than to 70 K. N_2O cools down to significantly lower temperatures when argon is used as a carrier gas in high concentrations. The reason for this is the different adiabatic index of N_2O and argon. Also, the production of clusters is enhanced for higher pressures (see section 4.8) and in this measurement not suppressed by argon. This could also effect the cooling of the gas.

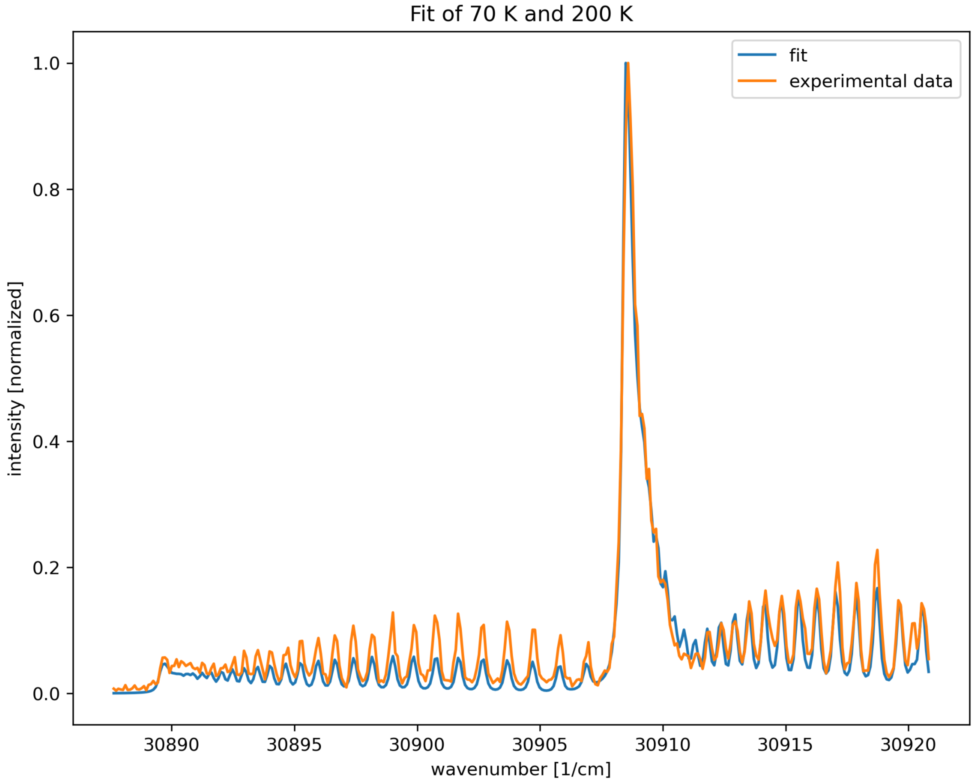

Figure 7.7: Fit of spectra for 70 K and 200 K. The fit parameter results $c = 0.201 \pm 0.058$.

Chapter 8

Discussion and outlook

8.1 Discussion

In the framework of this thesis the simple supersonic expansion source, developed at the Max Planck Institute for Nuclear Physics, was shipped to Belgium into the lab of Prof. Dr. Xavier Urbain and characterized with resonant photodissociation of the nitrous oxide cation. The source has a simple and stable design based on the commercial available Amsterdam Piezo Valve and a discharge between two electrodes. One electrode is on ground potential and a static high voltage is applied on the other electrode. Thanks to a circuit that limits the current, commercial available power supplies can be used to drive the discharge. The valve has opening times from 20 μs to continuum and a nozzle with a diameter of $D = 2.5$ mm was used. The nozzle diameter of the simple supersonic expansion source is bigger than the nozzle diameters in other expansion ion sources (0.5 mm in [Bej+21], 0.5 mm in [McC+04], 1 mm in [PT89]) and in tests with H_3^+ the source was able to produce pulses of up to 10 μA (see section 3.1). To record the resonant photodissociation spectrum of N_2O^+ the source was installed in the setup of STARGATE. A mix of 93 % argon and 7 % N_2O at 2 bar expanded into a vacuum at $1.25 * 10^{-5}$ mbar. Everything but N_2O^+ was filtered before the molecular ions entered the laser interaction zone. A second filter was used and only NO^+, that was produced by the resonant photodissociation, was detected on a MCP (see fig. 6.1). Although the recorded spectra showed characteristics that most of the ions were cold, there were some indicators for warmer ions. This could be due to broken thermal equilibrium in the expansion process (see chapter 4) or heating of the ions when they are gated, focused or accelerated. To derive a temperature, a simple model of a weighted sum of two simulated spectra for different temperatures was fitted to the recorded spectrum. The model resulted that 80 ± 2.7 % of the ions are at 40 K and 20 ± 2.7 % of the ions are at 200 K. This is a very low temperature for an ion source, since other ion sources produce ions at an internal temperature of $T \sim 10^3$ K (e.g. a typical vibrational temperature in plasma ion sources is $T = 3000$ K [Hir+20]). The final temperature is significantly lower than the rotational temperature observed in RICE (Riken cryogenic storage ring) $T_{RICE} = 320 \pm 20$ K – even for long storage times [Hir+20]. The temperature of this ion source is comparable to the final temperature of a pulsed supersonic expansion source also used with N_2O in the setup of STARGATE (40 ± 3 K with a mix of 99 % argon and 1 % N_2O at 5 bar) [Bej+21].

We were also able to show the difference in cooling with argon as carrier gas. The simple model of a weighted sum of two simulated spectra was fitted on the spectrum of pure N_2O^+ that expanded from 5 bar into a vacuum of $1.00 * 10^{-5}$ mbar. The model resulted that 20 % of the ions have a temperature of 70 K and 80 % of the ions have a temperature of 200 K. So even though the gas expanded from a higher pressure ratio, a higher temperature was reached. N_2O^+ cools down to significantly lower temperatures when argon is used as carrier gas in high concentrations.

There are some ideas to further improve the simple supersonic expansion source. The electrodes in the nozzle are recessed and form a diameter of $D_{electrodes} = 4$ mm while the rest of the nozzle has a diameter of $D = 2.5$ mm (see fig. 4.8). This could enhance turbulence in the gas flow through the nozzle. It could be tested if not recessed electrodes have an effect on the discharge, the gas flow and the final temperature in the expansion. Furthermore, the final temperature is dependent of the initial temperature of the gas before expansion. A precooled gas or a cold nozzle could lead to lower temperatures. However, the idea was to build a simple, reliable and transportable supersonic expansion ion source. To precool the gas would require a much more complex design. The vacuum pressure could be improved, to further suppress interaction of the expanding gas with the residual gas. The recorded resonant photodissociation spectrum was shifted for the measurement of 93 % argon and 7 % N_2O as well as for pure N_2O. For pure N_2O there was even a problem with the scaling. While the location of the peaks for the R-branch matched with the simulated spectrum, the position of the peaks of the P-branch did not match (see fig. 7.5). The measurement of the wavenumber of the laser could therefore be further improved.

8.2 Outlook

To study the DR process of H_3^+ as it takes place in the interstellar medium, the molecule has to be stored at low pressure and be vibrationally and rotationally cold (see chapter 1). H_3^+ has no permanent dipole moment and rotations do not cool to their lowest rotational states in accessible storage times for cryogenic storage rings. The supersonic expansion ion source is able to produce short high density pulses of rotationally cold molecular ions. For N_2O the source produced ions that are rotationally colder than ions observed at RICE – even for long storage times [Hir+20]. Although rotations cool fast in supersonic expansions, vibrations do not. However, it has been shown that vibrations of H_3^+ cool to their lowest states in a few seconds in cryogenic storage rings (see [Kre+04] and [Kre+10]). In the future, we want to use the simple supersonic expansion source in combination with the CSR to study H_3^+ in low rotational and vibrational states. The supersonic expansion source has already been transported back from Belgium to Heidelberg and is installed into one of the two ion production platforms of the CSR.

Appendix A

Fitted spectra

Two spectra were fitted on the measured data. All fitted spectra are shown in this appendix.

A.1 93 % argon and 7 % nitrous oxide

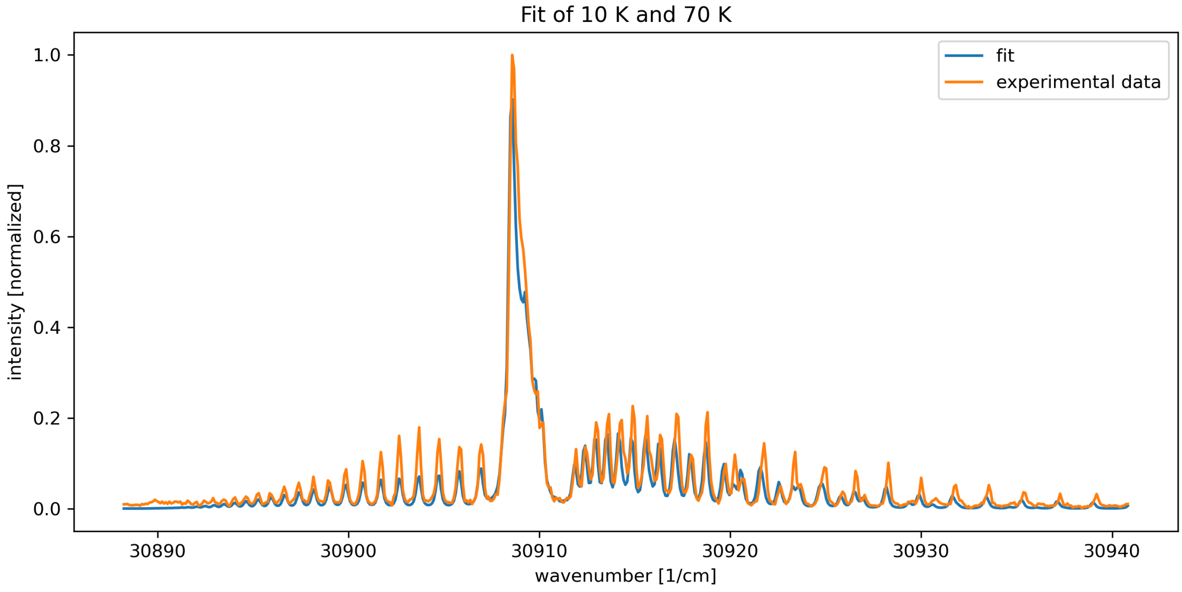

Figure A.1: Fit of spectra for 10 K and 70 K. The fit parameter results $c = 0.121 \pm 0.011$.

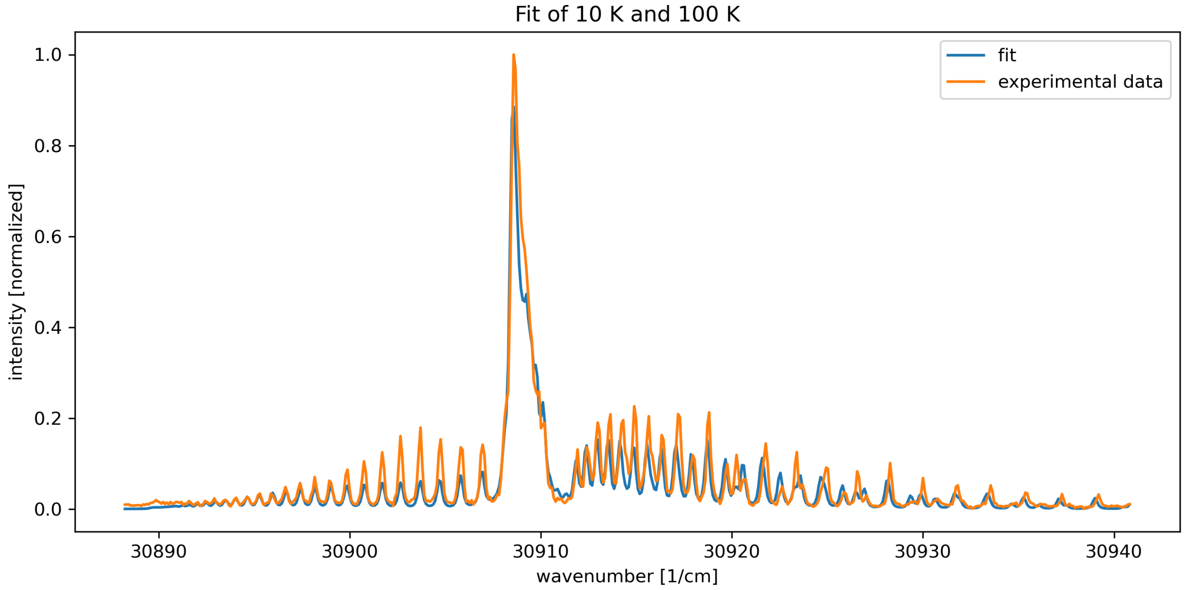

Figure A.2: Fit of spectra for 10 K and 100 K. The fit parameter results $c = 0.143 \pm 0.011$.

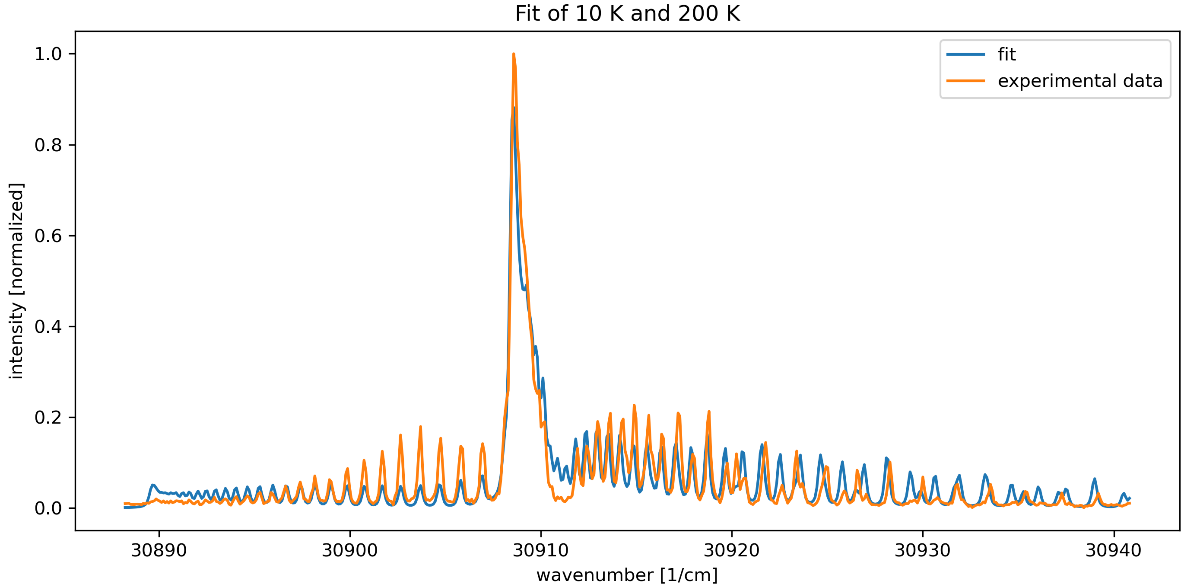

Figure A.3: Fit of spectra for 10 K and 200 K. The fit parameter results $c = 0.147 \pm 0.013$.

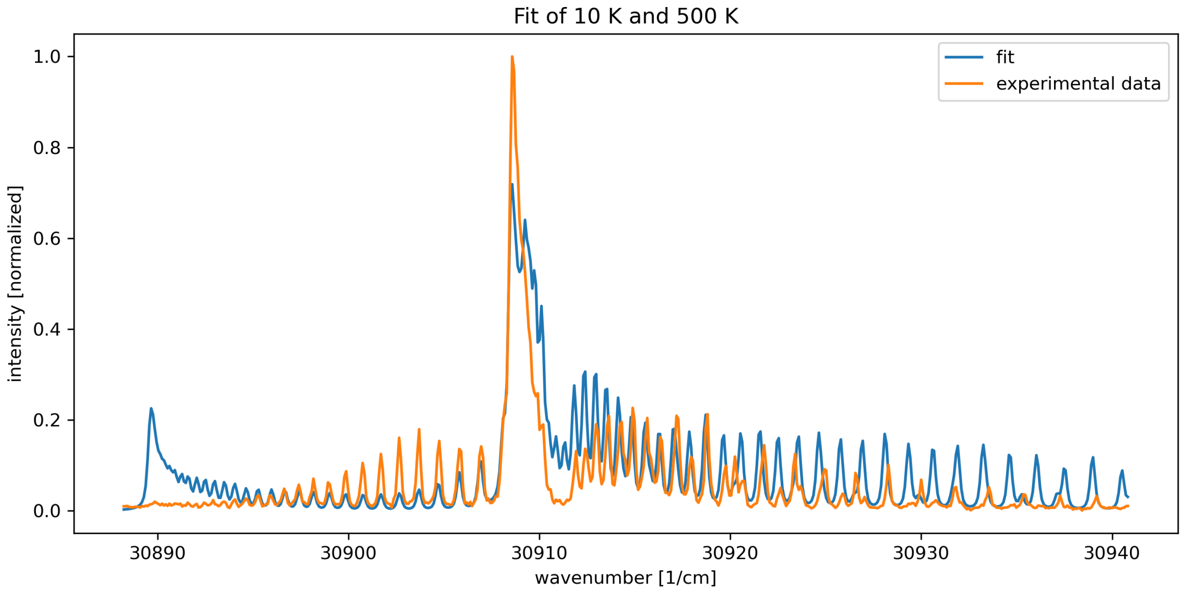

Figure A.4: Fit of spectra for 10 K and 500 K. The fit parameter results $c = 0.350 \pm 0.021$.

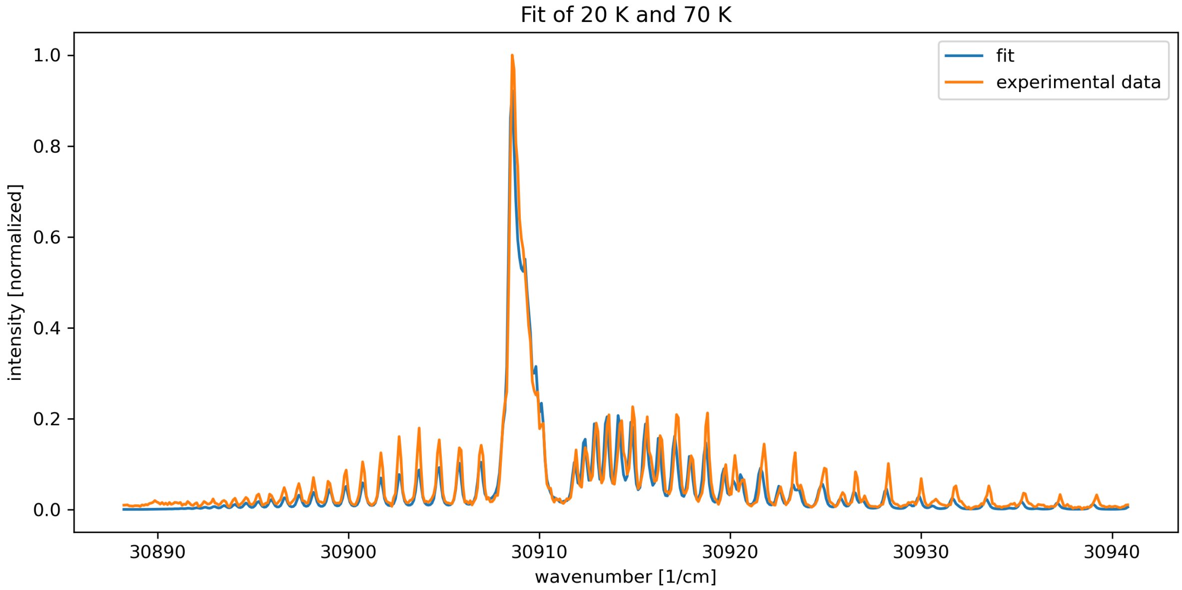

Figure A.5: Fit of spectra for 20 K and 70 K. The fit parameter results $c = 0.244 \pm 0.013$.

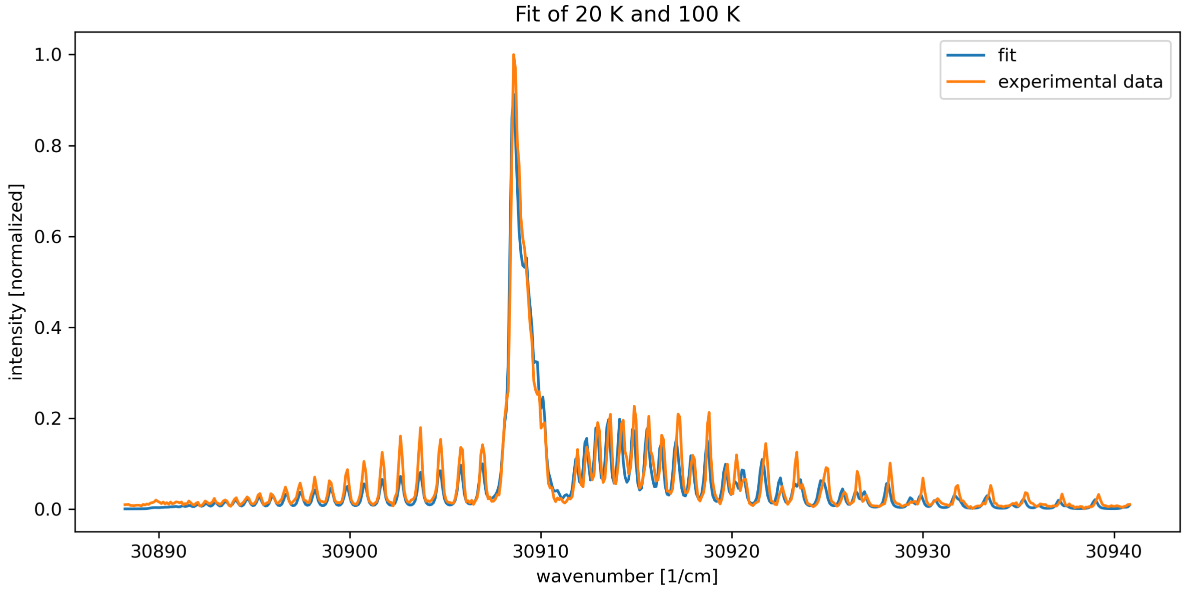

Figure A.6: Fit of spectra for 20 K and 100 K. The fit parameter results $c = 0.273 \pm 0.013$.

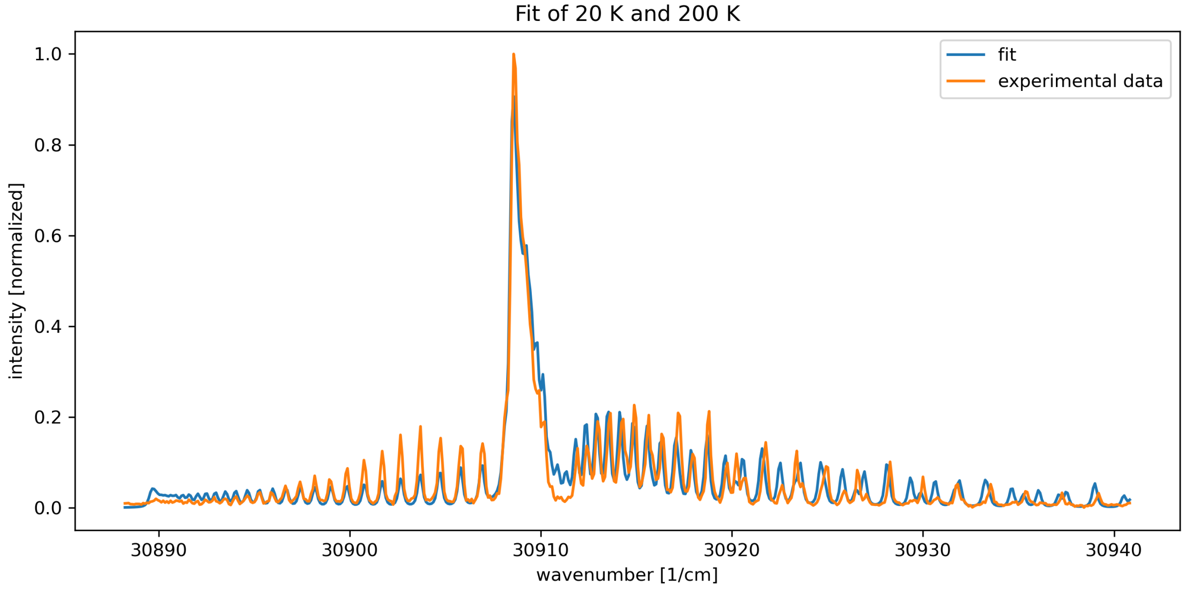

Figure A.7: Fit of spectra for 20 K and 200 K. The fit parameter results $c = 0.292 \pm 0.015$.

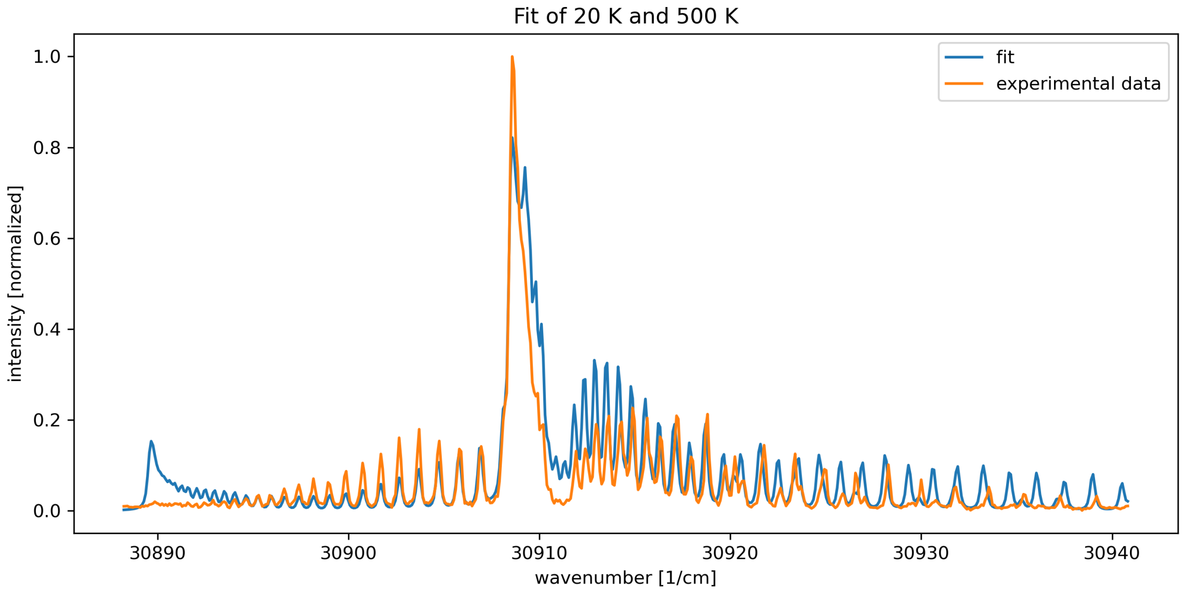

Figure A.8: Fit of spectra for 20 K and 500 K. The fit parameter results $c = 0.559 \pm 0.021$.

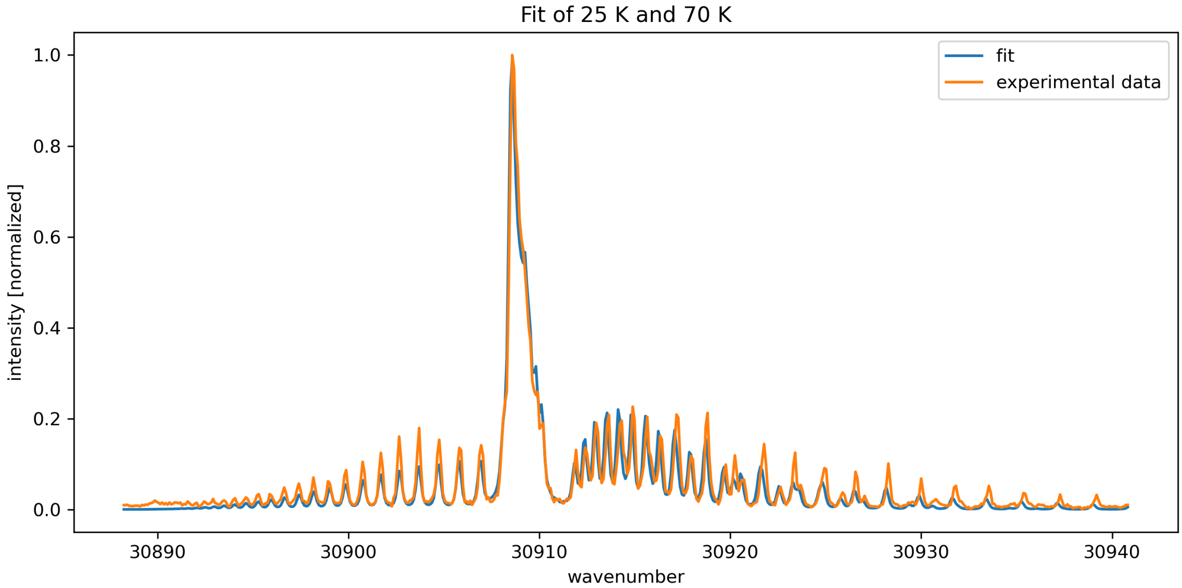

Figure A.9: Fit of spectra for 25 K and 70 K. The fit parameter results $c = 0.270 \pm 0.013$.

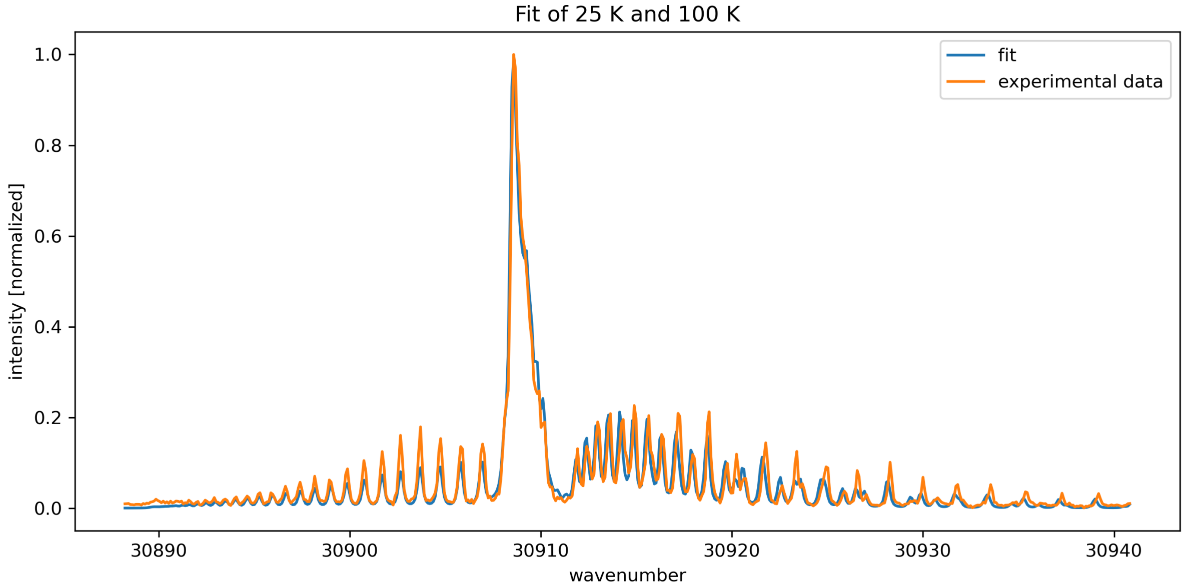

Figure A.10: Fit of spectra for 25 K and 100 K. The fit parameter results $c = 0.297 \pm 0.013$.

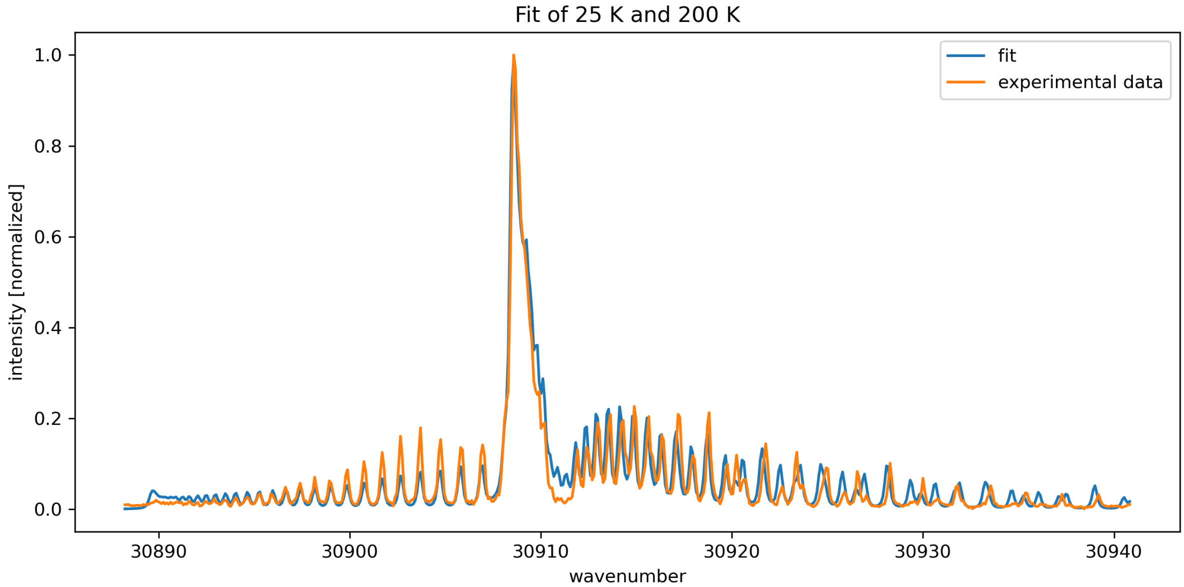

Figure A.11: Fit of spectra for 25 K and 200 K. The fit parameter results $c = 0.318 \pm 0.015$.

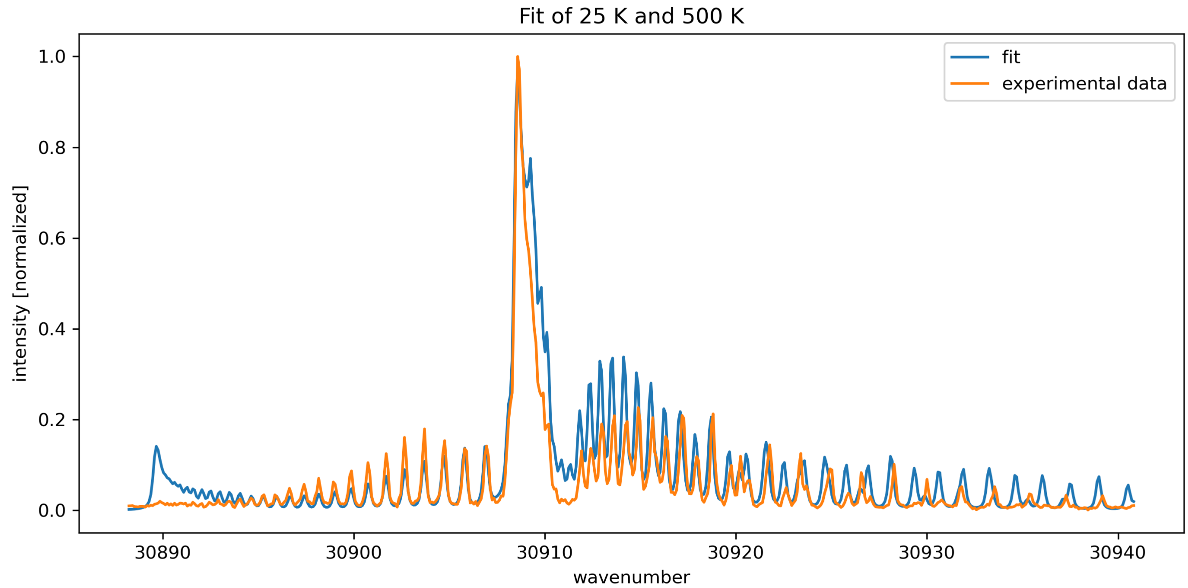

Figure A.12: Fit of spectra for 25 K and 500 K. The fit parameter results $c = 0.594 \pm 0.021$.

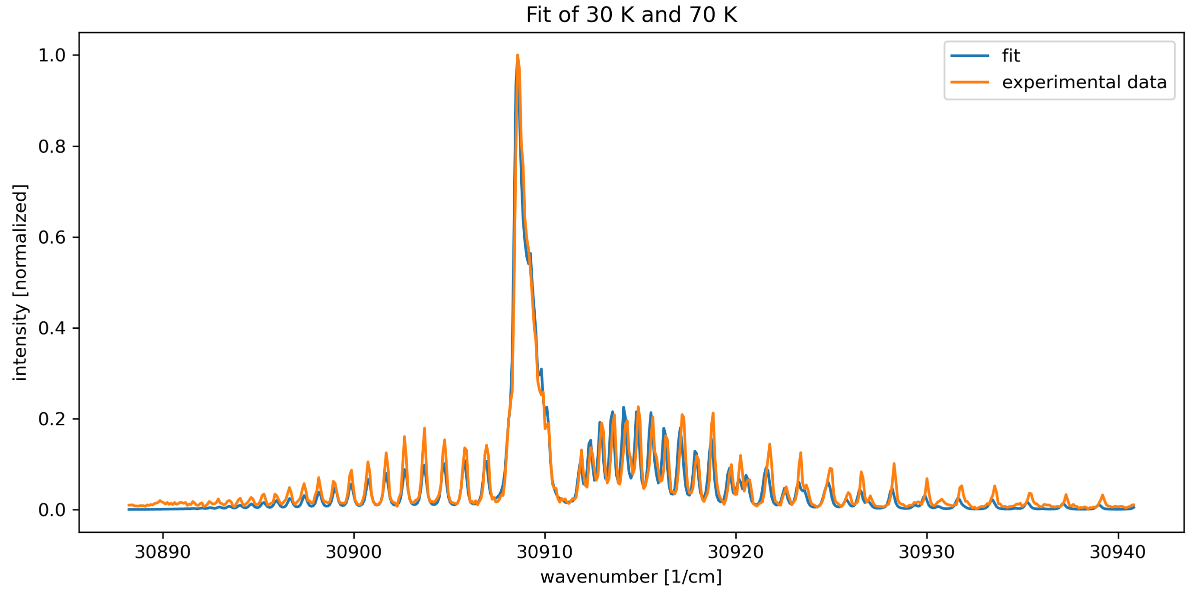

Figure A.13: Fit of spectra for 30 K and 70 K. The fit parameter results $c = 0.388 \pm 0.019$.

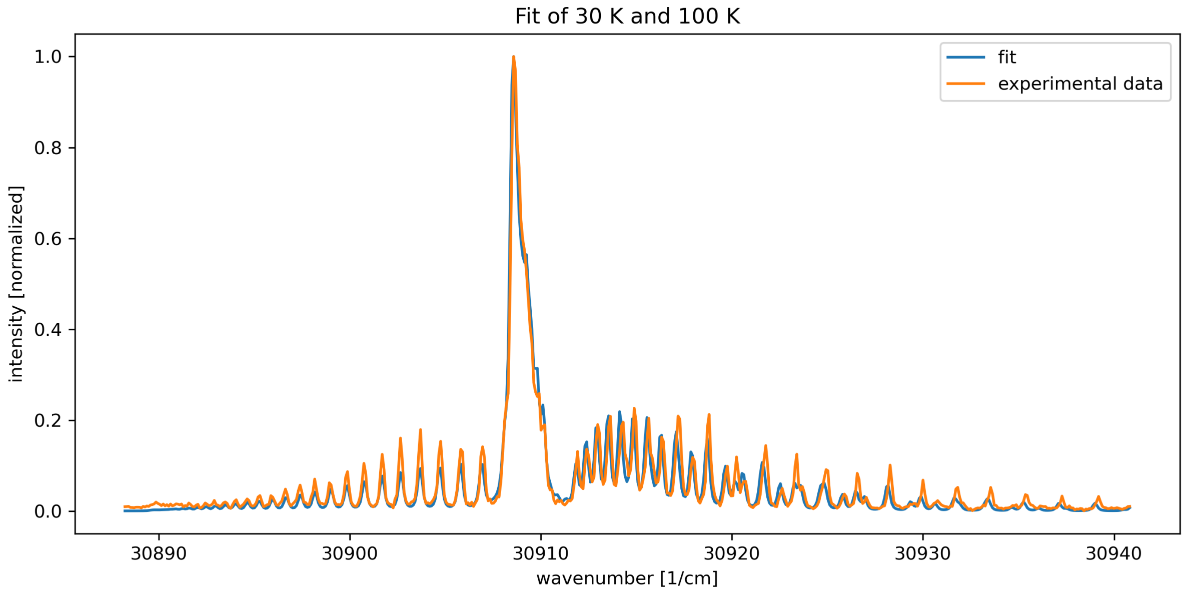

Figure A.14: Fit of spectra for 30 K and 100 K. The fit parameter results $c = 0.419 \pm 0.017$.

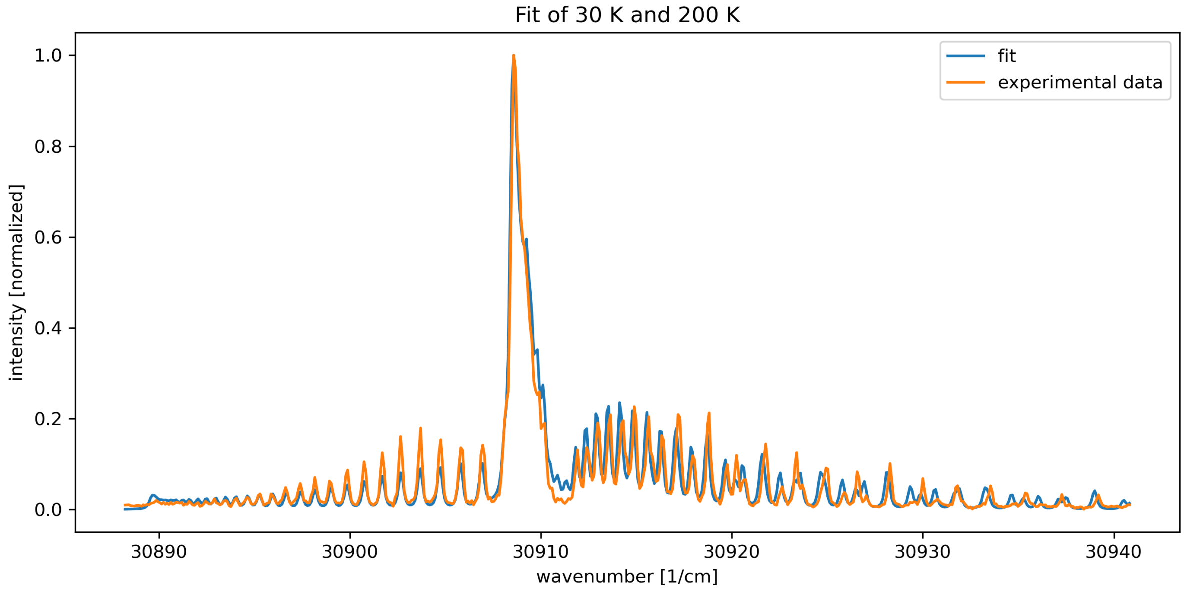

Figure A.15: Fit of spectra for 30 K and 200 K. The fit parameter results $c = 0.469 \pm 0.019$.

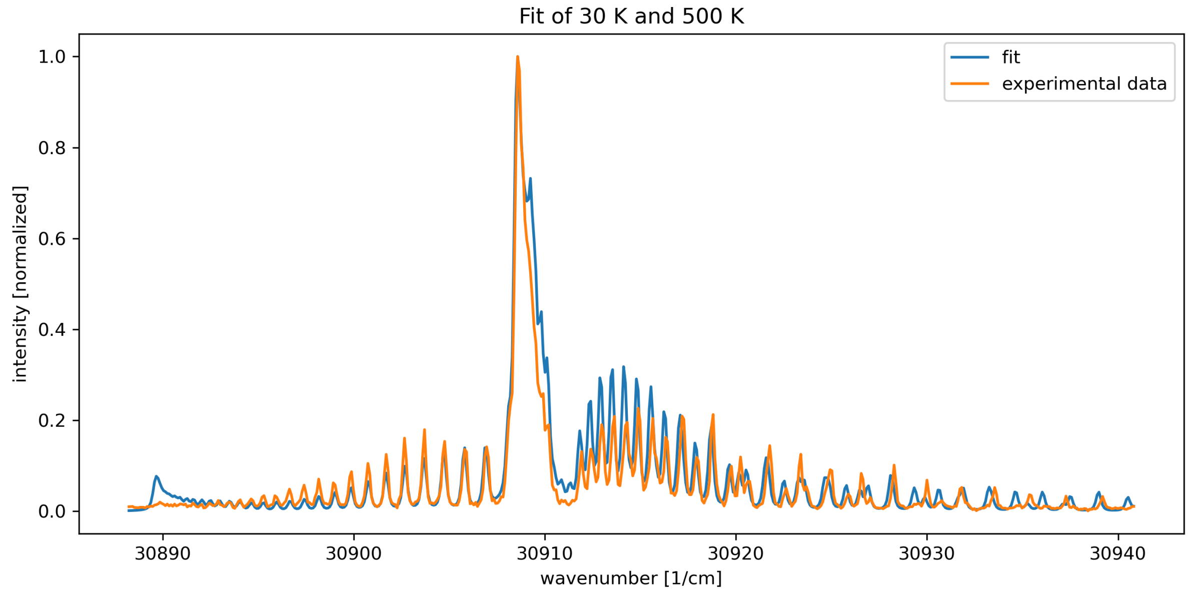

Figure A.16: Fit of spectra for 30 K and 500 K. The fit parameter results $c = 0.779 \pm 0.019$.

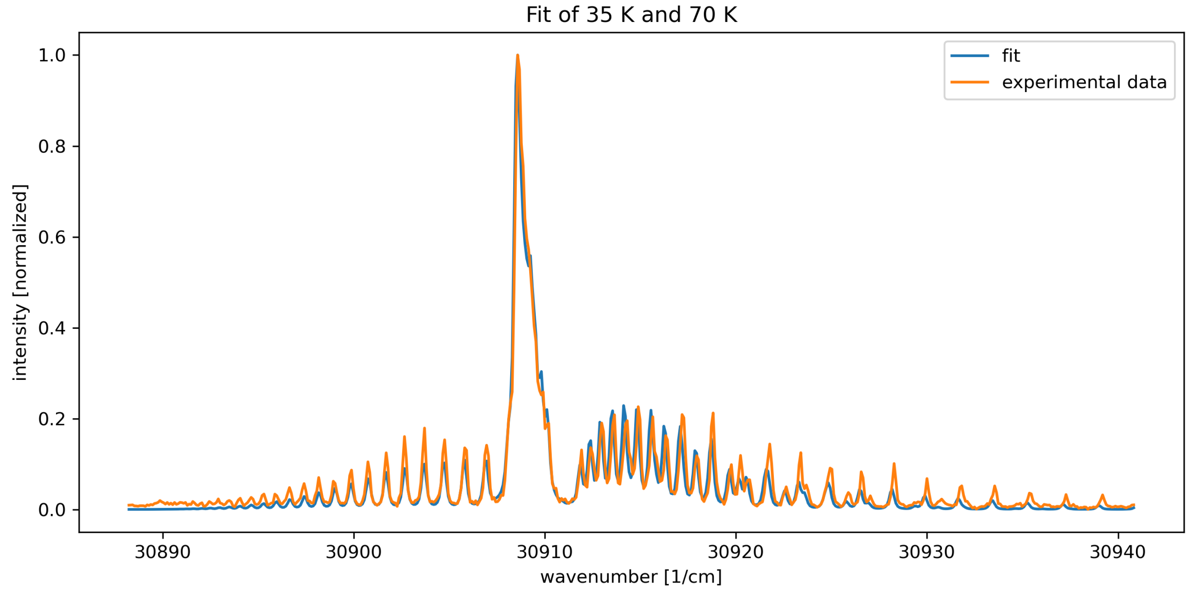

Figure A.17: Fit of spectra for 35 K and 70 K. The fit parameter results $c = 0.569 \pm 0.028$.

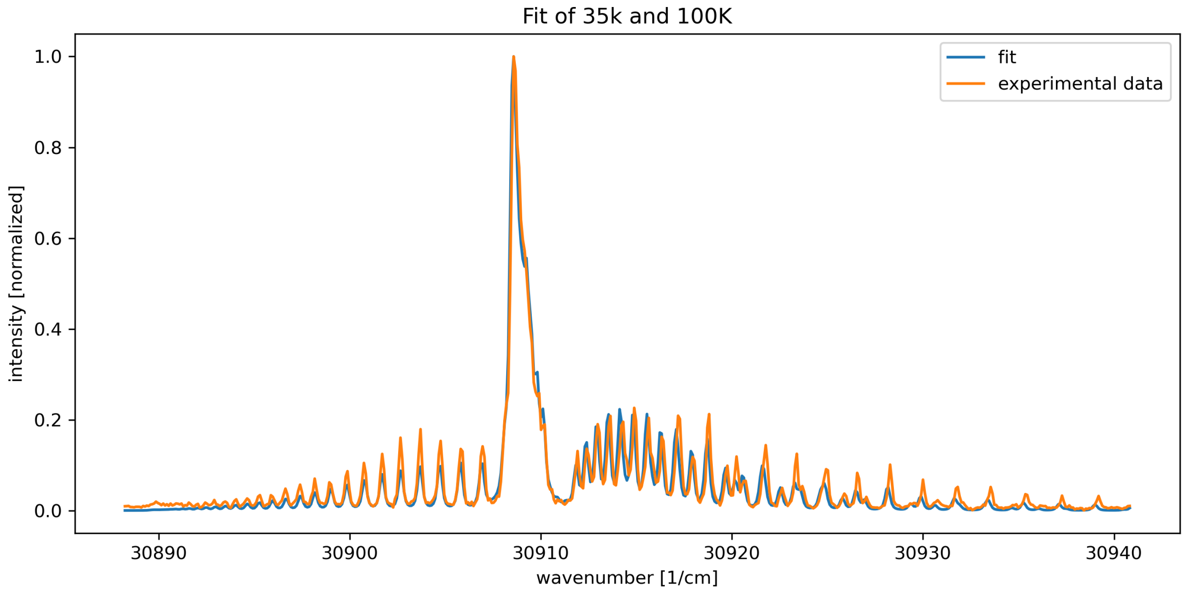

Figure A.18: Fit of spectra for 35 K and 100 K. The fit parameter results $c = 0.592 \pm 0.025$.

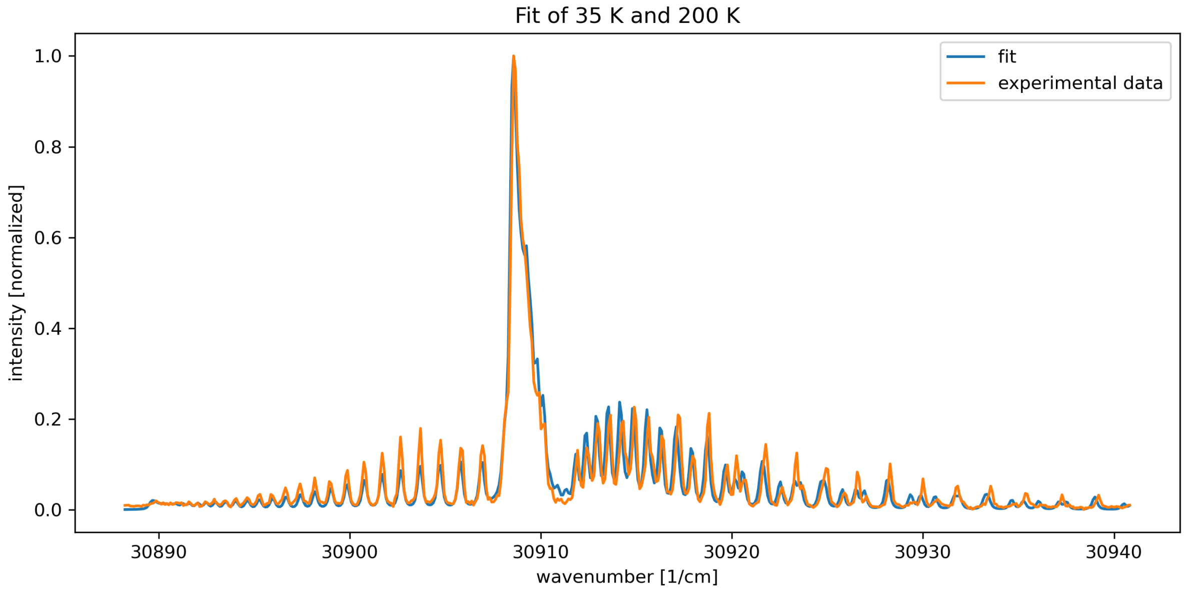

Figure A.19: Fit of spectra for 35 K and 200 K. The fit parameter results $c = 0.658 \pm 0.023$.

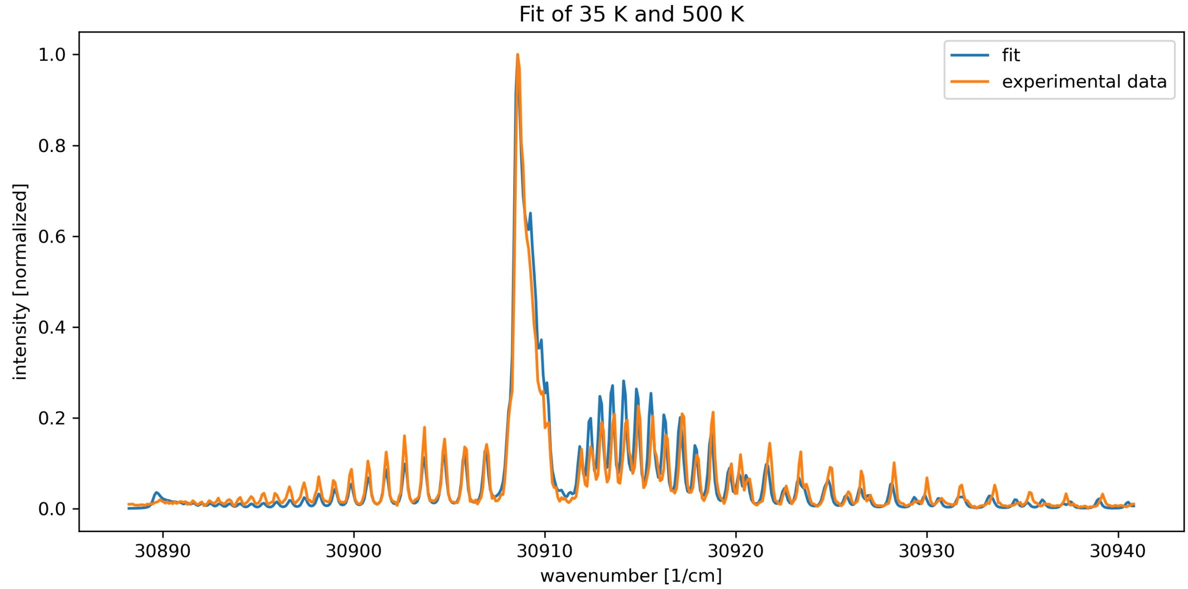

Figure A.20: Fit of spectra for 35 K and 500 K. The fit parameter results $c = 0.898 \pm 0.016$.

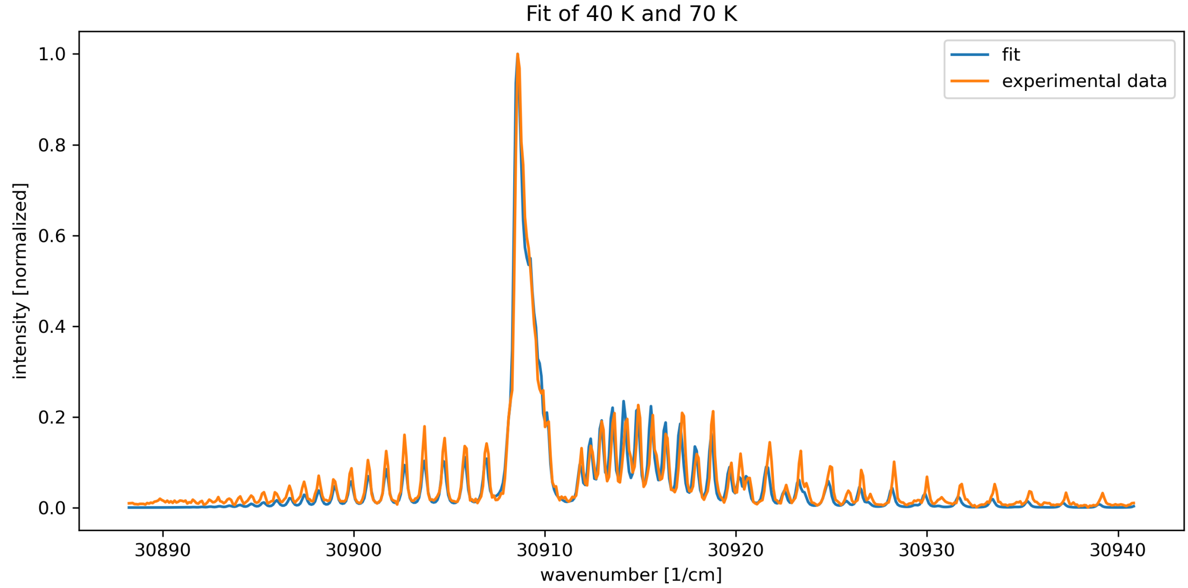

Figure A.21: Fit of spectra for 40 K and 70 K. The fit parameter results $c = 0.766 \pm 0.037$.

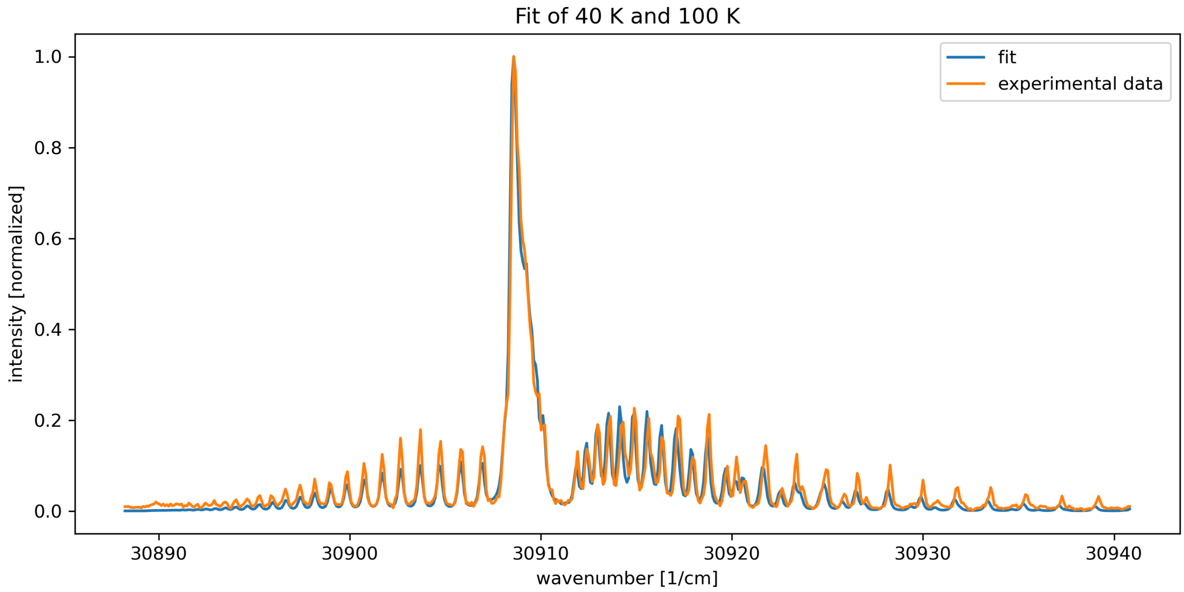

Figure A.22: Fit of spectra for 40 K and 100 K. The fit parameter results $c = 0.764 \pm 0.032$.

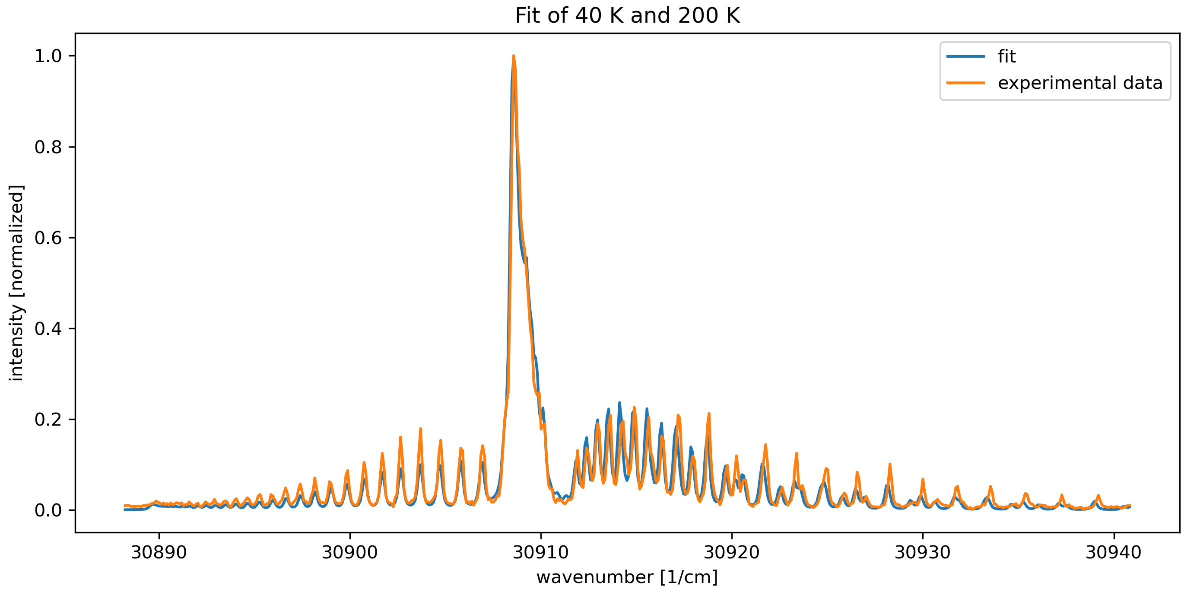

Figure A.23: Fit of spectra for 40 K and 200 K. The fit parameter results $c = 0.800 \pm 0.027$.

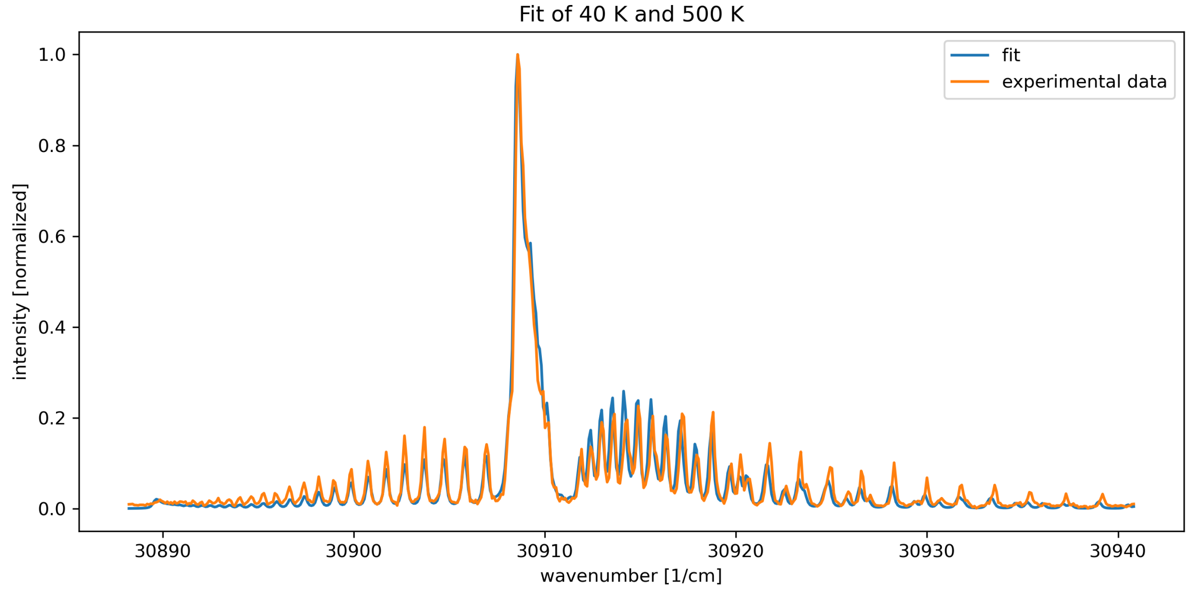

Figure A.24: Fit of spectra for 40 K and 500 K. The fit parameter results $c = 0.941 \pm 0.014$.

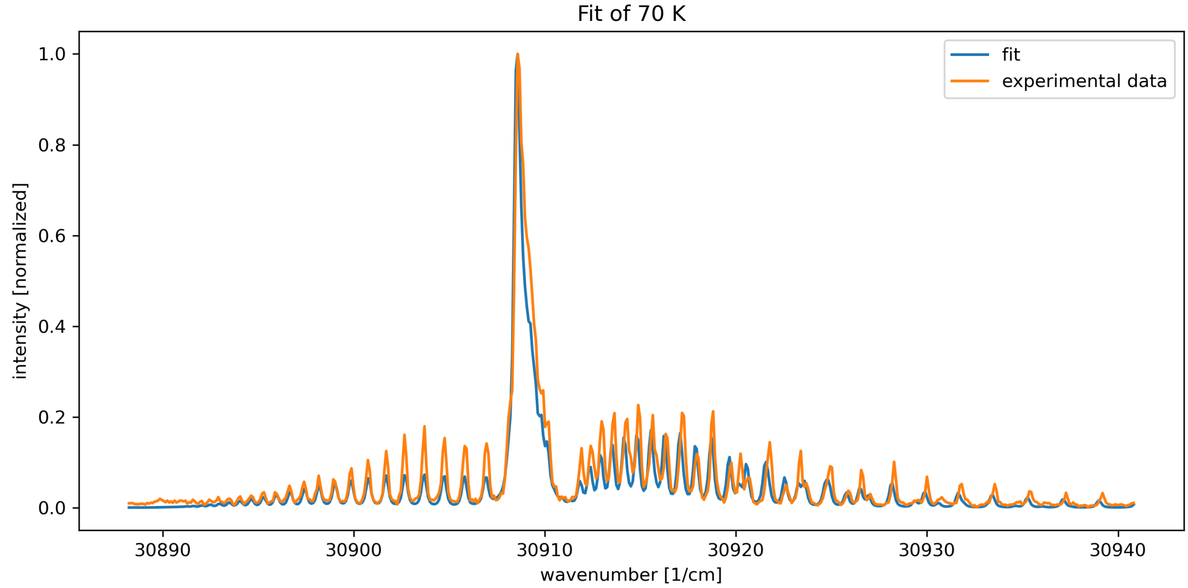

Figure A.25: Spectrum for 70 K.

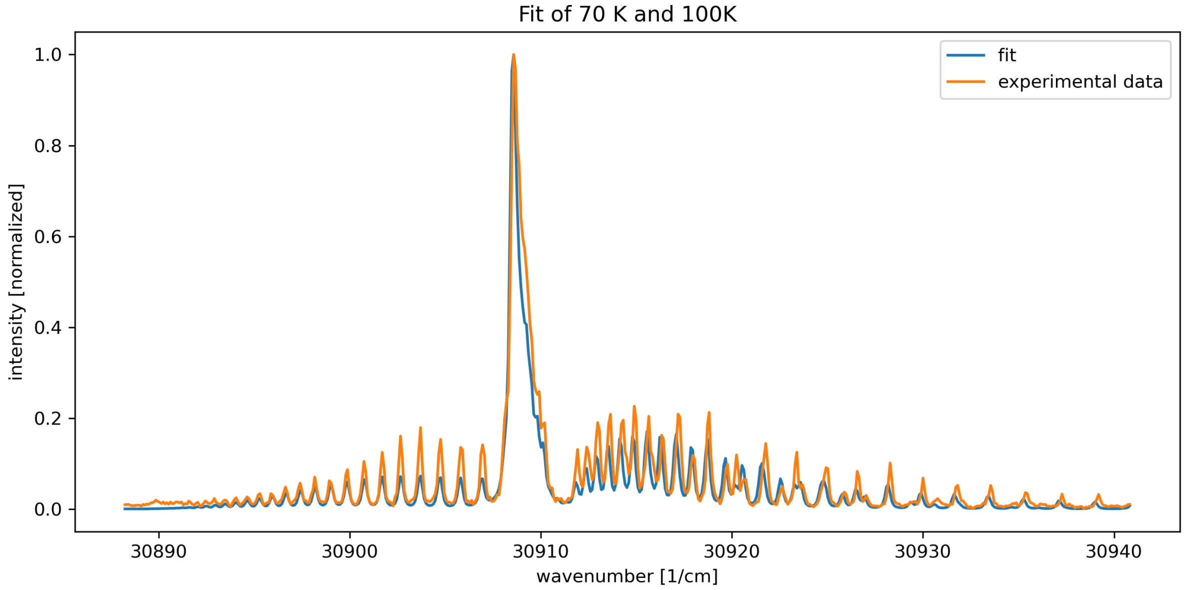

Figure A.26: Fit of spectra for 70 K and 100 K. The fit parameter results $c = 1.00 \pm 0.167$.

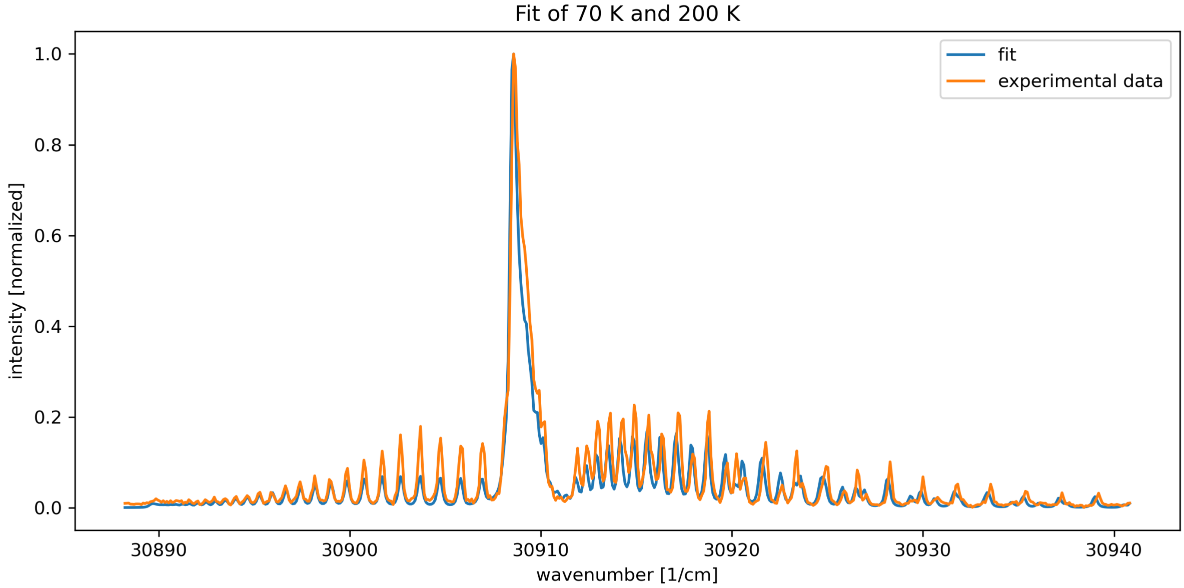

Figure A.27: Fit of spectra for 70 K and 200 K. The fit parameter results $c = 0.859 \pm 0.054$.

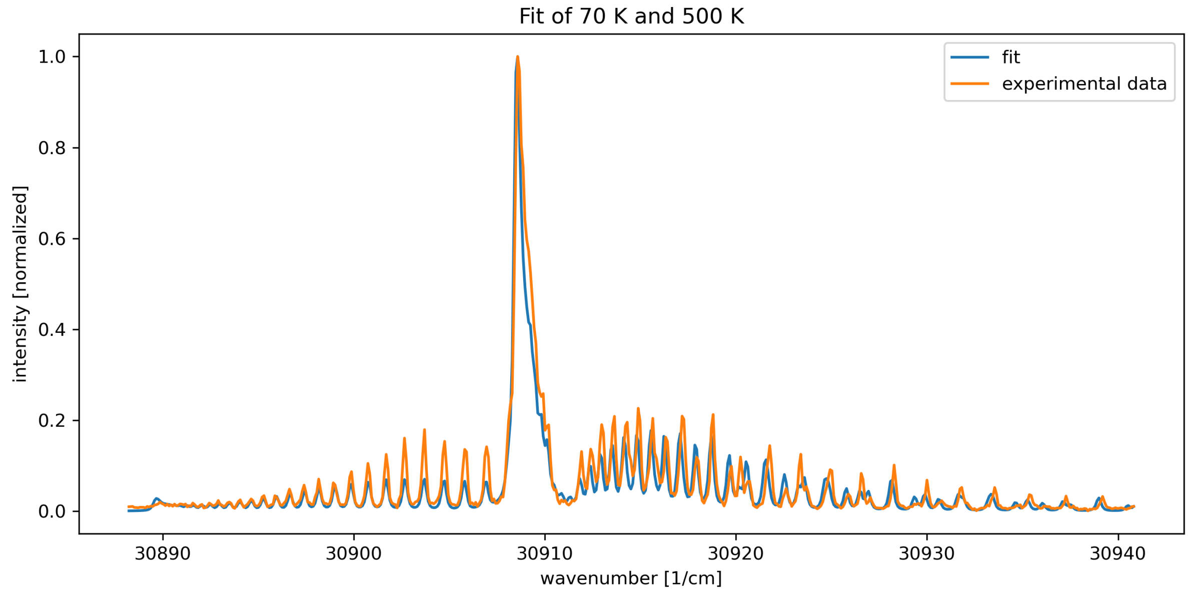

Figure A.28: Fit of spectra for 70 K and 500 K. The fit parameter results $c = 0.921 \pm 0.018$.

A.2 Pure nitrous oxide

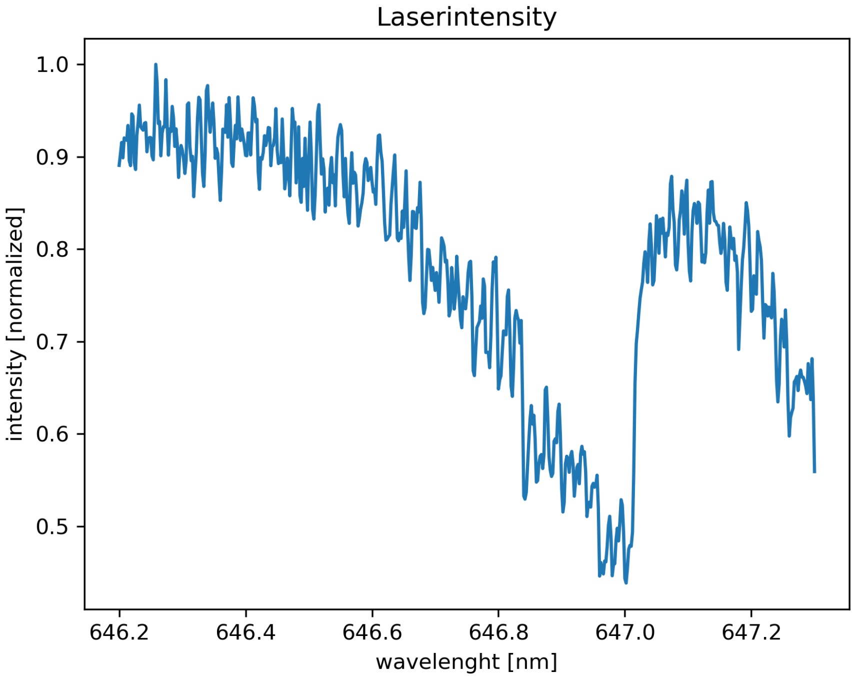

Figure A.29: The laser intensity of the pulsed dye laser for the measurement with pure N_2O.

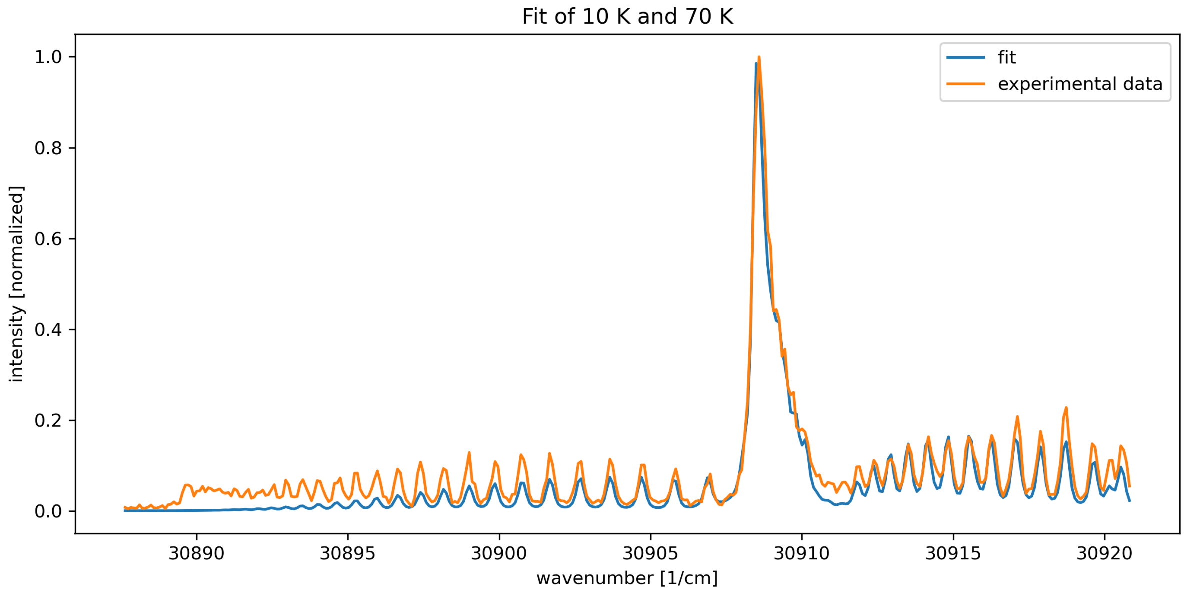

Figure A.30: Fit of spectra for 10 K and 70 K. The fit parameter results $c = 0.017 \pm 0.012$.

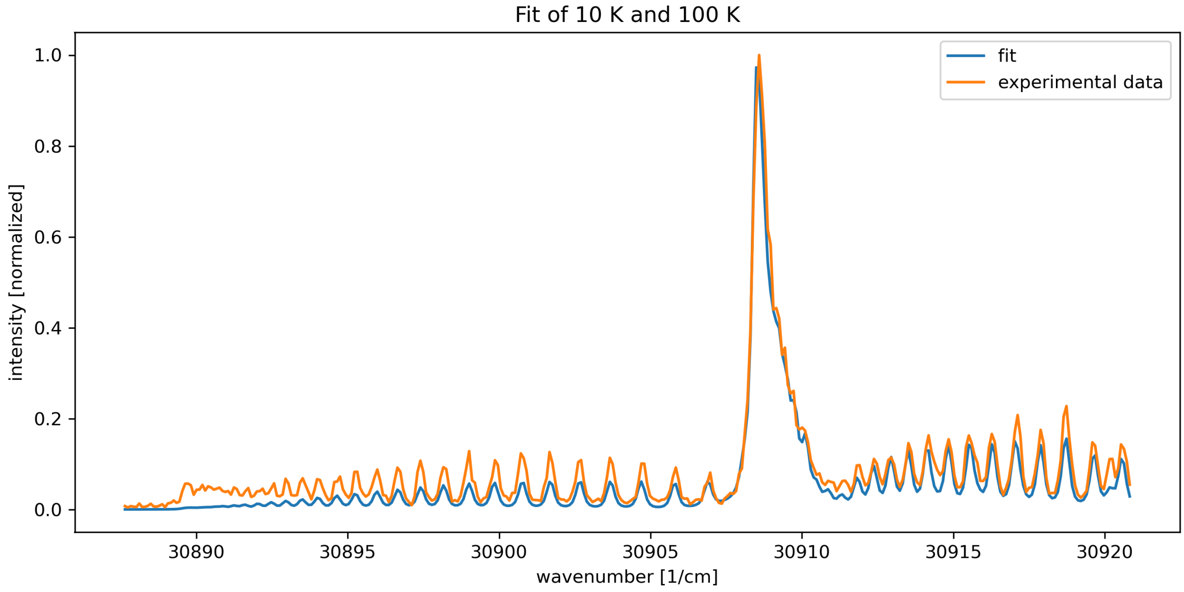

Figure A.31: Fit of spectra for 10 K and 100 K. The fit parameter results $c = 0.032 \pm 0.011$.

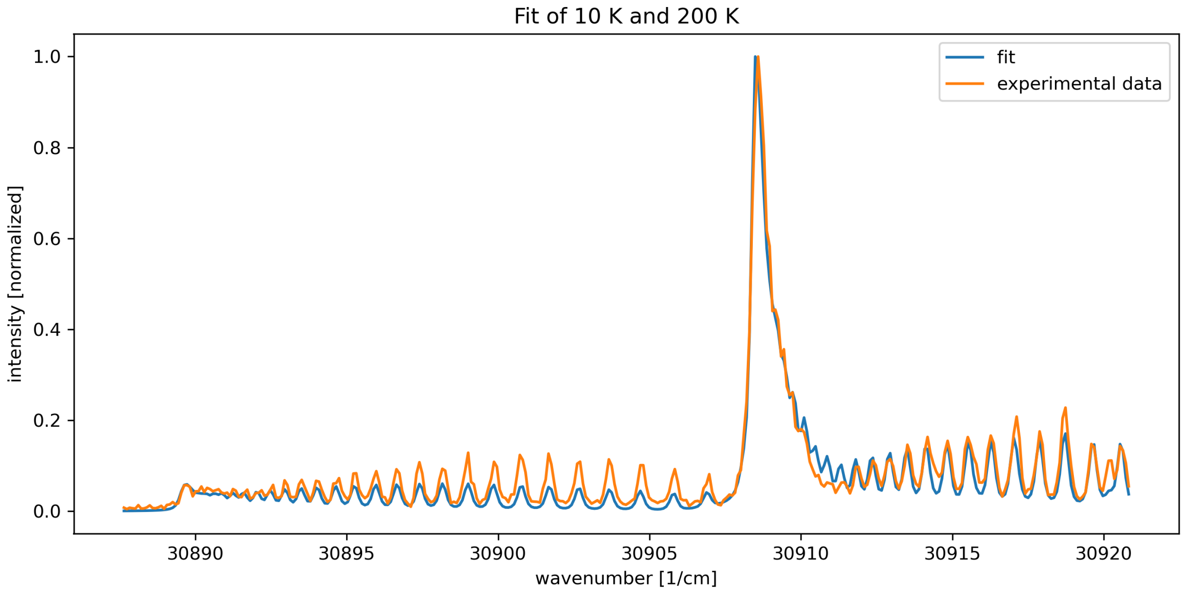

Figure A.32: Fit of spectra for 10 K and 200 K. The fit parameter results $c = 0.000 \pm 0.010$.

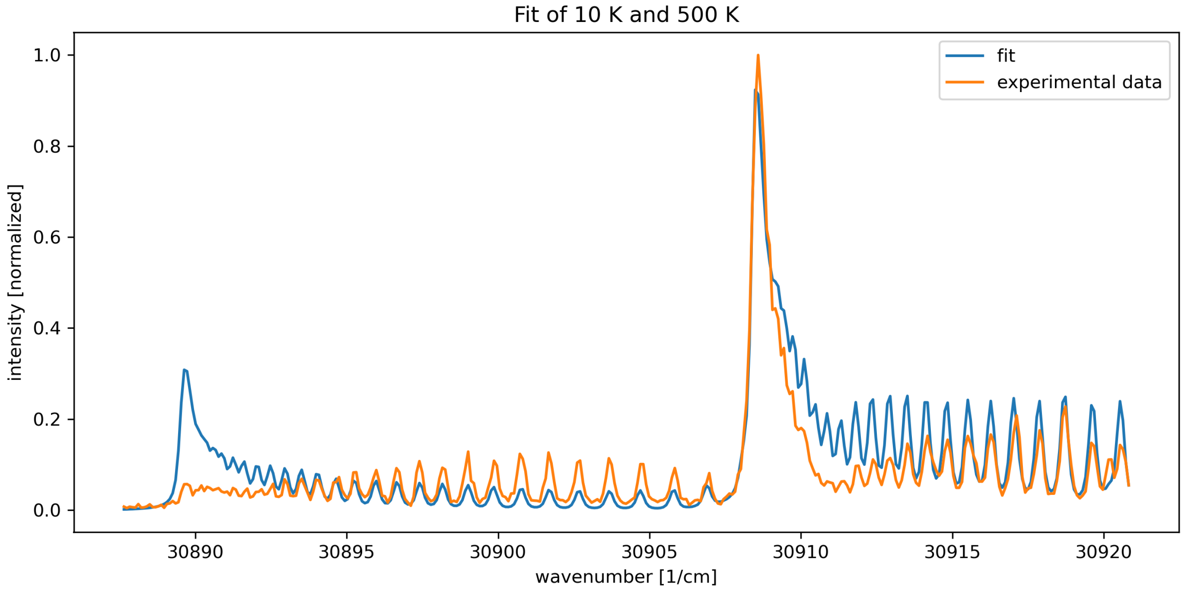

Figure A.33: Fit of spectra for 10 K and 500 K. The fit parameter results $c = 0.090 \pm 0.021$.

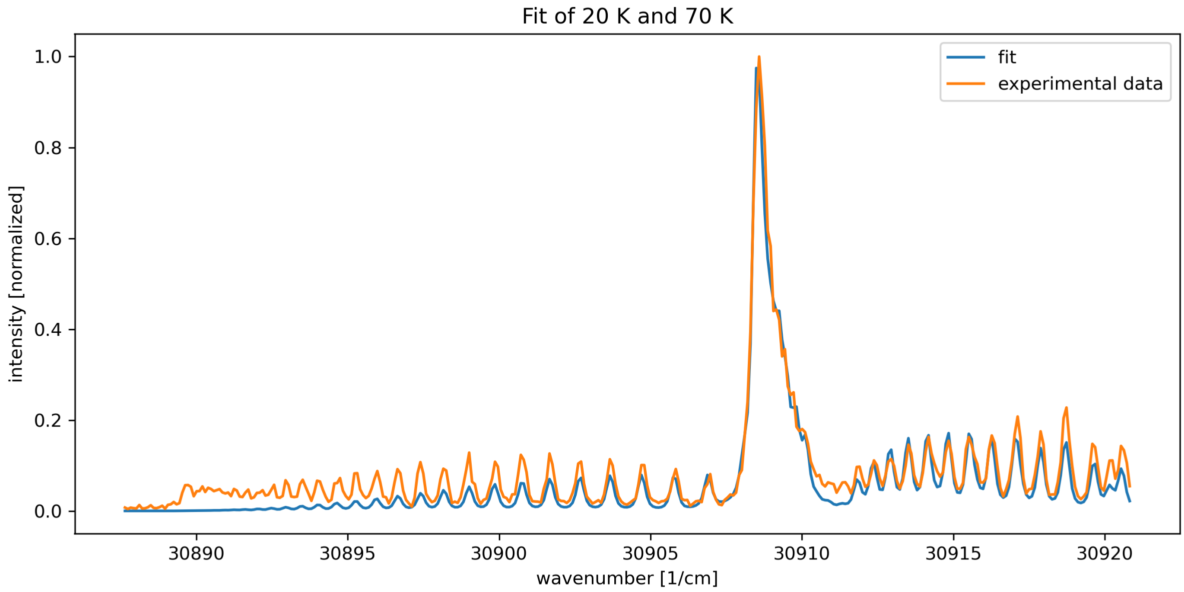

Figure A.34: Fit of spectra for 20 K and 70 K. The fit parameter results $c = 0.059 \pm 0.016$.

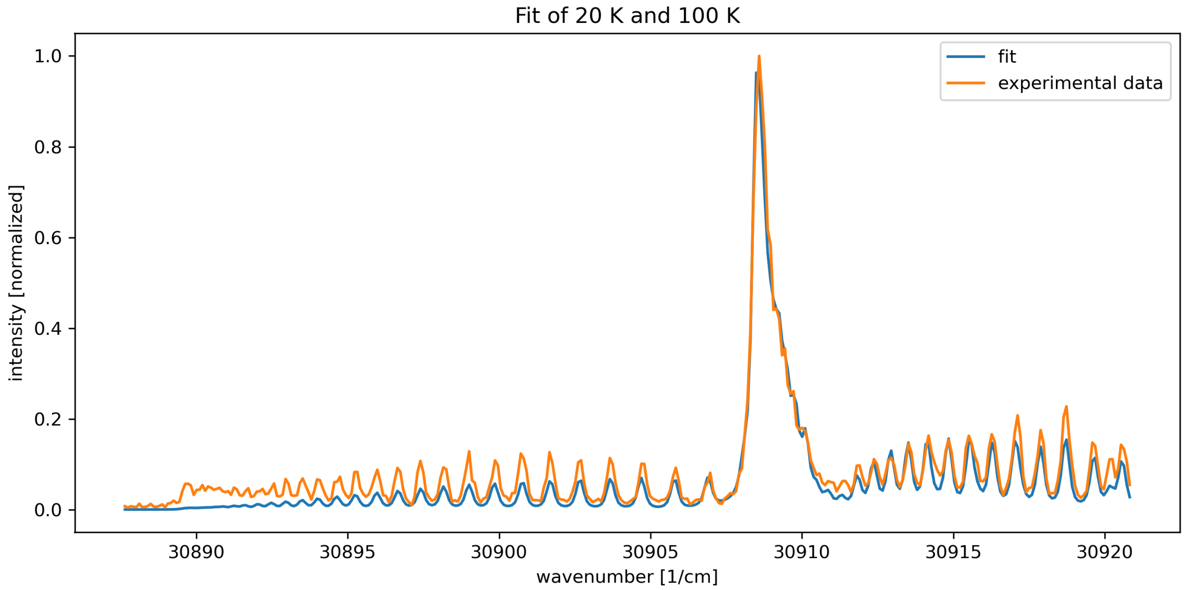

Figure A.35: Fit of spectra for 20 K and 100 K. The fit parameter results $c = 0.087 \pm 0.014$.

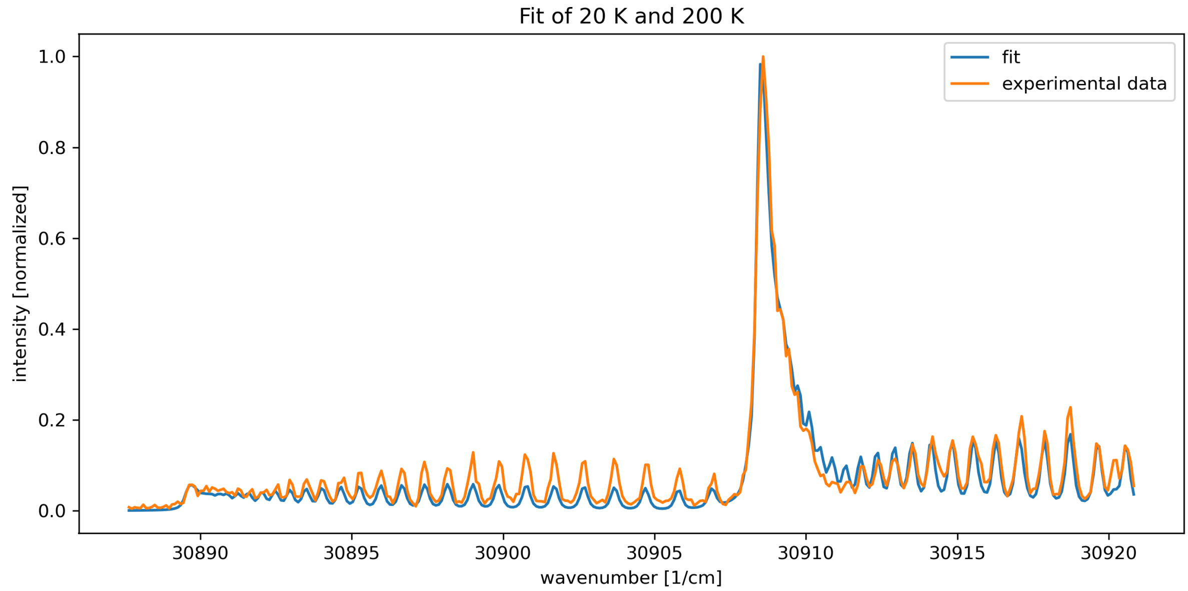

Figure A.36: Fit of spectra for 20 K and 200 K. The fit parameter results $c = 0.040 \pm 0.013$.

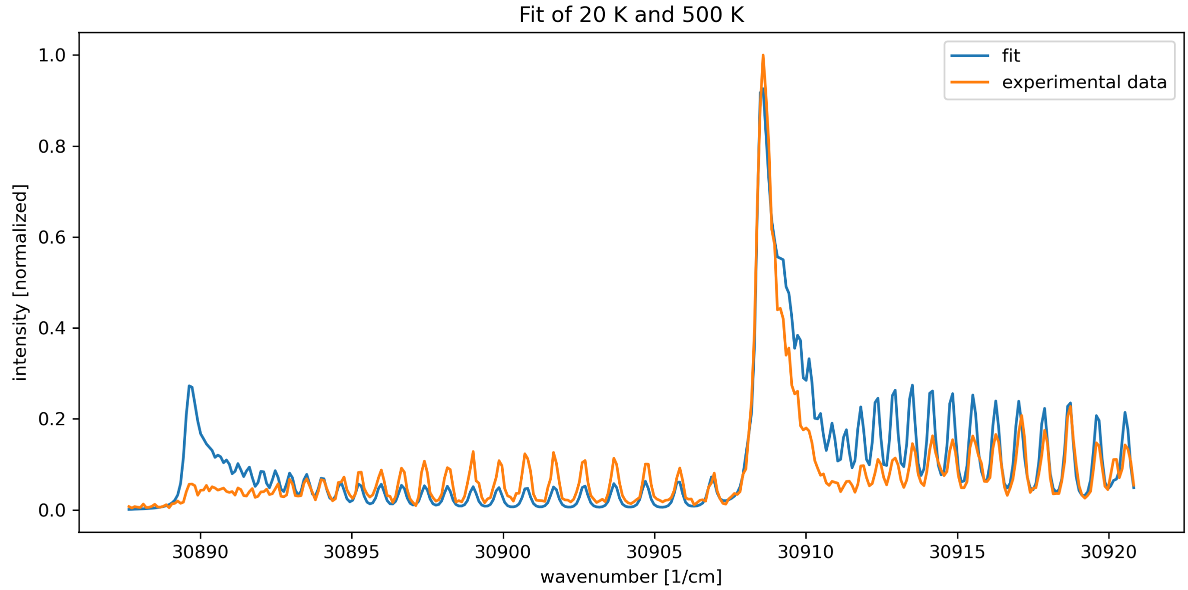

Figure A.37: Fit of spectra for 20 K and 500 K. The fit parameter results $c = 0.194 \pm 0.027$.

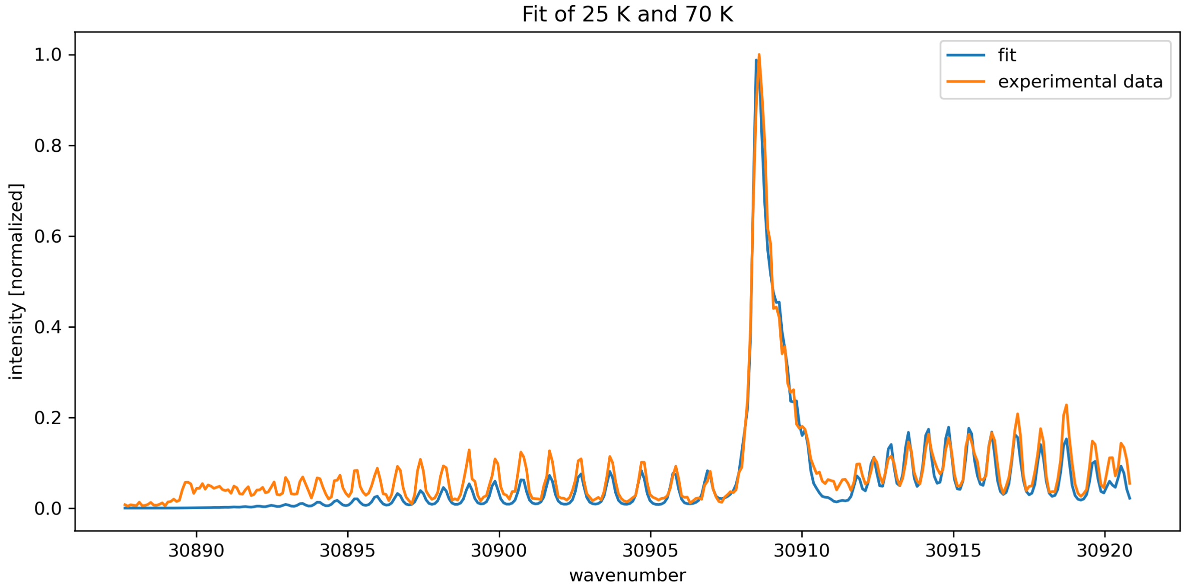

Figure A.38: Fit of spectra for 25 K and 70 K. The fit parameter results $c = 0.082 \pm 0.016$.

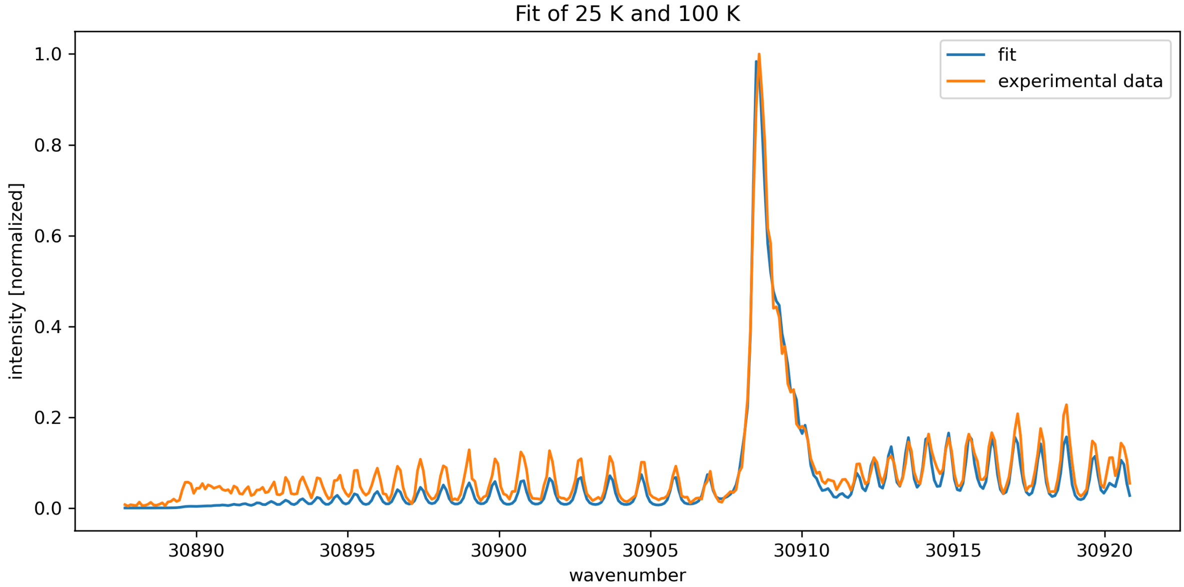

Figure A.39: Fit of spectra for 25 K and 100 K. The fit parameter results $c = 0.109 \pm 0.014$.

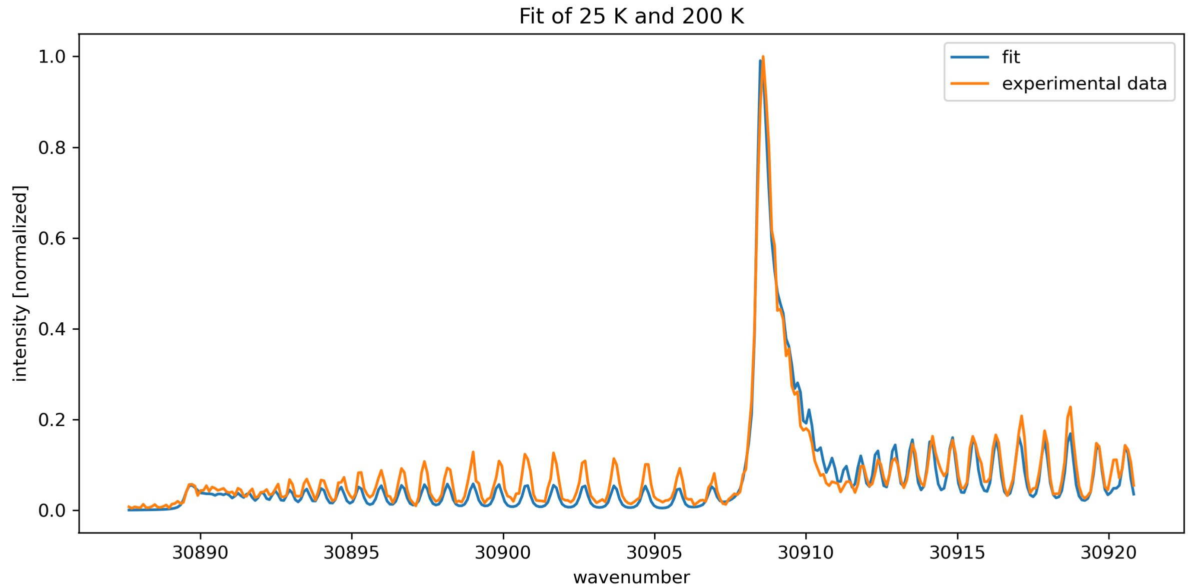

Figure A.40: Fit of spectra for 25 K and 200 K. The fit parameter results $c = 0.062 \pm 0.013$.

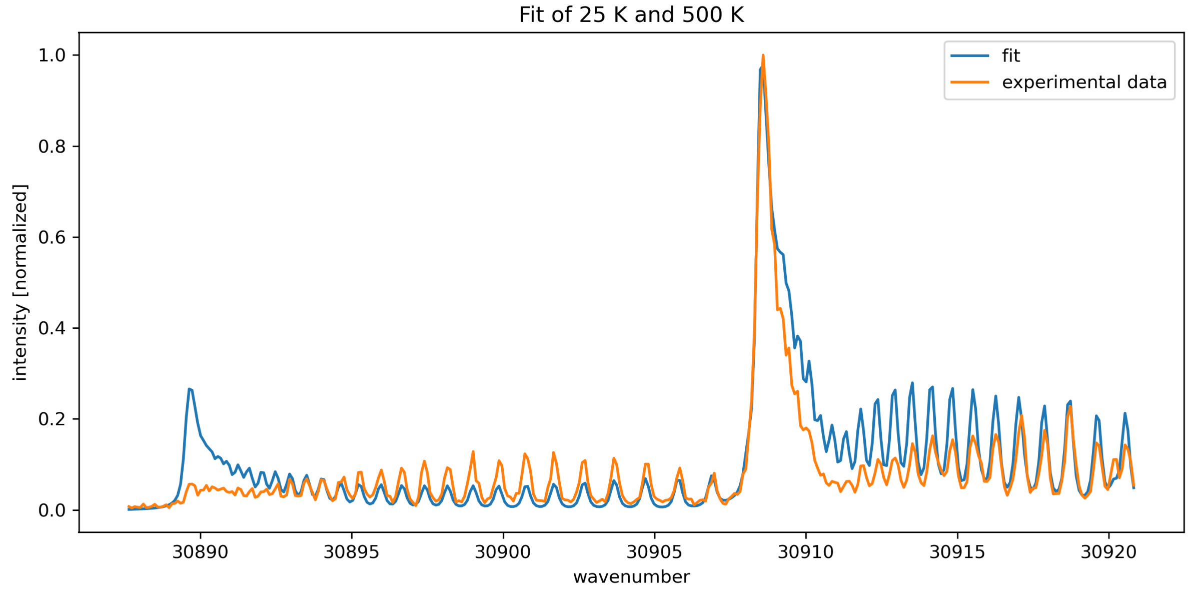

Figure A.41: Fit of spectra for 25 K and 500 K. The fit parameter results $c = 0.214 \pm 0.028$.

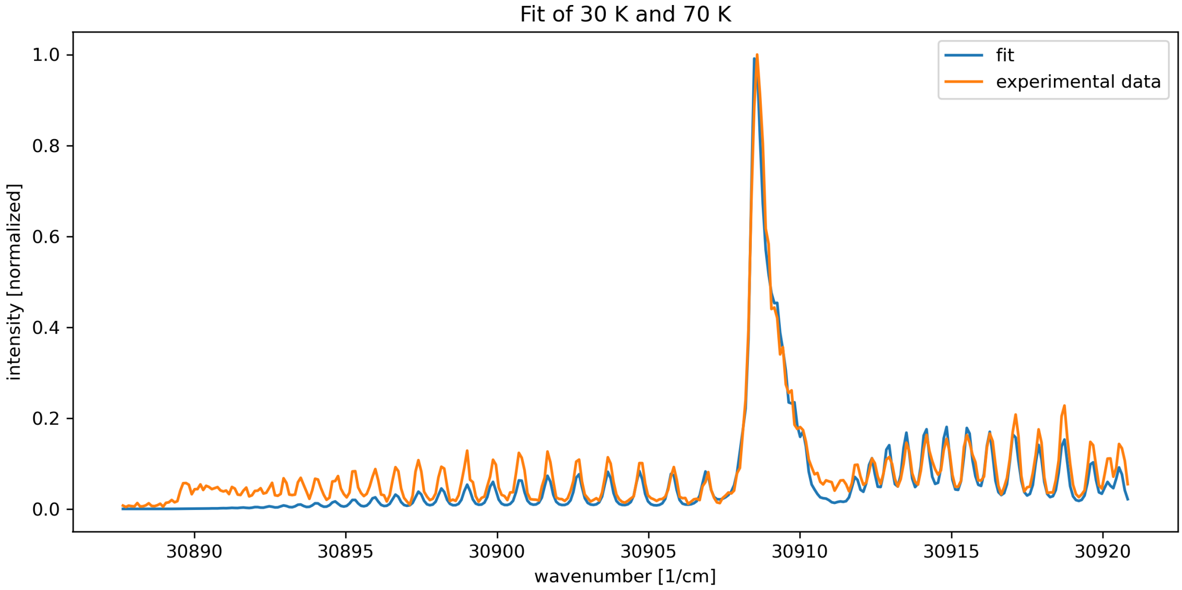

Figure A.42: Fit of spectra for 30 K and 70 K. The fit parameter results $c = 0.117 \pm 0.023$.

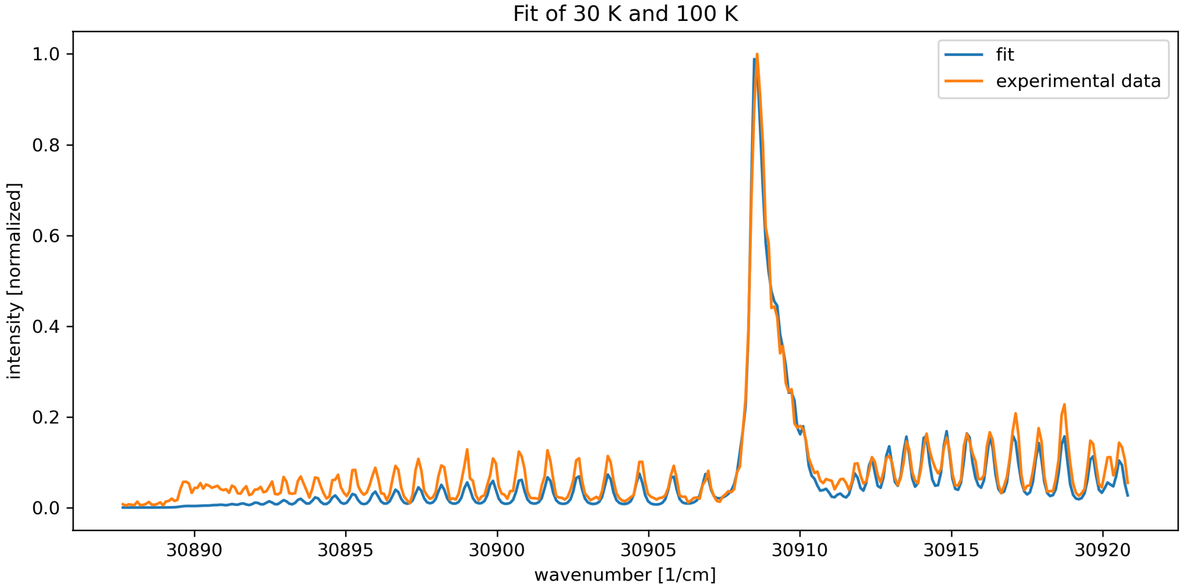

Figure A.43: Fit of spectra for 30 K and 100 K. The fit parameter results $c = 0.151 \pm 0.020$.

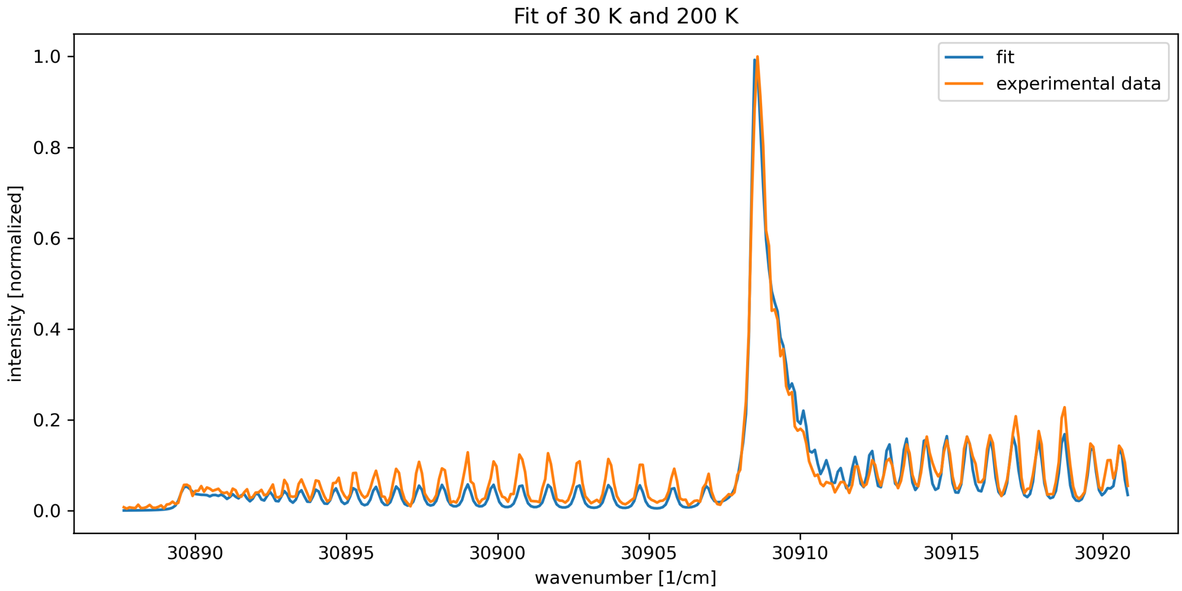

Figure A.44: Fit of spectra for 30 K and 200 K. The fit parameter results $c = 0.099 \pm 0.018$.

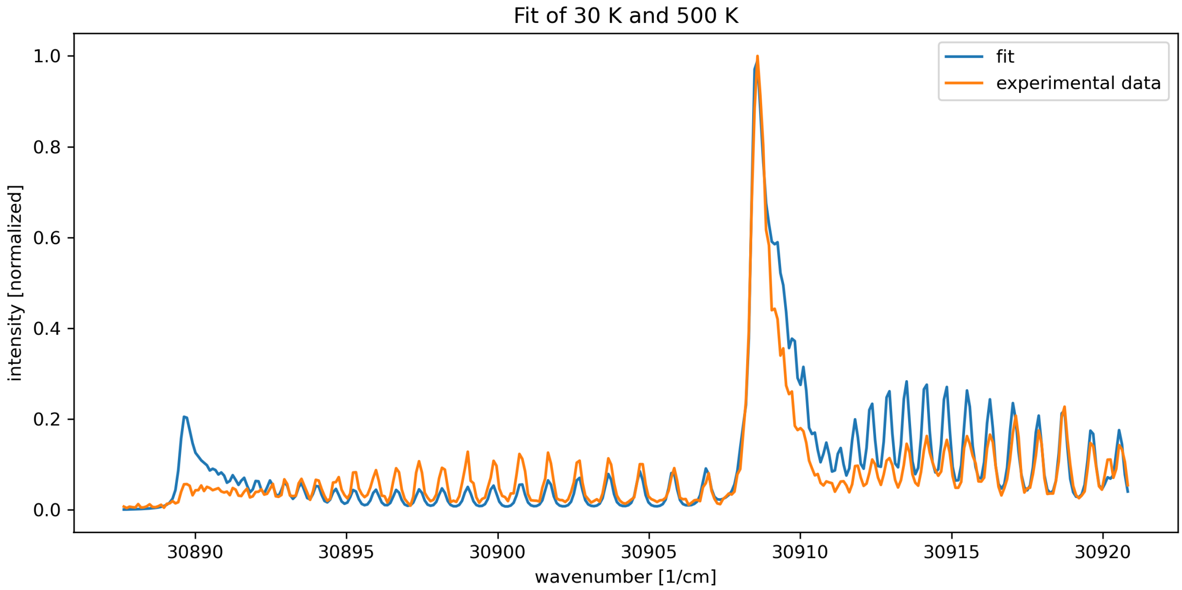

Figure A.45: Fit of spectra for 30 K and 500 K. The fit parameter results $c = 0.394 \pm 0.030$.

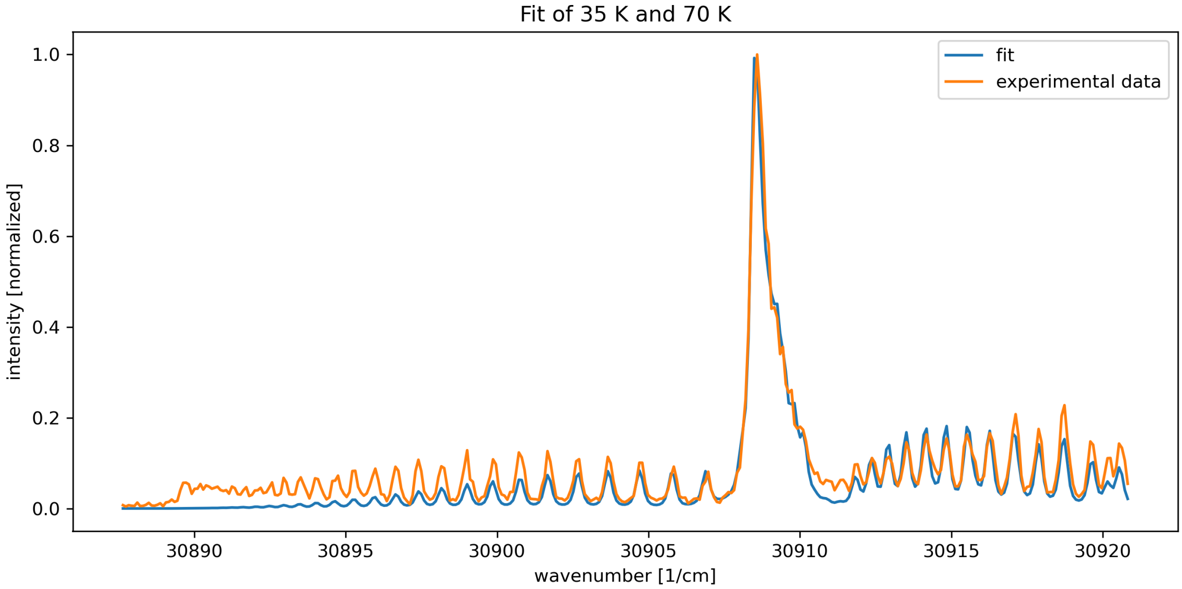

Figure A.46: Fit of spectra for 35 K and 70 K. The fit parameter results $c = 0.165 \pm 0.033$.

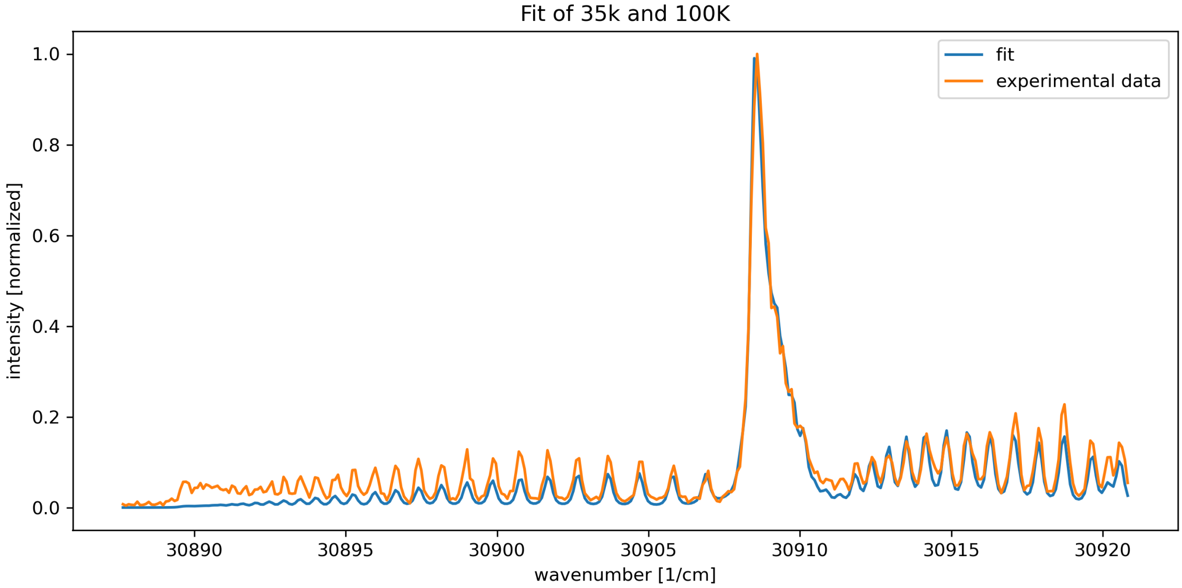

Figure A.47: Fit of spectra for 35 K and 100 K. The fit parameter results $c = 0.204 \pm 0.028$.

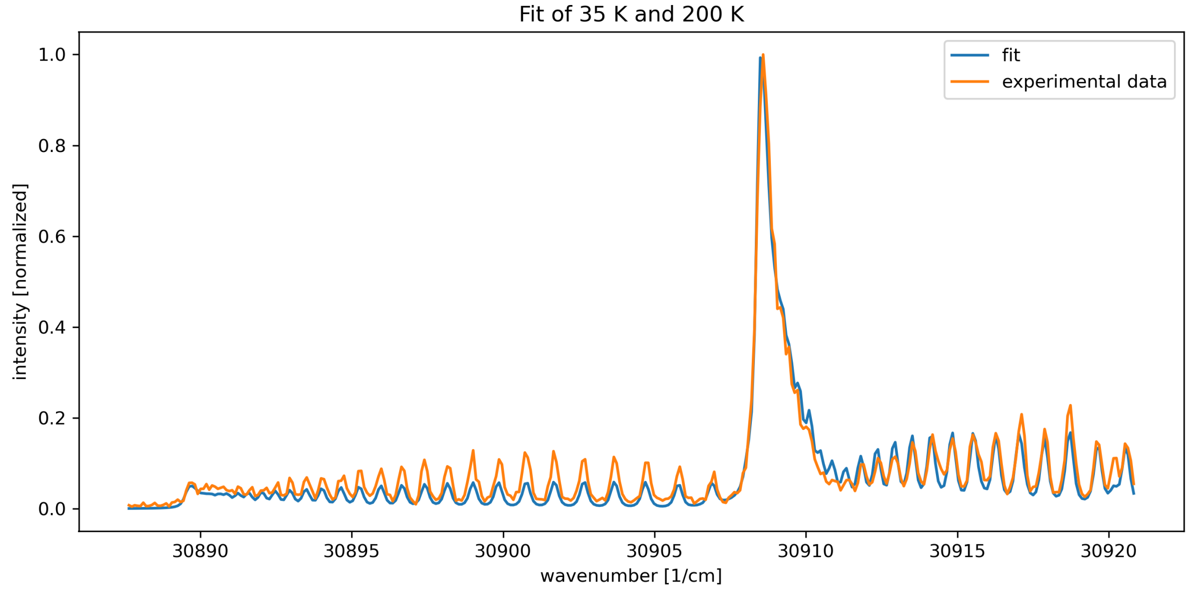

Figure A.48: Fit of spectra for 35 K and 200 K. The fit parameter results $c = 0.150 \pm 0.025$.

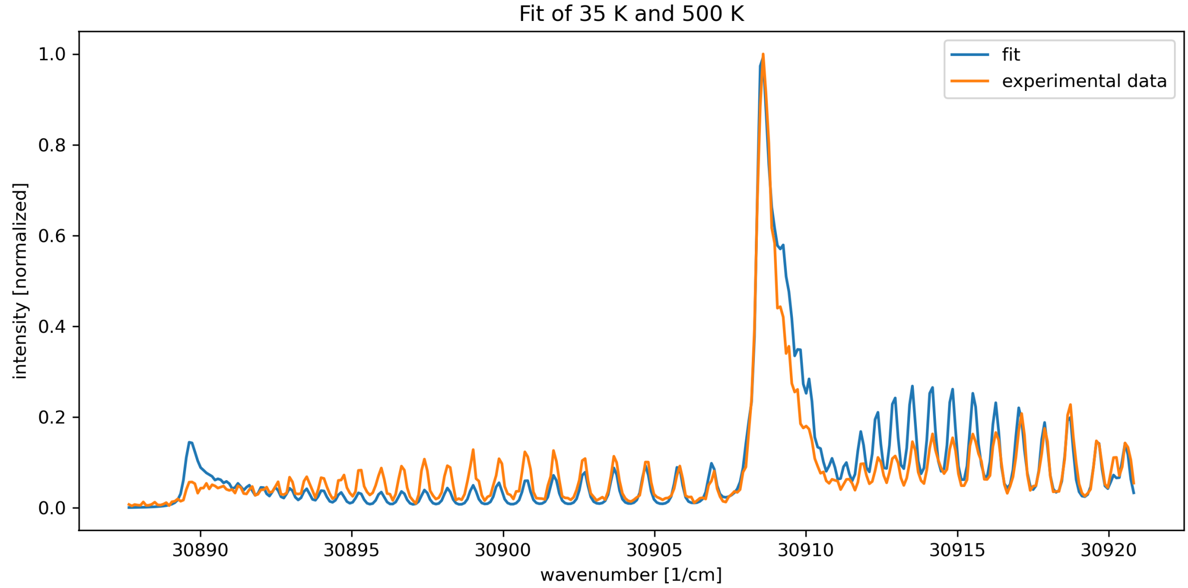

Figure A.49: Fit of spectra for 35 K and 500 K. The fit parameter results $c = 0.573 \pm 0.029$.

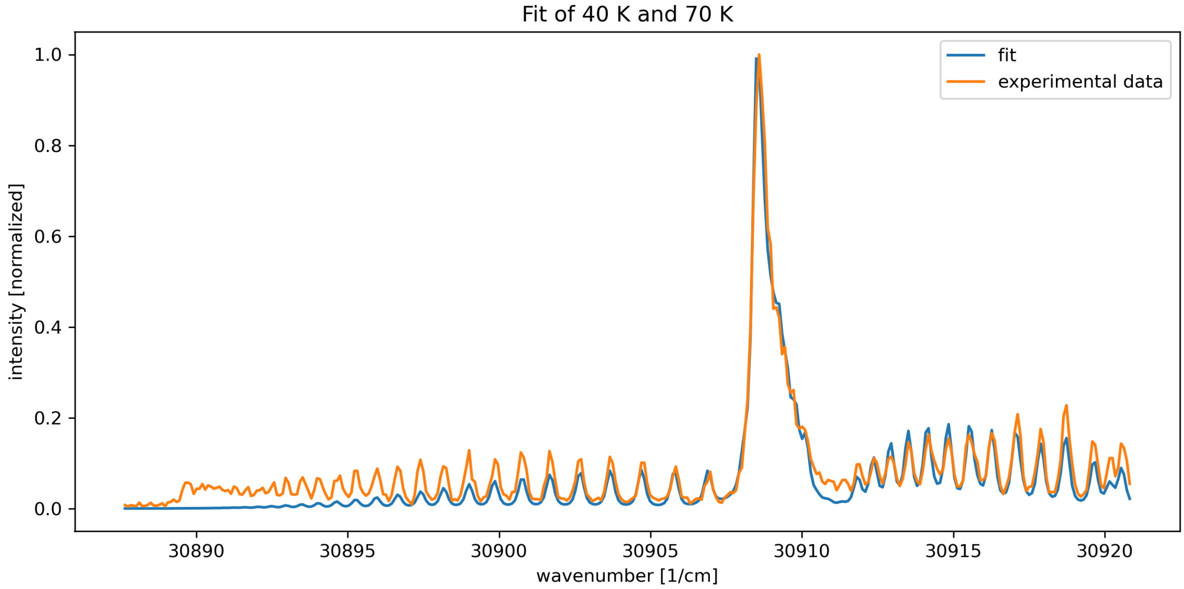

Figure A.50: Fit of spectra for 40 K and 70 K. The fit parameter results $c = 0.242 \pm 0.044$.

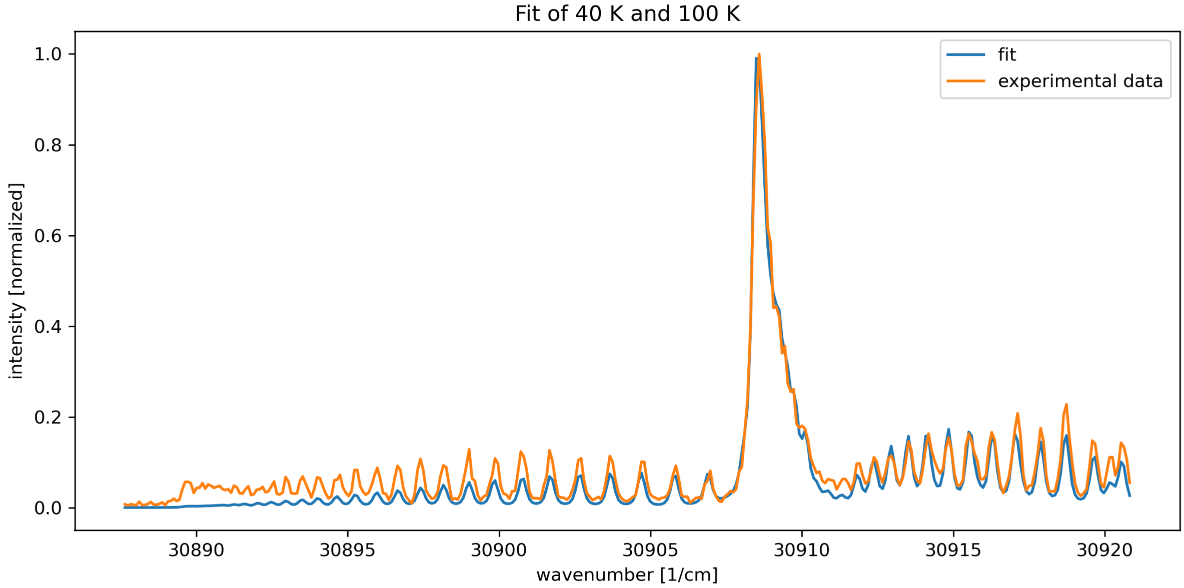

Figure A.51: Fit of spectra for 40 K and 100 K. The fit parameter results $c = 0.264 \pm 0.036$.

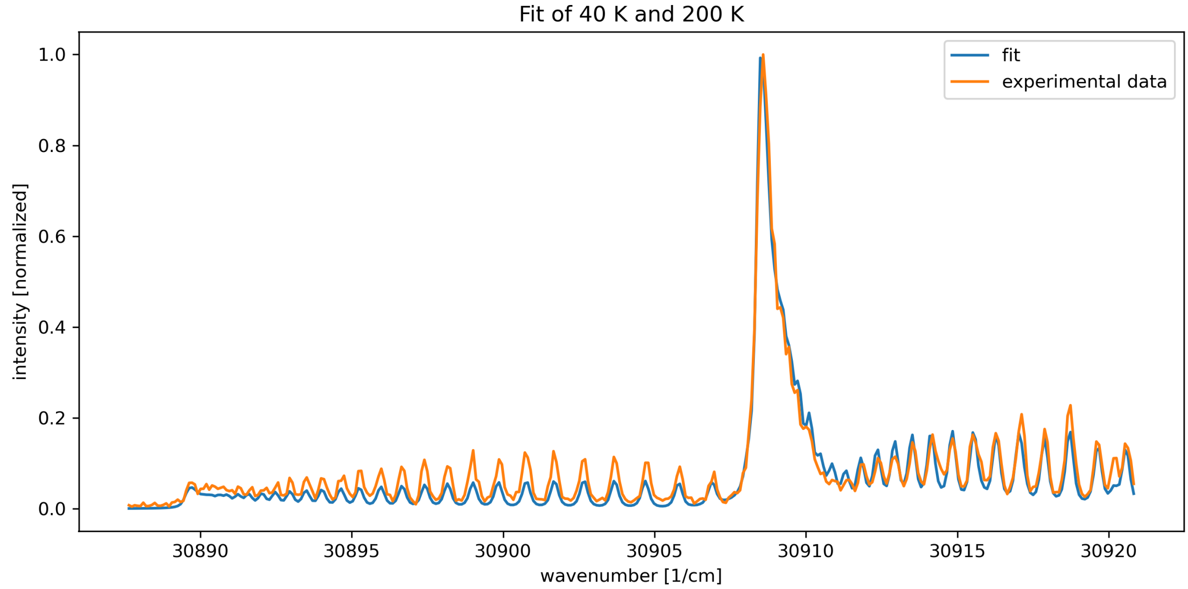

Figure A.52: Fit of spectra for 40 K and 200 K. The fit parameter results $c = 0.209 \pm 0.031$.

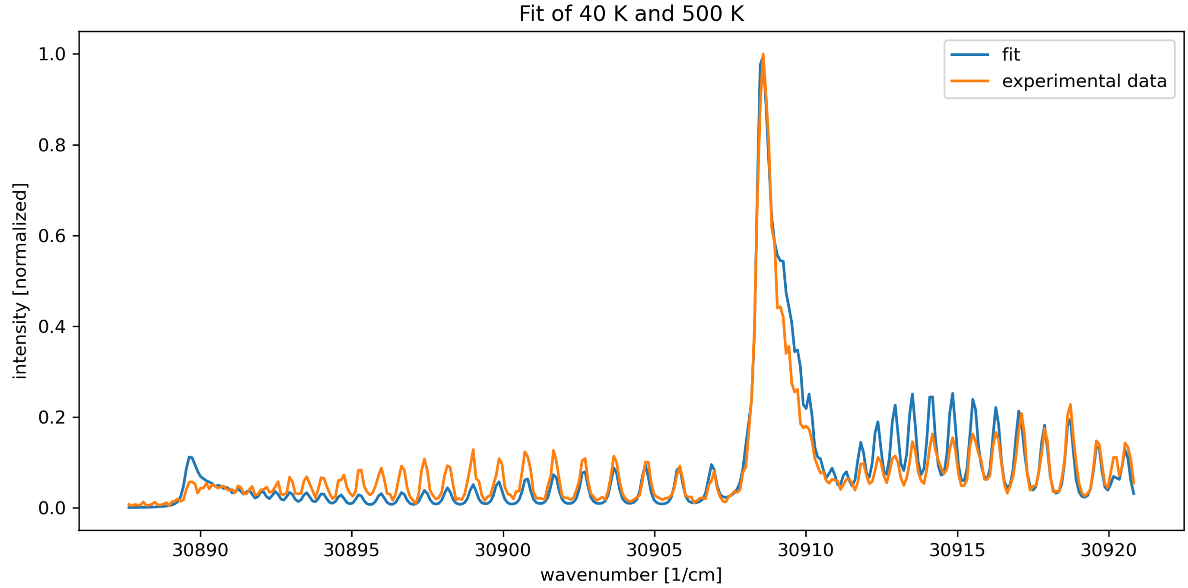

Figure A.53: Fit of spectra for 40 K and 500 K. The fit parameter results $c = 0.670 \pm 0.026$.

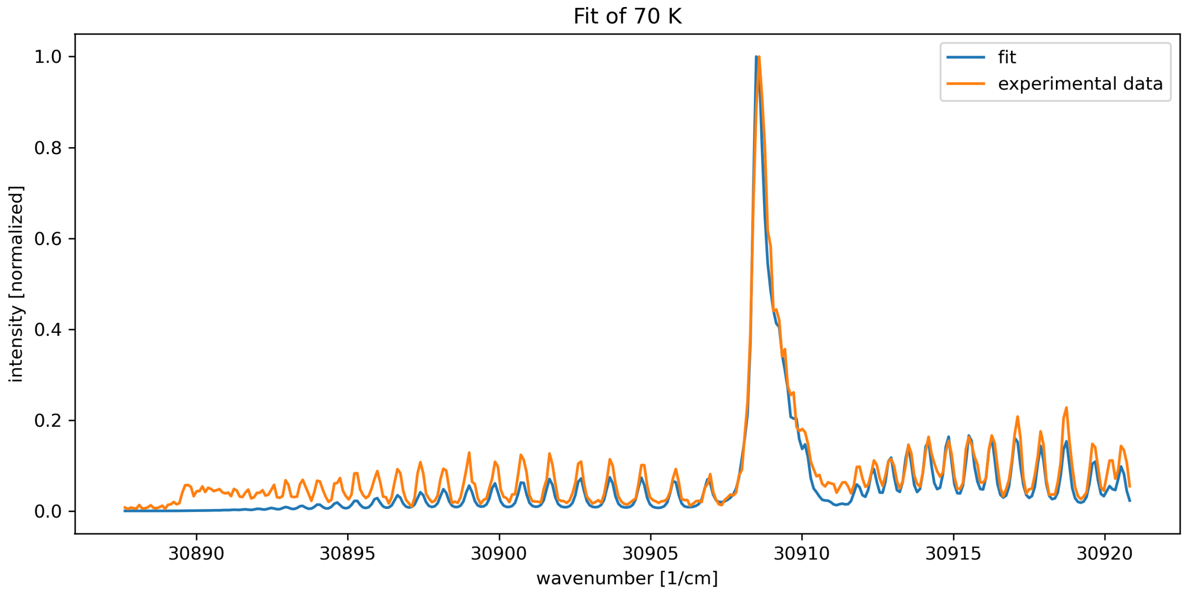

Figure A.54: Spectrum for 70 K.

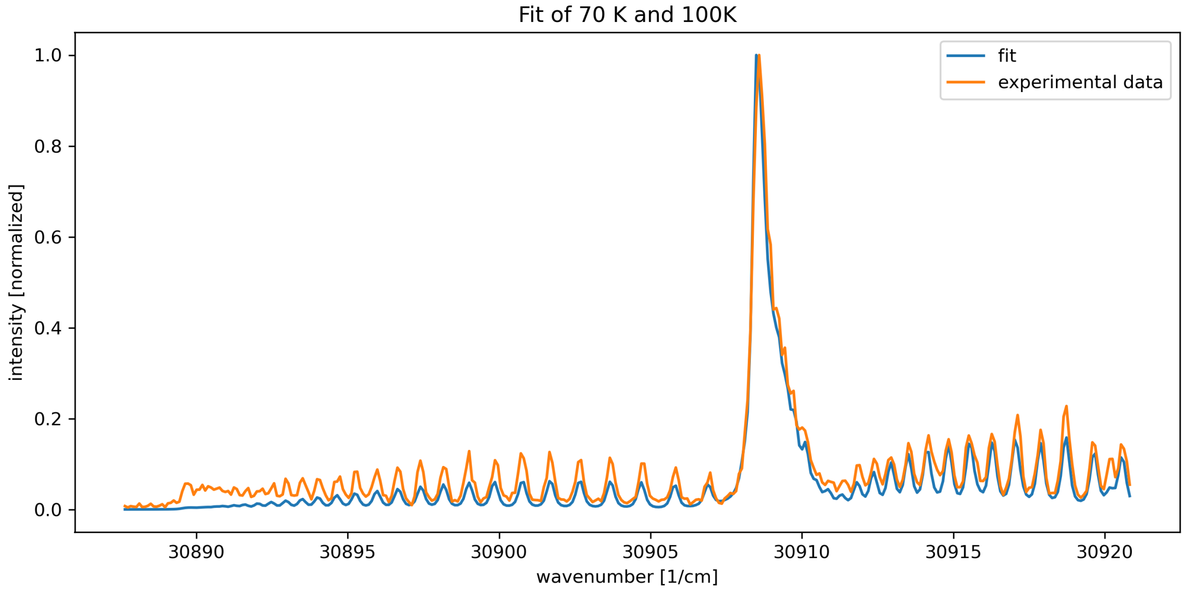

Figure A.55: Fit of spectra for 70 K and 100 K. The fit parameter results $c = 0.00 \pm 0.189$.

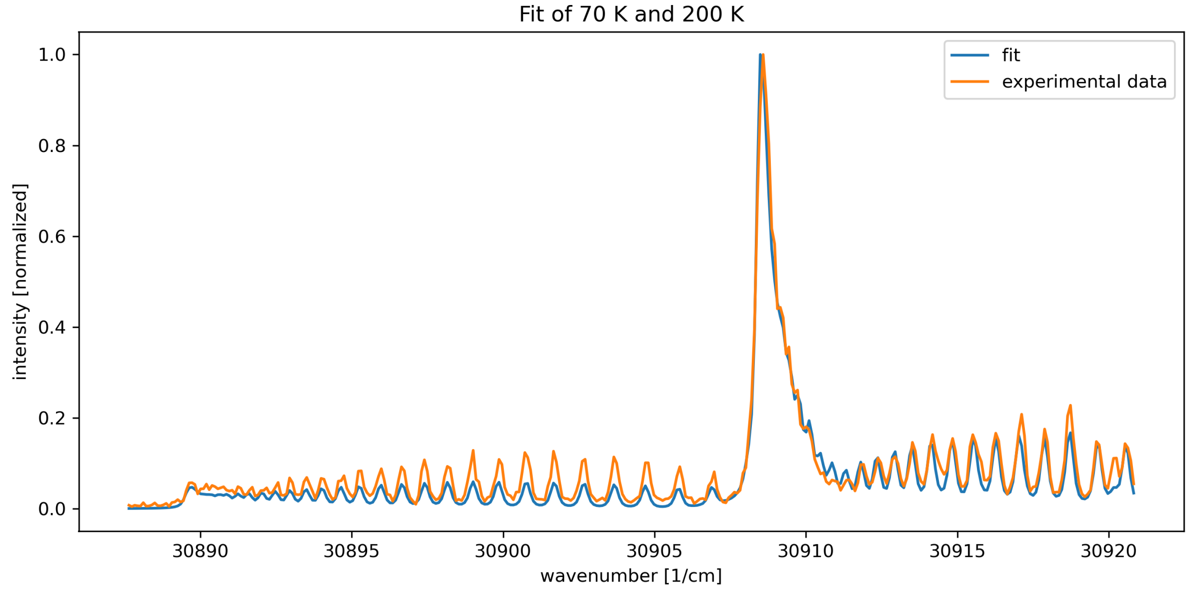

Figure A.56: Fit of spectra for 70 K and 200 K. The fit parameter results $c = 0.201 \pm 0.058$.

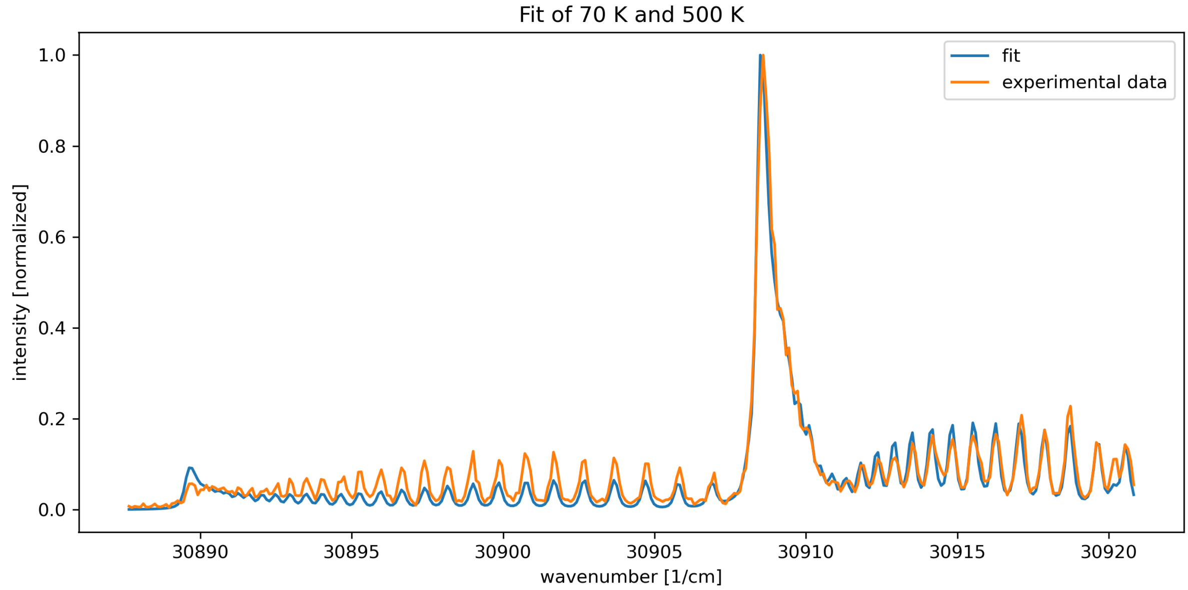

Figure A.57: Fit of spectra for 70 K and 500 K. The fit parameter results $c = 0.729 \pm 0.018$.

Bibliography

Amitay, Z., D. Zajfman, and P. Forck (1994). 'Rotational and vibrational lifetime of isotopically asymmetrized homonuclear diatomic molecular ions.' In: *Phys. Rev. A* 50 (3), pp. 2304–2308. DOI: `10.1103/PhysRevA.50.2304`.

Anaclerio, Giuseppe et al. (2022). 'Numerical characterization of hydrogen under-expanded jets: influence of the nozzle cross-section shape.' In: *Journal of Physics: Conference Series* 2385.1, p. 012046. DOI: `10.1088/1742-6596/2385/1/012046`.

Anderson, J. B. and J. B. Fenn (1965). 'Velocity Distributions in Molecular Beams from Nozzle Sources.' In: *The Physics of Fluids* 8.5, pp. 780–787. DOI: `10.1063/1.1761320`.

Bejjani, Raghed (2021). 'Conception, construction and validation of scientific instruments to study the spectrum of cold ionic species.' PhD thesis. University of Rennes.

Bejjani, Raghed et al. (2021). 'STARGATE: A new instrument for high-resolution photodissociation spectroscopy of cold ionic species.' In: *Review of Scientific Instruments* 92 (3). DOI: `10.1063/5.0039627/1061494`.

Bernath, Peter F. (2016). *Spectra of Atoms and Molecules.* Oxford University Press.

Bondi, A. (1964). 'van der Waals Volumes and Radii.' In: *The Journal of Physical Chemistry* 68.3, pp. 441–451. DOI: `10.1021/j100785a001`. eprint: `https://doi.org/10.1021/j100785a001`.

Bunker, P.R. (1974). 'Allowed transitions and the dipole moment of HD^+.' In: *Chemical Physics Letters* 27.3, pp. 322–324. DOI: `https://doi.org/10.1016/0009-2614(74)90233-4`.

Christen, Wolfgang, Klaus Rademann, and Uzi Even (2006). 'Efficient cooling in supersonic jet expansions of supercritical fluids: CO and CO2.' In: *The Journal of chemical physics* 125.17.

Coppola, C. M., L. Lodi, and J. Tennyson (2011). 'Radiative cooling functions for primordial molecules.' In: *Monthly Notices of the Royal Astronomical Society* 415.1. See supplementary Material at `https://www.exomol.com/data/molecules/H2_p/1H-2H_p/CLT/` Accessed: Jul 21 2023, pp. 487–493. DOI: `10.1111/j.1365-`

2966.2011.18723.x. eprint: https://academic.oup.com/mnras/article-pdf/415/1/487/3126743/mnras0415-0487.pdf.

Fellows, C. E. (2013). 'Improved molecular constants of the 000-000 band of the electronic transition $A^2\Sigma^+ - X^2\Pi$ of N_2O^+ radical.' In: *The Journal of Chemical Physics* 138.16, p. 164316. DOI: 10.1063/1.4802055. eprint: https://pubs.aip.org/aip/jcp/article-pdf/doi/10.1063/1.4802055/13017631/164316_1_online.pdf.

Frey, R., R. Kakoschke, and E.W. Schlag (1982). 'Spectroscopy of molecular ions: Laser-induced fragmentation spectra of N_2O^+,$A^2\Sigma^+ - X^2\Pi$.' In: *Chemical Physics Letters* 93.3, pp. 227–231. DOI: https://doi.org/10.1016/0009-2614(82)80128-0.

Gauthier, Michel (1988). 'Spectra and structure of nitrous oxide dimers and clusters.' In: *The Journal of chemical physics* 88.9, pp. 5439–5449.

Geballe, TR and T Oka (1996). 'Detection of H+ 3 in interstellar space.' In: *Nature* 384.6607, pp. 334–335.

Girin, Oleksandr (2022). *Dynamics of Compressible Fluids.* Springer.

Glosik, J et al. (2000). 'The recombination of H_3^+ ions with electrons: dependence on partial pressure of H_2.' In: *Chemical Physics Letters* 331.2-4, pp. 209–214.

Grussie, F. et al. (2022). 'An ion-atom merged beams setup at the Cryogenic Storage Ring.' In: *Review of Scientific Instruments* 93.5, p. 053305. DOI: 10.1063/5.0086391. eprint: https://pubs.aip.org/aip/rsi/article-pdf/doi/10.1063/5.0086391/16665382/053305_1_online.pdf.

Grussie, Florian (2023). *Personal communication.*

Hahn, R. von et al. (2016). 'The cryogenic storage ring CSR.' In: *Review of Scientific Instruments* 87.6, p. 063115. DOI: 10.1063/1.4953888.

Hilborn, Robert C. (1982). 'Einstein coefficients, cross sections, f values, dipole moments, and all that.' In: *American Journal of Physics* 50.11, pp. 982–986. DOI: 10.1119/1.12937. eprint: https://pubs.aip.org/aapt/ajp/article-pdf/50/11/982/11835413/982_1_online.pdf.

Hirota, A. et al. (2020). 'Radiative cooling dynamics of isolated N_2O^+ ions in a cryogenic electrostatic ion storage ring.' In: *Phys. Rev. A* 102 (2), p. 023119. DOI: 10.1103/PhysRevA.102.023119.

Imasaka, Totaro, D. S. Moore, and T. Vo-Dinh (2003). In: *Pure and Applied Chemistry* 75.7, pp. 975–998. DOI: doi:10.1351/pac200375070975.

Kreckel, H et al. (2002). 'Vibrational and rotational cooling of H_3^+.' In: *Physical Review A* 66.5, p. 052509.

Kreckel, H. et al. (2004). 'Rovibrational relaxation model for H_3^+.' In: *New Journal of Physics* 6, pp. 151–151. DOI: 10.1088/1367-2630/6/1/151.

Kreckel, Holger (2023). *Personal communication.*

Kreckel, Holger et al. (2010). 'High-resolution storage-ring measurements of the dissociative recombination of H_3^+ using a supersonic expansion ion source.' In: *Physical Review A* 82.4, p. 042715.

Lammich, L et al. (2003). 'Evidence for subthermal rotational populations in stored molecular ions through state-dependent dissociative recombination.' In: *Physical review letters* 91.14, p. 143201.

Larsson, M et al. (2003). 'Studies of dissociative recombination in CRYRING.' In: *Dissociative recombination of molecular ions with electrons*, pp. 87–94.

Luo, Fei et al. (1993). 'The weakest bond: Experimental observation of helium dimer.' In: *The Journal of Chemical Physics* 98.4, pp. 3564–3567. DOI: `10.1063/1.464079`. eprint: `https://pubs.aip.org/aip/jcp/article-pdf/98/4/3564/15361963/3564\_1\_online.pdf`.

MassSpecpecD BV (n.d.). *Specifications.* `https://www.amsterdampiezovalve.com/specifications`. Accessed: Jul 25 2023.

McCall, Benjamin J et al. (2002). 'Observations of H_3^+ in the diffuse interstellar medium.' In: *The Astrophysical Journal* 567.1, p. 391.

McCall, Benjamin J. (2001). 'Spectroscopy of H_3^+ in laboratory and astrophysical plasmas.' PhD thesis. University of Chicago.

McCall, BJ et al. (1998). 'Detection of H_3^+ in the diffuse interstellar medium toward Cygnus OB2 No. 12.' In: *Science* 279.5358, pp. 1910–1913.

McCall, BJ et al. (2004). 'Dissociative recombination of rotationally cold H_3^+.' In: *Physical Review A* 70.5, p. 052716.

Meyer, C. et al. (2017). 'Radiative Rotational Lifetimes and State-Resolved Relative Detachment Cross Sections from Photodetachment Thermometry of Molecular Anions in a Cryogenic Storage Ring.' In: *Phys. Rev. Lett.* 119 (2), p. 023202. DOI: `10.1103/PhysRevLett.119.023202`.

Morse, Michael D. (1996). '2 - Supersonic Beam Sources.' In: *Atomic, Molecular, and Optical Physics: Atoms and Molecules.* Ed. by F.B. Dunning and Randall G. Hulet. Vol. 29. Experimental Methods in the Physical Sciences. Academic Press, pp. 21–47. DOI: `https://doi.org/10.1016/S0076-695X(08)60784-X`.

NASA Glenn Research Center (n.d.[a]). *Expansion Fan.* Ed. by Tom Benson. `https://www.grc.nasa.gov/www/BGH/expans.html`. Last updated: May 07 2021, Accessed: Jul 15 2023.

NASA Glenn Research Center (n.d.[b]). *Isentropic Flow Equation Derivations.* Ed. by Nancy Hall. `https://www.grc.nasa.gov/www/k-12/airplane/isndrv.html`. Last updated: May 13 2021, Accessed: Jul 15 2023.

NASA Glenn Research Center (n.d.[c]). *Mass Flow Choking.* Ed. by Nancy Hall. `https://www.grc.nasa.gov/www/k-12/airplane/mflchk.html`. Last updated: May 13 2021, Accessed: Jul 15 2023.

NASA Glenn Research Center (n.d.[d]). *Normal Shock Wave.* Ed. by Nancy Hall. `https://www.grc.nasa.gov/www/k-12/airplane/normal.html`. Last updated: May 13 2021, Accessed: Jul 15 2023.

NASA Photo (n.d.[a]). *NASA Armstrong Fact Sheet: SR-71 Blackbird.* Ed. by Yvonne Gibbs. `https://www.nasa.gov/centers/armstrong/news/FactSheets/FS-030-DFRC.html`. Last updated: Aug 07 2017, Accessed: Jul 15 2023.

NASA Photo (n.d.[b]). *Schlieren Images Reveal Supersonic Shock Waves*. Ed. by Monroe Conner. `https://www.nasa.gov/centers/armstrong/multimedia/imagegallery/schlieren/AirBOS_F7_P5.html`. Last updated: Aug 17 2017, Accessed: Jul 15 2023.

National Institute of Standards and Technology (n.d.[a]). *Thermophysical Properties of Argon*. `https://webbook.nist.gov/cgi/fluid.cgi?ID=C7440371&Action=Page`. Accessed: Jul 15 2023.

National Institute of Standards and Technology (n.d.[b]). *Thermophysical Properties of nitrous oxide*. `https://webbook.nist.gov/cgi/fluid.cgi?ID=C10024972&Action=Page`. Accessed: Jul 24 2023.

Nuesslein, Felix (2023). *Personal communication*.

O'Connor, A. P. et al. (2016). 'Photodissociation of an Internally Cold Beam of CH^+ Ions in a Cryogenic Storage Ring.' In: *Phys. Rev. Lett.* 116 (11), p. 113002. DOI: `10.1103/PhysRevLett.116.113002`.

Pontes, José, Norberto Mangiavacchi, and Gustavo R. Anjos (2019). *An Introduction to Compressible Flows with Applications Quasi-One-Dimensional Approximation and General Formulation for Subsonic, Transonic and Supersonic Flows*. Springer.

Poth, L et al. (1997). 'Metastable dissociation study of nitric oxide clusters.' In: *The Journal of Physical Chemistry A* 101.6, pp. 1099–1103.

Proch, D and T Trickl (1989). 'A high-intensity multi-purpose piezoelectric pulsed molecular beam source.' In: *Review of Scientific Instruments* 60.4, pp. 713–716.

Saha, Samir (1974). 'The electric dipole moment of HD^+ molecular ion.' In: *Indian Journal of Physics* 48, pp. 849–852.

Schlemmer, Stephan, Thomas Giesen, and Harald Mutschke (2014). *Laboratory astrochemistry: from molecules through nanoparticles to grains*. John Wiley & Sons.

Snow, Theodore P and Veronica M Bierbaum (2008). 'Ion chemistry in the interstellar medium.' In: *Annu. Rev. Anal. Chem.* 1, pp. 229–259.

Tsikritea, Andriana et al. (2022). 'Capture theory models: An overview of their development, experimental verification, and applications to ion–molecule reactions.' In: *The Journal of Chemical Physics* 157.6, p. 060901. DOI: `10.1063/5.0098552`. eprint: `https://pubs.aip.org/aip/jcp/article-pdf/doi/10.1063/5.0098552/16547114/060901\_1\_online.pdf`.

Wang, Hua et al. (2010). 'Predissociation dynamics of N_2O^+ at the $A\Sigma_2^+$ state: Three pathways to form $NO^+\Sigma_1^+$) revealed from ion velocity imaging.' In: *The Journal of Chemical Physics* 132.24, p. 244309. DOI: `10.1063/1.3457945`. eprint: `https://pubs.aip.org/aip/jcp/article-pdf/doi/10.1063/1.3457945/16121971/244309\_1\_online.pdf`.

Wang, Jue et al. (1988). 'Speed ratios greater than 1000 and temperatures less than 1 mK in a pulsed He beam.' In: *Phys. Rev. Lett.* 60 (8), pp. 696–699. DOI: `10.1103/PhysRevLett.60.696`.

White, T. R. and B. E. Milton (2008). ‘Shock wave calibration of under-expanded natural gas fuel jets.’ In: *Shock Waves* 18 (5), pp. 353–364. DOI: `10.1007/S00193-008-0158-6/METRICS`.

Wolf, Andreas et al. (2004). ‘Storage Ring Experiments with Cold Molecular Ions: the H_3^+ *Puzzle*.’ In: *Physica Scripta* 2004.T110, p. 193.

Zhaunerchyk, V et al. (2007). ‘Rotational State Effects in the Dissociative Recombination of H_2^+.’ In: *Physical review letters* 99.1, p. 013201.

Acknowledgements

In the end I would like to mention and thank a few people without whom this thesis would have not been possible. I would like to thank **Prof. Dr. Klaus Blaum** who sparked my interest in electric storage devices and gave me the opportunity to do my master's thesis in his department. I want to thank **PD. Dr. Holger Kreckel** for the excellent supervision and for always taking time for me even when time was tight. My gratitude goes to **Prof. Dr. Xavier Urbain** who welcomed me in his lab and answered many of my questions and agreed to be the second referee for this thesis. My gratitude goes also to all the people I met during my time at the Université catholique de Louvain and helped to record the spectra that were used in this thesis, especially **Dr. Joffrey Fréreux** who not only recorded the data but also provided the simulated spectra for the resonant photodissociaton of N_2O^+. I want to thank **Felix Nuesslein**, who answered many questions about the simple supersonic expansion source and helped me numerous times. A big thank you goes to **Dr. Florian Grussie** who spend a lot of time with me in the lab, taught me even more about the CSR and supported me in more ways than I can name here. I want to thank **Viviane Schmidt**, who gave the right impulse at the right time. A big thank you goes to **Aigars Znotiņš**, with whom I shared an office and who was available for many discussions. I want to thank **Dr. Oldřich Novotný** for the helpful discussions. A big thank you to my colleagues **Ábel**, **Christopher**, **Damian**, **Daniel**, **Jonas**, **Lauren**, **Leonard**, **Lisa**, **Manfred** and **Selina** for the numerous conversations and activities we shared. I would like to thank all the technicians, without whom the CSR would not run, especially **Dirk Kaiser**, **Manfred König** and **Maximilian Trebis**. Thank you to everyone at the Max Planck Institute for Nuclear Physics, who made this thesis possible.

I would like to thank my colleagues at ImageContent, who made it possible for me to juggle work and university. A special thank you to **Xuan Xuyen Nguyen** who often stepped in for me. A big thank you to **Claudia Volk** for all the lectures we shared and all the waffles we ate. I want to thank **Peter Gutschank** for the long evenings working through my thesis. Even though the stress of finishing this thesis makes me question it, I'm sure I'll be grateful to him again in a few days for motivating me to study physics. A big thank you to all my friends who accompanied me during this time. I want to thank my parents **Ursula Berger** and **Willi Berger** as well as my sister **Rebekka Berger** for their unlimited support. I want to thank my girlfriend **Alissa Greshake** for her continuous support and her patience with me. Thank you to all the people who deserve to be on this list, but are not named here.

Erklärung:

Ich versichere, dass ich diese Arbeit selbstständig verfasst habe und keine anderen als die angegebenen Quellen und Hilfsmittel benutzt habe.

Heidelberg, 31.07.2023

Lukas Berger

Lukas Berger